

Understanding, detecting and conceptualising hydrogeologic barriers in groundwater modelling studies

By

Sarah K. Marshall

*Thesis
Submitted to Flinders University
for the degree of*

Doctor of Philosophy

College of Science and Engineering
August 2021

Declaration

I certify that this thesis:

- 1. does not incorporate without acknowledgment any material previously submitted for a degree or diploma in any university; and*
- 2. to the best of my knowledge and belief, does not contain any material previously published or written by another person except where due reference is made in the text.*

Sarah K. Marshall

July 1, 2021

Summary

Understanding and predicting groundwater flow can be challenging in regions with complex geology. Geological structures that inhibit flow, known as hydrogeologic barriers, can impact groundwater velocities, chemistry, and discharge dynamics, amongst other things. Examples of hydrogeologic barriers include some faults and dykes. Although not all faults and dykes are hydrogeologic barriers, this thesis is focused on the role of geological structures as hydrogeologic barriers, rather than as conduits. Barriers are difficult to detect and characterise. As such, they are often excluded from a conceptual model of a site. This could have implications for groundwater model predictions, and subsequent groundwater management, if the geological reality of a site is misrepresented. The thesis is part of a larger project investigating groundwater resources in the Pilbara region of Western Australia. The scope and research questions initially stemmed from this broader project. In the Pilbara region, hydrogeological barriers, including faults and dolerite dykes, are known to impact groundwater flow. However, the contents of the research is intrinsically universal and not based on one field area specifically.

This thesis addresses key issues on understanding, detecting and conceptualising groundwater barriers in groundwater modelling studies. On understanding barriers, by describing scenarios and quantifying conditions under which they can significantly impact groundwater level recovery associated with groundwater extraction. On detecting barriers, by showing how two commonly-collected hydrogeological datasets, hydraulic head and groundwater age, can assist in locating and characterising barriers depending on their configuration and the recharge setting. And on conceptualising barriers, by demonstrating a new method for inverse modelling that uses hydraulic head and groundwater age data to conceptualise models with no prior knowledge of barriers properties.

Specifically, the new contributions to research address:

1. During pumping, a hydrogeological barrier may be undetected if it is located beyond the maximum extent of the cone of depression; yet it may still control drawdown during the recovery phase. Non-dimensional solutions are devel-

oped to show the conditions under which a barrier may be undetected during pumping but still significantly impact groundwater level recovery. The magnitude of the impact from an undetected barrier will increase as the ratio of pumping rate to aquifer transmissivity increases.

2. The joint role of hydraulic head and groundwater age data in detecting and characterising hydrogeologic barriers, such as faults and dykes is studied. Numerical flow and transport models were developed with different hydrogeologic barrier configurations in a hypothetical aquifer. Computed hydraulic head and groundwater age distributions were compared to those without a barrier and two forms of recharge were compared.
3. Sharp barriers are included in groundwater model inversion, even where their presence is uncertain. A new method is introduced utilising ‘phantom structures’—randomly located, linear groups of model cells assigned a unique hydraulic conductivity value—to improve identifiability of barriers. Automated parameter estimation using PEST is implemented to determine model structures that best match the hydraulic head and groundwater age observation data from a hypothetical aquifer. The results are compared to model inversion using traditional pilot points.

As a whole, the thesis contributes to the study of structural geological heterogeneity and how it can be better represented in groundwater models that aid decision making. It aims to improve best practice for investigating and modelling aquifers with fault-like barriers. This has implications for projects where barriers play a significant role in the compartmentalisation of groundwater flow, spring dynamics, and drawdown and recovery associated with groundwater extraction.

Acknowledgments

This research was undertaken as a collaboration between the National Centre for Groundwater Research and Training (NCGRT) at Flinders University and Rio Tinto Iron Ore (RTIO). Funding sources included an Australian Government Research Training Program Scholarship, the Australian Research Council and RTIO. I would like to thank my primary supervisor, Peter Cook (NCGRT), for mentorship and technical expertise in all aspects of the project. I am also very grateful for the support of my co-supervisors, Craig Simmons (NCGRT) and Shawan Dogramaci (RTIO) for their invaluable guidance and suggestions. A large portion of my thesis was completed external to the Flinders University campus. For that reason, I owe much gratitude to the United States Geological Survey for hosting me as an exchange scholar in Reston, VA. In particular, I received endless logistical support and scientific mentoring from my adjunct supervisor, Leonard Konikow (USGS).

Many of the techniques implemented to complete this thesis were newly acquired during my candidature. I could not have come as far as I did without the guidance from both Jim McCallum (University of Western Australia) and Saskia Noorduijn (Geological Survey of Denmark and Greenland). I learnt a lot working with Tony Miller (Flinders University) and I appreciate advice from John Doherty (Watermark Numerical Computing). Valuable feedback was received from Jeffrey Starn (USGS), Paul Hsieh (USGS), and Matthew Currell (RMIT University), as well as from other anonymous reviewers. Undertaking a PhD candidature is not something I would have liked to do alone. My enjoyment and learning was greatly aided by my fellow PhD candidates, postdoctoral researchers, and colleagues at both Flinders University and the USGS. On a personal note, I know I could not have achieved what I did without the support of my loving family. In particular, thank you to my wonderful husband Tim, for always listening to and believing in me, and to our newborn daughter Maxine, for giving me lots of supportive kicks in the final few months.

Contents

Summary	iii
List of Figures	ix
List of Tables	xii
1 Introduction	1
1.1 Research problem	1
1.2 Project context	2
1.2.1 Detection of barriers using hydrogeologic data	5
1.2.2 Including barriers in groundwater models	5
1.3 Research aims	6
1.3.1 Publications arising from this thesis	8
1.4 Contributions of this thesis	8
2 The effect of undetected barriers on groundwater drawdown and recovery	11
2.1 Abstract	11
2.2 Introduction	12
2.3 Mathematical development	13
2.4 Groundwater drawdown and recovery with a single barrier	18
2.5 Timing of the maximum effect of a barrier	22
2.6 Groundwater drawdown and recovery with two orthogonal barriers	22
2.7 Maximum error in predictions of hydraulic head during recovery	23
2.8 Discussion and conclusions	25
3 Conjoint use of hydraulic head and groundwater age data to detect hydrogeologic barriers	27
3.1 Abstract	27
3.2 Introduction	28
3.3 Methods	30

3.3.1	Theory and numerical models	30
3.3.2	Conceptual models	30
3.3.3	Hydraulic head and groundwater age difference	33
3.3.4	Extent of spatial impact of a barrier	34
3.3.5	Change across the barrier	34
3.3.6	Baseline hydraulic head and groundwater age distributions	35
3.4	Results	36
3.4.1	Hydraulic head and groundwater age differences	36
3.4.2	Extent of spatial impact of a barrier	38
3.4.3	Change across the barrier	42
3.4.4	Impact of barrier orientation	44
3.4.5	Influence of aquifer properties	46
3.5	Discussion	49
3.5.1	Barrier detection	49
3.6	Assumptions and limitations	52
3.7	Conclusions	54
4	Hydrogeologic barriers in groundwater model inversions: the use of novel phantom structures	55
4.1	Abstract	55
4.2	Introduction	56
4.3	Materials and methods	58
4.3.1	Hypothetical model	58
4.3.2	Phantom structures	60
4.3.3	Hydraulic head and groundwater age data	62
4.3.4	Model inversions	64
4.3.5	Sensitivity analysis	66
4.3.6	Metrics for evaluating inversion results	66
4.4	Results	69
4.4.1	Single inversion	70
4.4.2	All simulations	74
4.4.3	Pilot points	77
4.5	Discussion	79
4.5.1	Limitations and future studies	81
4.6	Conclusions	83
5	Conclusions	84
5.1	Overview	84
5.2	Limitations and future work	86
5.3	Summary of findings	87

A Conceptual model of Baby Hope: a site in the Pilbara region of Western Australia	91
A.1 Introduction	91
A.2 Project background	92
A.2.1 Site description	92
A.2.2 Climate	93
A.2.3 Hydrogeology	94
A.2.4 Groundwater recharge	100
A.2.5 Groundwater chemistry	101
A.2.6 Hydrogeologic barriers	101
A.3 Groundwater data	102
A.4 Hydraulic head data	103
A.4.1 Steady state, pre-pumping data	103
A.4.2 Transient data	104
A.5 Groundwater chemistry	106
A.5.1 Radiocarbon data	106
A.5.2 CFCs	107
A.6 Stable isotopes	109
A.7 Summary	112
B Conference abstracts	122
B.1 Modelling the effect of undetected barriers on groundwater drawdown and recovery	122
B.2 Conjoint use of hydraulic head and groundwater age data to detect hydrogeologic barriers	123
Reference List	124

List of Figures

2.1	Schematic diagram of analytical method notation to calculate draw-down with one barrier.	15
2.2	Schematic diagram of analytical method notation to calculate draw-down with two barriers.	16
2.3	Plot of maximum difference in drawdown during pumping and recovery with one barrier.	19
2.4	Plot of the ratio of maximum difference in drawdown during pumping and recovery.	19
2.5	Plot of drawdown and recovery for simulation with hypothetical aquifer.	21
2.6	Plot of timing of maximum effect of barrier.	22
2.7	Plot of maximum difference in drawdown during pumping and recovery with two barriers.	24
2.8	Plot showing values of maximum difference in drawdown in recovery.	25
3.1	Schematic diagram of model set up showing boundary conditions and recharge.	32
3.2	Schematic, cross-section diagrams of model with various barrier configurations.	33
3.3	Hydraulic head and groundwater age results with no barrier.	36
3.4	Hydraulic head and groundwater age results with a fully-penetrating barrier.	37
3.5	Hydraulic head and groundwater age differences for the fully-penetrating barrier with uniform recharge.	39
3.6	Hydraulic head and groundwater age differences for the fully-penetrating barrier with upgradient recharge.	40
3.7	Hydraulic head and groundwater age results with a buried barrier.	41
3.8	Cumulative plots of hydraulic head and groundwater age difference depending on the distance from the barrier.	43
3.9	Plots of hydraulic head and groundwater age change across the barrier.	45

3.10	Cumulative plots of hydraulic head and groundwater age difference depending on orientation of barrier.	47
3.11	Plan-view maps of groundwater age difference for different barrier angles.	48
3.12	Plots showing the sensitivity of hydraulic head and groundwater age difference to different model metrics.	50
4.1	Schematic plot of model set up for forward model with a single barrier.	60
4.2	Locations of structures for each phantom structure configuration. . .	62
4.3	Hydraulic head and groundwater age calculated for forward model with single barrier.	63
4.4	Observation well locations for each scenario.	64
4.5	Workflow metric to describe the process for model inversion using phantom structures.	69
4.6	Hydraulic conductivity values for single example with phantom structures.	70
4.7	Hydraulic head and groundwater age difference between forward and inverse model single example.	72
4.8	Plot showing hydraulic head, groundwater age and combined <i>RMSE</i> values for single example.	73
4.9	Composite sensitivity of observation well data for single example. . .	74
4.10	Average values of hydraulic conductivity for each key phantom structure.	75
4.11	Combined <i>RMSE</i> values for all simulations.	76
4.12	Plot showing comparison between combined <i>RMSE</i> values for different phantom structure configurations and with pilot points.	77
4.13	Hydraulic conductivity distributions with pilot point approach.	79
A.1	Site description of Baby Hope region.	94
A.2	Mean monthly rainfalls for Baby Hope region.	95
A.3	Annual recorded rainfall for Baby Hope region.	95
A.4	Conceptual model of main aquifer types in the Pilbara.	96
A.5	Baby Hope geology cross sections.	98
A.6	Baby Hope interpreted cross section.	99
A.7	Three-dimensional geological model interpretation - west.	99
A.8	Three-dimensional geological model interpretation - east.	100
A.9	Groundwater wells across Baby Hope.	103
A.10	Steady state water levels across Baby Hope.	105
A.11	Cross section of radiocarbon data by total well depth.	107
A.12	Cross section of radiocarbon data by screen interval.	108

A.13 Cross section of CFC-12 data by total well depth.	109
A.14 Cross section of CFC-12 data by screen interval.	110
A.15 Stable isotopes plot for Baby Hope samples.	111
A.16 Transient water level data at western Baby Hope.	115
A.17 Transient water level data at western Baby Hope, between barriers.	116
A.18 Transient water level data at central Baby Hope.	117
A.19 Transient water level data at central Baby Hope.	118
A.20 Transient water level data from a single well at Baby Hope.	119
A.21 Transient water level data at eastern Baby Hope, between barriers.	119
A.22 Transient water level data at eastern Baby Hope.	120
A.23 Transient water level data at eastern Baby Hope.	121

List of Tables

2.1	Analytical approach description of symbols and dimensions.	14
3.1	Dimensions and universal parameters for modelling various barrier and recharge configurations.	31
3.2	Summary of results indicating likelihood of barrier detectability. . . .	51
4.1	Dimensions and universal parameters for inverse modelling with phantom structures.	59
4.2	Parameter values for key phantom structures in the single inversion. .	71
A.1	Radiocarbon data for Baby Hope samples.	106
A.2	CFC data for baby Hope samples.	108
A.3	Stable isotopes data for Baby Hope.	110
A.4	Well details for Baby Hope site, table 1 of 2.	113
A.5	Well details for Baby Hope site, table 2 of 2.	114

Chapter 1

Introduction

1.1 Research problem

Groundwater models are used to develop understanding about, and to forecast changes to, aquifer systems. However, they are built to emulate a three-dimensional subsurface that is hidden from view and accessed by a limited set of field data. Despite the best efforts of geoscientists, key elements of an aquifer system may be missed. We can think of these as “unknown unknowns” (Hunt and Welter 2010). This is especially likely for sites with an underlying geology that is complex and heterogeneous. At these sites, narrow, linear features such as faults and dykes can be overlooked if they are not discovered in regional geological or geophysical mapping or targeted by drilling. If they are overlooked in the conceptualisation of an aquifer, it follows that they will be missing from any site-specific groundwater models. This can result in what Bredehoeft (2005) describes as model “surprise”, where an inaccurate conceptualisation renders the original concepts of a model as invalid, leading to potentially significant errors in model predictions.

Faults, dykes and other geological structures occur in a diverse range of geological environments and manifest a variety of hydrogeological properties. This means that, even if they are known to be present, the implications of their presence for groundwater flow and transport can be difficult to discern. Studies that investigate the properties and long-term role of geological structures in an aquifer can be resource intensive; they may not be considered feasible where the cost of drilling and sampling is high. It is for this reason that this thesis helps improve the *understanding* of the role of these structures in groundwater systems; to discover efficient and effective means of *detecting* structures using common hydrogeological datasets; and to determine novel approaches for *conceptualising* geological structures in groundwater models that account for any uncertainty in knowledge of their properties.

The focus of this thesis is on one type of geological structure, that of hydrogeologic barriers. In this chapter, I will provide the context of the problems addressed in the thesis. The research undertaken is universal, in that it does not apply to one specific field region. However, the problem was defined by the overarching project, of which this thesis is a component, that is based in the Pilbara region of Western Australia. It is for this reason that I provide a brief description of this region, and some of its key hydrogeological and groundwater resource management issues. More site-specific information, including a summary of data collected, are provided in Appendix A. This appendix provides a framework for the research undertaken, which can be further extended to other field sites across Australia and the world. In this Introduction, I also set forth project context related to the study of hydrogeologic barriers and conceptual model uncertainty. The key knowledge gaps and scientific hypotheses that this thesis addresses are presented. Detailed literature summaries specific to each body of research are also included at the beginning of Chapters 2, 3 and 4. The final part of this Introduction clearly outlines the aims of the thesis and the new contributions of knowledge that it provides.

1.2 Project context

This thesis forms a component of a broader project investigating groundwater resources in the semi-arid Pilbara region of Western Australia (Cook et al. 2016; Dogramaci and Skrzypek 2015; McCallum et al. 2017; Poulsen et al. 2019; Underwood et al. 2018). Australia has the world's largest economic demonstrated resources of iron ore, and 92 % of it comes from the Pilbara region (Senior et al. 2020). The principal field site of the overarching project is in the Hamersley Basin, which unconformably overlies the Archean Pilbara Craton and contains most of the iron ore deposits in Western Australia (McFarlane 2015). An understanding of the groundwater resources in the region is required so that mining in the area can proceed while also satisfying regulatory conditions and stakeholder agreements with respect to environmental and societal impacts to water resources. However, the Hamersley Basin is vast and its geology is complex. Novel approaches are required to model the impacts of mining on the environment, including the role of the complex geology on controlling groundwater flow.

The Archean to Palaeoproterozoic Hamersley Basin is geographically and geologically diverse, which is reflected in its complex hydrological setting. Alluvial sediments are underlain by hard rocks, in which groundwater flow dominantly occurs through fracture networks (Dogramaci and Skrzypek 2015). The main aquifer types include: (1) alluvial aquifers; (2) calcrete and pisolithic limonite aquifers; (3) inter-

granular sedimentary rock aquifers; and (4) fractured rock aquifers (Johnson 2004). The most significant is considered to be a karst dolomite aquifer, yet fractured rock aquifers are locally significant for supporting springs and other groundwater-dependent ecosystems (Rojas et al. 2018). Palaeovalleys and alluvial sediments associated with modern drainage systems can also be important aquifers (Commander et al. 2015).

Due to its long deformation history and intrusive events, the Hamersley Basin is structurally complex (Rojas et al. 2018). Importantly, hydrogeologic barriers are common throughout the region and are known to exert control on groundwater flow (Latscha 2010; Pham 2016; RPS Group 2015). In the Pilbara, hydrogeologic barriers are primarily faults and dykes, but they also include chert bands, inclined shale beds and unkarstified dolomite units (Latscha 2010). In many cases, however, the location or properties of hydrogeologic barriers are not completely understood, with little data available to constrain them (Pham 2016). At the Baby Hope site within the Pilbara, we see that four hydrogeologic barriers have been inferred due to the distribution of hydraulic head data (Appendix A). However, the location and geological properties of only two of the four barriers have been confirmed with exploratory drilling. For the other two barriers, the geological explanation of a hydrogeological phenomenon—that of a sharp change in groundwater levels, has not been explained. Furthermore, for the two barriers confirmed by drilling, there is no clear understanding of how their geological properties translate in terms of hydrogeological parameters. In addition, a limited understanding of recharge processes at the site means that there is little knowledge of how the inferred barriers will affect groundwater processes such as residence times and flow paths. This poses challenges for the interpretation of groundwater age data without an understanding of how different styles of barriers influence both hydraulic head and groundwater age.

Hydrogeologic barriers are structures that cut off or restrict groundwater flow (Ferris et al. 1962). Due to this compartmentalisation effect on groundwater systems, they are often important to consider in groundwater studies (Bense et al. 2003; Ciloni et al. 2015; Ferrill et al. 2004). In particular, they exert influence on spring and wetland formation (Babiker and Gudmundsson 2004; Gleeson and Novakowski 2009), groundwater drawdown (Bense and Van Balen 2004; Gumm et al. 2016; Hadley et al. 2020), and the spatial distribution of groundwater chemistry (Gumm et al. 2016; Mayer et al. 2007; Sebben and Werner 2016). Faults, dykes and other geological structures do not always form hydrogeologic barriers. Some faults and dykes are permeable and others are complex barrier-conduits. In fault zones, the permeability structure will vary depend on the proportion of the core of the fault, which is

generally lower permeability, to the outer, more permeable, damage zone (Caine et al. 1996). Other factors also play a role, such as the host rock type, the regional stress regime, and mineral precipitation (Bense et al. 2013). The focus of this thesis is specifically on hydrogeologic barriers because they are known to compartmentalise groundwater systems, play a dominant role in controlling groundwater flow in the Pilbara region, and yet have not been the specific focus of many previous groundwater studies.

The variability of geological structures, and the settings in which they can form, mean that there is no single conceptualisation to define a hydrogeologic barrier. Therefore, understanding the impact that a barrier has on a flow system will usually be specific to a particular region. This is limited, however, by the fact that it can be resource-intensive to detect and characterise geological structures. A barrier's properties, such as its precise location, length, width, orientation, and permeability structure are often not fully known. This then translates into uncertainty in the representation of that barrier in a groundwater model. As a result, structures such as faults and dykes are often excluded from, or misrepresented in, groundwater models. Understanding the influence of hydrogeologic barriers on groundwater model predictions can be essential in certain groundwater flow regimes. In this thesis, I will demonstrate how simple analytical models can be used to build understanding of where barriers affect groundwater levels in response to large-scale groundwater pumping, such as occurs in mining regions such as the Pilbara.

Studies of large-scale groundwater pumping are relevant in mining regions and may be compromised by undetected or mis-conceptualised hydrogeologic barriers. The mining industry extracts, and disposes of, large volumes of groundwater for both consumptive (e.g. ore processing) and non-consumptive (e.g. dewatering) purposes. In Australia, reported water use by the mining industry was 1108 GL in 2017–18 (Australian Bureau of Statistics 2020). Dewatering is a form of groundwater extraction required for almost all open cut or underground mines that work below the water table (Younger et al. 2002). This allows mining to proceed in dry conditions but may cause a lowering of the potentiometric surface over a broader region than the mine itself. The duration of reduced groundwater pressure resulting from the dewatering may also extend longer than the life of the mine. Numerical and analytical models can be used to predict groundwater drawdown and recovery as a result of mine dewatering. Their use, however, requires a thorough understanding of the mining environment, including regional hydrogeological parameters (Rapantova et al. 2007). This understanding may not be evident if geological structures have not been adequately detected and characterised.

1.2.1 Detection of barriers using hydrogeologic data

This thesis specifically focuses on the use of hydraulic head and groundwater age data for barrier detection and characterisation, because these datasets provide direct information on groundwater flow. Stationary and transient hydraulic head data have both proven useful in the detection of barriers (Allen and Michel 1999; Bense et al. 2003; Cilona et al. 2015; Hadley et al. 2020; Mayer et al. 2007; Seaton and Burbey 2005). The use of groundwater age, although less frequent, is also a powerful indicator of groundwater flow conditions (Cook and Böhlke 2000) that has been applied to regions with flow barriers (Castro and Goblet 2005; Janos et al. 2018; Raiber et al. 2015). Although demonstrated examples exist using both hydraulic head and groundwater age for a barrier’s detection, the methods have limited resolution where well density is sparse. Wells intersecting or surrounding geologic structures such as faults are uncommon (Bense et al. 2013). There is a paucity in research into the scenarios where these datasets are most beneficial, and how different barrier configurations and recharge conditions affect their ability to detect and characterise a hydrogeologic barrier.

Other methods also exist for detecting barriers. These include surface or aerial geophysics (Ball et al. 2010; Vittecoq et al. 2015); groundwater temperature (Bense and Kooi 2004; Fairley 2009); and lineament analysis (Per et al. 1997; Tam et al. 2004). Yet these datasets are often not available in a region. They may be expensive to collect, particularly over a large regional area. In addition, geophysics and lineament analysis, while useful in detecting the presence of a structure, do not provide information on its hydrological properties (e.g. Viezzoli et al. 2013). By focusing this thesis on hydraulic head and groundwater age data, I aim to demonstrate how two commonly-collected hydrogeological datasets can be used in the detection and characterisation of hydrogeologic barriers.

1.2.2 Including barriers in groundwater models

Even where barrier properties are not thoroughly characterised, they may still be included in groundwater models. Determining the most likely aquifer and barrier properties in light of uncertainty is often achieved using model inversion techniques. Model inversion (or model calibration) is a procedure whereby expert knowledge and direct measurements can be combined to help estimate a groundwater system’s parameters. It has been applied in previous studies to estimate the properties of hydrogeologic barriers (Comte et al. 2017; Hadley et al. 2020; Mayer et al. 2007; Ochoa-González et al. 2015). Traditionally, however, the locations and geometric properties of structures (such as width, strike and dip) are fixed, regardless of whether knowledge of these properties is uncertain.

There is little precedent for including hydrogeologic barriers with uncertain geometric properties in a groundwater model. Although the use of training images and other geostatistical approaches have been shown to be helpful in uncovering uncertain aquifer structures (Chen and Rubin 2003; Harp et al. 2008; Koohbor et al. 2019; McCallum et al. 2014b), they often require considerable knowledge of existing aquifer properties at the outset to interpolate new aquifer structures. In this thesis, a new method for including hydrogeologic barriers with uncertain properties in groundwater models is introduced. This is a step towards reducing conceptual model uncertainty (i.e. structural noise) in regions of complex geology.

Uncertainty in model conceptualisation encompasses many forms of model error arising from an inadequate representation of a system's geometry, physics and processes (e.g. Enemark et al. 2019). The consideration of conceptual uncertainty is important because it often forms the largest component of uncertainty in the modelling process (Carrera and Neuman 1986; Doherty and Welter 2010; Gupta et al. 2012; Ye et al. 2004). This thesis addresses uncertainty that lies in the unknown location, geometric properties and hydraulic conductivity of hydrogeologic barriers. At sites such as the Pilbara region, conceptual uncertainty can hinder assessments of how mines will affect regional water systems both during and after mining. It may also lead to loss of confidence by stakeholders in the decisions related to environmental management. Understanding the best way to represent conceptual model uncertainty in groundwater predictions, such as in mining regions, will allow better decision making and more public confidence in the environmental and economic stability of a region's water resources.

1.3 Research aims

The purpose of this research is to build understanding about the impact of hydrogeologic barriers on groundwater flow and to develop strategies for improving their conceptualisation in groundwater models. To do this, several modelling techniques are incorporated, including analytical modelling, numerical modelling of groundwater flow and transport, and inverse modelling. Although all of the research is hypothetical, in that it is not specific to one particular field site, the problems addressed stem from issues pertaining to the overarching project based in the Pilbara region of Western Australia. In particular, the work was informed to develop insight into a new mining site known as 'Baby Hope'. At this site, clear hydraulic head drops across inferred hydrogeologic barriers have been observed and reported. Groundwater samples from the site were used to provide estimates of groundwater age, based on the analysis of radiocarbon and CFCs. These data, and a conceptualisation of

the site, are included in Appendix A. The mining company, along with researchers from the National Centre of Groundwater Research and Training, recognised that these barriers may impact dewatering estimates for, and drawdown impacts from, mining at the Baby Hope site. Discussions about how best to investigate the role of the inferred barriers on groundwater levels were original seeds from which the project's broader research aims evolved.

The thesis aims relate to understanding the effect that lack of knowledge about hydrogeologic barriers could have on models of groundwater flow. They revolve around developing strategies to better detect and model barriers where their properties are uncertain.

The knowledge gaps addressed in this thesis relate to limited understanding in the following areas:

1. The quantification of how the exclusion of barriers from groundwater models could impact estimates of groundwater drawdown and recovery.
2. The ways that hydrogeologic barriers impact hydraulic head and groundwater age distributions in aquifers, under different recharge conditions.
3. Understanding of how the geometry of a barrier affects a hydraulic head or groundwater age distribution in an aquifer.
4. Studying methods to detect and characterise hydrogeologic barriers, whose presence was not previously known, using hydraulic head and groundwater age data.
5. The use of hydrogeologic datasets for identifying and characterising new hydrogeologic barriers using inverse methods.

Based on these identified knowledge gaps, associated research aims are summarised as follows:

- **Objective 1.** If a barrier that is undetected, and therefore not included in a conceptual model of a site, it can introduce structural uncertainty in model predictions. The *aim* of the first study (Chapter 2) was therefore to determine both spatially and temporally when impermeable barriers should be considered in predictive groundwater models, and what their impact on groundwater level predictions could be.
- **Objective 2.** Hydraulic head distributions may not definitively indicate the presence of barriers, particularly if the sampling density is low. The *aim* of the second study (Chapter 3) is to determine the detectability of barriers under contrasting recharge settings and barrier configurations. The detection, and

any further characterisation, of barriers relies inherently on the availability of data. The objective is not to quantitatively address the impact of data density on barrier detection. Instead, the focus is on when, and to what degree, hydraulic head and groundwater age data may be useful in detecting barriers in simple aquifer systems.

- **Objective 3.** Hydrogeologic barriers can significantly impact groundwater model predictions. The *aim* of the third study (Chapter 4) is to include hydrogeologic barriers in a model where their presence is suspected but unverified. A new method is proposed that allows for the inclusion of thin impermeable structures, which may include faults and dykes, in a model inversion, without knowing their location or properties in advance.

1.3.1 Publications arising from this thesis

This thesis is structured as a body of papers. The aims from each paper are addressed in Chapters 2, 3 and 4 of the thesis, and each is also a manuscript submitted for publication in respected international journals. At the time of writing, the first two papers are published. These are listed below.

- Marshall, S. K., P. G. Cook, A. D. Miller, C. T. Simmons, S. Dogramaci, 2019. The Effect of Undetected Barriers on Groundwater Drawdown and Recovery. *Groundwater*, 57(5): 718–726.
- Marshall, S. K., P. G. Cook, L. F. Konikow, C. T. Simmons, S. Dogramaci, 2020. Conjoint use of hydraulic head and groundwater age data to detect hydrogeologic barriers. *Hydrogeology Journal* 28: 1003–1019.

The third manuscript has been submitted to an international journal and is in the peer review process. Aspects of this work were presented twice at scientific conferences, abstracts for these presentations are provided in Appendix B.

1.4 Contributions of this thesis

This thesis contributes original research to the issue of how the groundwater research community can address conceptual model uncertainty arising from geological complexity. New contributions to knowledge are presented in Chapters 2, 3 and 4, and these are summarised as follows.

Firstly, in Chapter 2, simple analytical expressions for radial flow to a well based on Theis (1935) are adapted to show the effect that barriers can have on groundwater recovery when they are not detected during the pumping phase of a project. Non-

dimensionalised solutions are developed to show the aquifer and barrier properties that result in the largest impact on groundwater level recoveries. These properties include the aquifer thickness, hydraulic conductivity, storativity, the duration of aquifer pumping and the distance of a pumping well to a barrier. A comparison is made between the impact of a single barrier and two orthogonal barriers on groundwater drawdown and recovery. This research presents simple and adaptable solutions that are not only relevant in mining regions, such as the Pilbara, where large-scale groundwater extraction occurs for the purpose of dewatering mines. Indeed the research is relevant to any groundwater extraction project in regions with complex geology.

Secondly, in Chapter 3, groundwater flow and transport models are developed to represent two barrier configurations: where the barrier penetrates the full thickness of the aquifer; and where the barrier is overlain by permeable aquifer material. The study considers the likelihood of two datasets, hydraulic head and groundwater age, in detecting these barriers under two recharge conditions. Recharge is either applied uniformly across the aquifer, or only in the upper part of the catchment (representing ‘mountain-front’ recharge). The impact of the barrier’s orientation, thickness and other properties on hydraulic head and groundwater age gradients across the barriers are investigated. This study contributes to the better employment of these two hydrogeologic datasets in detecting hydraulic barriers and helps to show the geological settings where they are most helpful in this pursuit.

Thirdly, in Chapter 4, a new method for groundwater inverse modelling is developed that utilises novel ‘phantom structures’—randomly located, linear groups of model cells assigned a unique hydraulic conductivity value—to improve identifiability of barriers. A forward model with a hydraulic barrier is based on what is known of aquifer and barrier properties in the Pilbara region. This is then sampled at various observation well densities and the properties of phantom structures are estimated using regularised inversion utilising the PEST software suite (Doherty 2018b). This new approach tests whether the geometric and physical properties of barriers can be successfully estimated, even where no prior knowledge of them exists. The technique is compared to the previously-demonstrated approach of using pilot points to reproduce hydraulic conductivity distribution across an aquifer. The study builds on a key limitation of the pilot point approach, which is that sharp changes in aquifer properties are difficult to estimate in model inversion studies due to issues of solution uniqueness. The study can be adapted to any region with narrow, linear, low-permeability structures such as faults and dykes. It is a step towards improving aquifer conceptualisation where these structures occur, but are not well defined.

Finally, in Chapter 5, the conclusions from the body of research as a whole are summarised. This chapter also presents limitations of the studies and some recommendation for new research questions rooted in the outcomes of this thesis. Appendix A provides a conceptual model of one of the sites at the Pilbara, known as Baby Hope. Previously existing and new data are collated to discuss the role of inferred hydrogeologic barriers on groundwater flow. This appendix do not provide a full analysis of the role of hydrogeologic barriers on groundwater flow at Baby Hope. Instead, the intent is to provide context about a site for which the new findings presented in this thesis are relevant. This lays out a bridge to link the theoretical contributions of the thesis to field sites, such as Baby Hope, with complex geology.

Chapter 2

The effect of undetected barriers on groundwater drawdown and recovery

Citation for published article: Marshall, S. K., P. G. Cook, A. D. Miller, C. T. Simmons, S. Dogramaci, 2019. The Effect of Undetected Barriers on Groundwater Drawdown and Recovery. *Groundwater*, 57(5): 718–726.

2.1 Abstract

In large-scale pumping projects, such as mine dewatering, predictions are often made about the rate of groundwater level recovery after pumping has ceased. However, these predictions may be impacted by geological uncertainty—including the presence of undetected impermeable barriers. During pumping, an impermeable barrier may be undetected if it is located beyond the maximum extent of the cone of depression; yet it may still control drawdown during the recovery phase. This has implications for regional-scale modelling and monitoring of groundwater level recovery. In this paper, non-dimensional solutions are developed to show the conditions under which a barrier may be undetected during pumping but still significantly impact groundwater level recovery. The magnitude of the impact from an undetected barrier will increase as the ratio of pumping rate to aquifer transmissivity increases. The results are exemplified for a hypothetical aquifer with an unknown barrier 3 km from a pumping well. The difference in drawdown between a model with and without a barrier may be < 1 m in the ten years while pumping is occurring, but up to 50 m after pumping has ceased.

2.2 Introduction

Using numerical or analytical models to predict future groundwater levels, the core objective of many hydrogeological studies, is contingent upon geological understanding of a site. This paper discusses one aspect of geological complexity, that of impermeable barriers, due to their significance for studies of hydraulic head in regions with groundwater extraction. In this context, ‘impermeable barriers’ are linear features that cut off or prevent groundwater flow (Ferris et al. 1962). Geological structures—such as faults and dykes—can be conduits, barriers, or complex conduit-barrier combinations to groundwater flow (Allen and Michel 1999; Babiker and Gudmundsson 2004; Bense and Person 2006; Caine et al. 1996). In fault zones the permeability structure depends on the proportion of the core of the fault, which is generally of lower permeability, to the more permeable, outer damage zone (Caine et al. 1996). Other factors such as the host rock type, the regional stress regime, and mineral precipitation also play a role (Bense et al. 2013).

Under steady state flow conditions, impermeable barriers can influence the distribution of hydraulic heads (Bense et al. 2013; Bense and Van Balen 2004; Gumm et al. 2016; Mayer et al. 2007; Rawling et al. 2001; Seaton and Burbey 2005). Yet during groundwater extraction, if an impermeable barrier exists beyond the extent of the cone of depression, it will not have any effect on drawdown. At some distance away from pumping, the maximum decline in groundwater level may not occur until after pumping has ceased (Bredehoeft 2011). Then, if the cone of depression intersects an impermeable barrier, drawdown on the pumping side of the barrier will be greater than it otherwise would be if that barrier were not present. In this case, hydraulic head measurements taken during pumping would not detect the presence of the barrier. Other methods available for locating impermeable barriers rely on datasets that can be clustered around the site of extraction rather than in the broader region (Cook et al. 2016), and so a barrier may remain undetected.

The role that groundwater barriers play in pumping test analysis has been thoroughly characterised (Ferris et al. 1962; Kruseman and Ridder 2000; Pujades et al. 2012; Wu et al. 2017). In addition, methods have been developed for groundwater modelling in regions with hydraulic barriers, including: using analytical models (Fitts 1997); understanding horizontal (Anderson 2006) and vertical (Anderson and Bakker 2008) anisotropy across impermeable barriers, including in multi-aquifer settings; incorporating impermeable barriers into numerical modelling codes (Hsieh and Freckleton 1993); and using numerical models to test different permeabilities of fault zones (Bense and Person 2006). However, many of the studies have been limited to steady-state flow and few discussed the recovery period following pumping. Yet

predictions of groundwater levels in transient systems, including during groundwater recovery, are often required for the purpose of watershed and ecosystem management (Currell et al. 2017; Toran and Bradbury 1988). If a barrier is undetected, and therefore not included in a conceptual model of a site, it can introduce structural uncertainty in model predictions. In general, the implications of structural model uncertainty have been well documented (Beven 2005; Bredehoeft 2005; Gupta et al. 2012; Refsgaard et al. 2012). However, to date no research has quantified the degree to which model predictions could be inaccurate if impermeable barriers are not included in models of groundwater drawdown. The aim of this study was therefore to determine both spatially and temporally when impermeable barriers should be considered in predictive groundwater models, and what their impact on groundwater level predictions could be.

2.3 Mathematical development

Analytical models (Ferris et al. 1962; Theis 1935) were used to compare groundwater drawdown with and without an impermeable barrier. The difference in drawdown between these two end members will be referred to as ‘the effect of the barrier(s)’. The effect of a barrier, or multiple barriers, was evaluated during extraction (pumping phase) and also once pumping had ceased (recovery phase) at various distances from pumping and in aquifers with different geological properties. Drawdown from a pumping well was represented by the Theis equation (Theis 1935). For an aquifer of infinite extent and with a constant transmissivity, drawdown during pumping in a homogeneous aquifer (s_1^p) is represented as:

$$s_1^p = -\frac{Q}{4\pi T} \left(\text{Ei} \left(\frac{-r^2}{4\kappa t} \right) \right). \quad (2.1)$$

Symbols are defined in Table 2.1, and $\text{Ei}()$ represents the exponential integral function:

$$\text{Ei}(x) = -\int_{-x}^{\infty} \frac{e^{-u}}{u} du. \quad (2.2)$$

Drawdown with an impermeable barrier, which is a no-flow boundary, for an observation well some distance, r , from the pumping well, can be derived by applying the superposition principle using the image well technique (Ferris et al. 1962), which assumes that the barrier has no permeability, spans the whole thickness of the aquifer and is of infinite length. A plan view schematic diagram of the problem is presented in Figure 2.1. Drawdown at the observation well, in the presence of the impermeable

Symbol	Description
s_1^p	Drawdown [L] without a hydraulic barrier during pumping, where $s > 0$ indicates a lower hydraulic head.
s_2^p	Drawdown [L] with a hydraulic barrier during pumping.
s_1^r	Drawdown [L] without a hydraulic barrier during recovery.
s_2^r	Drawdown [L] with a hydraulic barrier during recovery.
Q	Extraction/pumping rate, where $Q > 0$ indicates extraction [$\frac{L^3}{T}$].
K	Hydraulic conductivity of aquifer [$\frac{L}{T}$].
b	Thickness of aquifer [L].
T	Transmissivity of aquifer [$\frac{L^2}{T}$].
S	Specific storage [dimensionless].
κ	Aquifer diffusivity = $\frac{T}{S}$ [$\frac{L^2}{T}$].
r	Radial distance of the pumping well to the observation well/point [L].
R	Radial distance of the image well to the observation well/point [L].
L	Radial distance of the pumping well to the barrier.
t	Time at which drawdown is evaluated [T].
τ_{off}	Time at which pumping ceases, i.e. $Q = 0$ [T].
Δs^p	Difference in drawdown with and without the barrier: i.e. the effect of the barrier, during pumping [L].
Δs^r	Difference in drawdown with and without the barrier: i.e. the effect of the barrier, during recovery [L].
ϵ	The ratio of the maximum effect of the barrier during recovery compared to pumping.
t_{max}^r	Time of the maximum effect of the barrier during recovery [T].
Δs^{p*}	Non-dimensional difference in drawdown during pumping, where Δs^p [L] is scaled by $\frac{Q}{4\pi T}$ [L].
Δs^{r*}	Non-dimensional difference in drawdown during recovery, where Δs^r [L] is scaled by $\frac{Q}{4\pi T}$ [L].
r^{2*}	Non-dimensional distance from a pumping well to an observation well/point, where r^2 [L ²] is scaled by $4\kappa\tau_{off}$ [L ²].

Table 2.1: Description of symbols and dimensions.

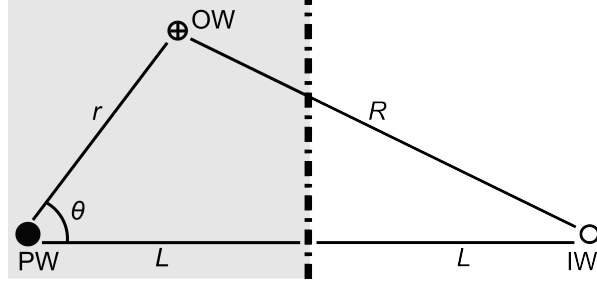


Figure 2.1: Schematic, plan-view diagram of notation used in the analytical method to calculate drawdown in the presence of an impermeable barrier (*dot-dash line*). The *shaded region* represents the physical region, the *white region* represents the imaginary region. The solution from an image well, depicted by the *open black circle*, was used along with real discharge at the pumping well, depicted by the *filled black circle*, to derive the solution for drawdown at the observation well shown as *black circle filled with a cross*. *PW* = Pumping well; *OW* = Observation well; *IW* = Image well.

barrier, can therefore be represented by:

$$s_2^p = -\frac{Q}{4\pi T} \left(\text{Ei} \left(\frac{-r^2}{4\kappa t} \right) + \text{Ei} \left(\frac{-R^2}{4\kappa t} \right) \right). \quad (2.3)$$

In this approach, R can be calculated if the angle, θ , between the line perpendicular to the barrier that passes through the pumping well and the line from the pumping well to the observation well is known, where $R = r \sin \theta \sqrt{1 + \left(\frac{2L - r \cos \theta}{r \sin \theta} \right)^2}$. Suppose that pumping ceases at a time $t = \tau_{off}$. Drawdown at the observation well for $t > \tau_{off}$ with no impermeable barrier present (s_1^r) is shown in Equation 2.4, and with a barrier present (s_2^r) is shown by Equation 2.5. These equations are obtained from Equations 2.1 and 2.3 by adding an additional expression for drawdown which uses an inflow term with the same, yet negative, rate of extraction Q where inflow begins at the cessation of pumping (where $t = \tau_{off}$). By the principle of superposition, this is then added to the original drawdown for each time step, which results in water level simulations for the recovery period $t > \tau_{off}$:

$$s_1^r = -\frac{Q}{4\pi T} \left(\text{Ei} \left(\frac{-r^2}{4\kappa t} \right) \right) + \frac{Q}{4\pi T} \left(\text{Ei} \left(\frac{-r^2}{4\kappa(t - \tau_{off})} \right) \right), \quad (2.4)$$

$$s_2^r = -\frac{Q}{4\pi T} \left(\text{Ei} \left(\frac{-r^2}{4\kappa t} \right) + \text{Ei} \left(\frac{-R^2}{4\kappa t} \right) \right) + \frac{Q}{4\pi T} \left(\text{Ei} \left(\frac{-r^2}{4\kappa(t - \tau_{off})} \right) + \text{Ei} \left(\frac{-R^2}{4\kappa(t - \tau_{off})} \right) \right). \quad (2.5)$$

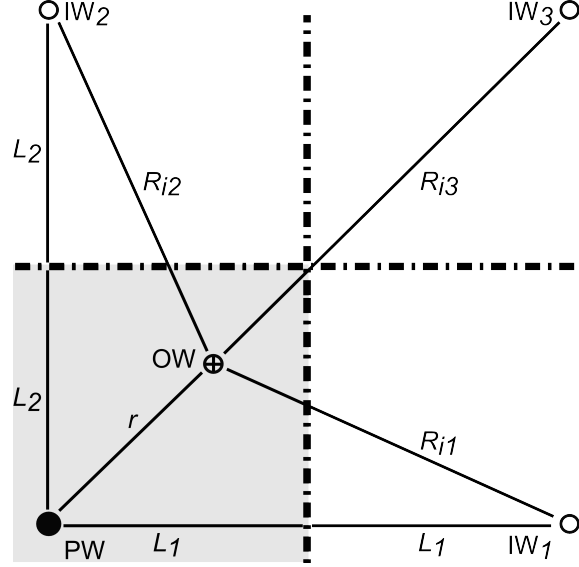


Figure 2.2: Schematic, plan-view diagram of notation used in the analytical method to calculate drawdown in the presence of a two hydraulic barriers (*dot-dash lines*). The *shaded region* represents the physical region, the *white region* represents the imaginary region. The solution from three image wells, IW_1 , IW_2 and IW_3 , depicted by *black open circles* were used along with real discharge at the pumping well, depicted by the *black filled circle*, to derive the solution for drawdown at the observation well shown as the *black circle filled with a cross*. PW = Pumping well; OW = Observation well; IW = Image well.

To observe the effect of two barriers on groundwater drawdown, where the two barriers are orthogonal, drawdown at an observation point can be calculated by including more image wells. With two orthogonal barriers, the imaginary system includes three image wells and thus Equation 2.3 expands to become Equation 2.6. R_{i1} , R_{i2} and R_{i3} represent the radial distances from the observation well to each of the image wells, $i1$, $i2$ and $i3$, respectively (Figure 2.2). The drawdown in the observation well during pumping with two barriers is:

$$s_2^p = -\frac{Q}{4\pi T} \left(\text{Ei} \left(\frac{-r^2}{4\kappa t} \right) + \text{Ei} \left(\frac{-R_{i1}^2}{4\kappa t} \right) + \text{Ei} \left(\frac{-R_{i2}^2}{4\kappa t} \right) + \text{Ei} \left(\frac{-R_{i3}^2}{4\kappa t} \right) \right). \quad (2.6)$$

And drawdown in the observation well during recovery ($t > \tau_{off}$) with two barriers is:

$$s_2^r = -\frac{Q}{4\pi T} \left(\text{Ei} \left(\frac{-r^2}{4\kappa t} \right) + \text{Ei} \left(\frac{-R_{i1}^2}{4\kappa t} \right) + \text{Ei} \left(\frac{-R_{i2}^2}{4\kappa t} \right) + \text{Ei} \left(\frac{-R_{i3}^2}{4\kappa t} \right) \right) + \frac{Q}{4\pi T} \left(\text{Ei} \left(\frac{-r^2}{4\kappa(t - \tau_{off})} \right) + \text{Ei} \left(\frac{-R_{i1}^2}{4\kappa(t - \tau_{off})} \right) + \text{Ei} \left(\frac{-R_{i4}^2}{4\kappa(t - \tau_{off})} \right) + \text{Ei} \left(\frac{-R_{i3}^2}{4\kappa(t - \tau_{off})} \right) \right). \quad (2.7)$$

The difference in drawdown between the barrier and non-barrier scenarios (δs) during pumping and recovery are:

$$\Delta s^p = s_2^p - s_1^p, \quad (2.8)$$

$$\Delta s^r = s_2^r - s_1^r. \quad (2.9)$$

Δs represents the effect of the barrier, and the error in a prediction of drawdown, where it may be uncertain whether or not a barrier is present. The time of the maximum effect of the barrier during pumping is the time at which pumping ceases because the effect of the barrier increases as drawdown increases. On the other hand, the time of the maximum effect of the barrier during recovery, t_{max}^r , will vary depending on pumping duration, τ_{off} , and aquifer diffusivity, κ . The value of t_{max}^r , for any value of τ_{off} where $t > \tau_{off}$, can be found by setting $\frac{d\Delta s^r}{dt} = 0$, and solving for t . For the one barrier case, this produces:

$$-\frac{\exp(-R^2/4\kappa t_{max}^r)}{t_{max}^r/\tau_{off}} + \frac{\exp(-R^2/4\kappa(t_{max}^r - \tau_{off}))}{(t_{max}^r/\tau_{off}) - 1} = 0, \quad (2.10)$$

or for the two orthogonal barrier case:

$$-\frac{\exp(-R_{i1}^2/4\kappa t_{max}^r)}{t_{max}^r/\tau_{off}} - \frac{\exp(-R_{i2}^2/4\kappa t_{max}^r)}{t_{max}^r/\tau_{off}} - \frac{\exp(-R_{i3}^2/4\kappa t_{max}^r)}{t_{max}^r/\tau_{off}} + \frac{\exp(-R_{i1}^2/4\kappa(t_{max}^r - \tau_{off}))}{(t_{max}^r/\tau_{off}) - 1} + \frac{\exp(-R_{i2}^2/4\kappa(t_{max}^r - \tau_{off}))}{(t_{max}^r/\tau_{off}) - 1} + \frac{\exp(-R_{i3}^2/4\kappa(t_{max}^r - \tau_{off}))}{(t_{max}^r/\tau_{off}) - 1} = 0. \quad (2.11)$$

These can easily be solved numerically for t_{max}^r . It is also convenient to define the ratio of the maximum Δs^r to the maximum Δs^p :

$$\epsilon = \frac{\max \Delta s^r}{\max \Delta s^p}, \quad (2.12)$$

to understand the relative effect of the barrier during recovery compared to pumping. The $\max \Delta s^p$ and $\max \Delta s^r$ occur where $t = \tau_{off}$ and $t = t_{max}^r$, respectively. Where the effect of the barrier is high during recovery and low during pumping, the value ϵ will be high. As the effect of the barrier during pumping approaches 0, the ratio approaches infinity.

2.4 Groundwater drawdown and recovery with a single barrier

Drawdown with and without an impermeable barrier during pumping and recovery was analysed over a wide parameter space initially for systems with one barrier (Equations 2.8 and 2.9). To study the circumstances where the effect of the barrier is not observed during pumping, yet is significant during recovery, $\max \Delta s^p$ was compared to $\max \Delta s^r$ for various values of r , κ and τ_{off} (Figure 2.3). To simplify, situations where $r = R = L$ were explored as this represents a worst-case scenario. This means that the observation well is at the point immediately adjacent to the barrier nearest the pumping well on the straight line between the pumping well and image well. Differences in drawdown Δs [L] are scaled by $\frac{Q}{4\pi T}$ [L] to give non-dimensional quantities Δs^* . The squared radial distance, r^2 [L²], is scaled by $4\kappa\tau_{off}$ [L²] to give the non-dimensional quantity r^{2*} . As the value of r^{2*} increases, the values of both $\max \Delta s^{p*}$ and $\max \Delta s^{r*}$ decrease, with $\max \Delta s^{p*}$ always lower than $\max \Delta s^{r*}$.

To understand the results, we can study the distance, r^{2*} , at which the effect of the barrier becomes insignificant (and therefore unobservable) in the pumping phase. Suppose that we define a significant amount of additional drawdown due to the presence of a barrier as $\Delta s > 1$ m. We consider three scenarios: $Q/T = 10^2$, 10^3 and 10^4 m, which respectively give $\max \Delta s^{p*} = 0.13$, 0.013 and 0.0013. For each of these values, the largest value of $\max \Delta s^{r*}$ (and hence also $\max \Delta s^r$) can be determined for each corresponding value of r^{2*} . From Figure 2.3, we therefore get r^{2*} values of 1.4, 3.0, and 4.9 for $Q/T = 10^2$ m, 10^3 m and 10^4 m, respectively. For each distance, r^{2*} , the value of $\max \Delta s^{r*}$ can therefore also be read from the graph. These non-dimensional values are, respectively, 0.27, 0.12 and 0.08, giving dimensional values for $\max \Delta s^r$ of 2 m, 10 m and 59 m (for $Q/T = 10^2$ m, 10^3 m and 10^4 m).

Following a similar approach, we can explore the range of distances between which the effect of the barrier during pumping is not significant, but the barrier is not

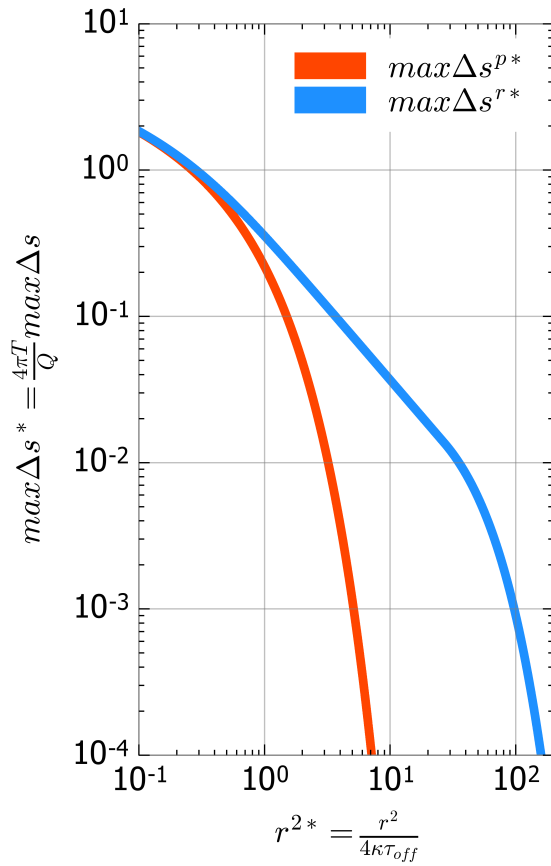


Figure 2.3: Generalised graph of maximum difference in drawdown between the one barrier case and the no barrier case during pumping (in *red*) and recovery (in *blue*), where $r = R = L$, as a function of non-dimensional distance (r^{2*}).

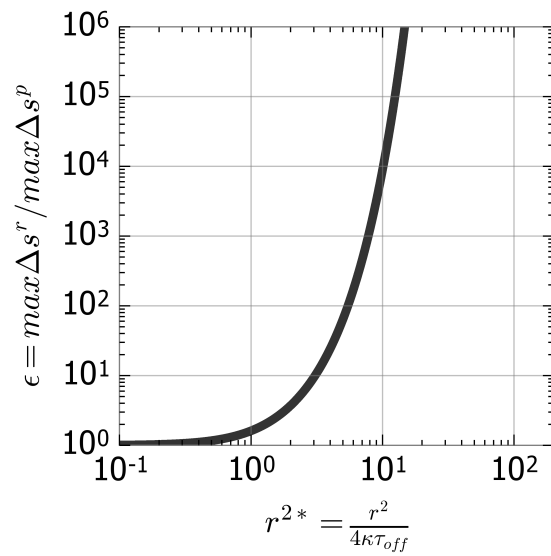


Figure 2.4: Generalised graph of the ratio of the maximum difference in drawdown between the barrier and no barrier case during pumping compared to recovery (ϵ), where $r = R = L$, as a function of r^{2*} .

too far away—so that its effect during recovery is significant ($\max \Delta s^p \leq 1$ m yet $\max \Delta s^r \geq 1$ m). We refer to these barriers as ‘undetected’ as hydraulic head measurements taken during pumping are not useful to predict recovery drawdown. From Figure 2.3, these are: $1.4 \leq r^{2*} \leq 2.9$, $3.0 \leq r^{2*} \leq 29$, $4.9 \leq r^{2*} \leq 91$ for $Q/T = 10^2$ m, 10^3 m and 10^4 m, respectively. For a system with $\kappa = 500$ m²/day and $\tau_{off} = 10$ years, these non-dimensional values of r^{2*} equate, respectively, to r values of 3140–4620 m, 4700–14,630 m, and 5990–25,800 m. Within these ranges of distance, ϵ respectively spans 2.0–8.7; 10.0 – 2.0×10^{12} and 59.0 – 4.5×10^{38} (Figure 2.4). This illustrates that the effect of the barrier during recovery is considerably greater than the effect of the barrier during pumping. However, as demonstrated, to determine the significance of the effect of the barrier during recovery one cannot simply refer to ϵ . This is because at high values of ϵ , the actual difference in drawdown induced by the barrier may be minor even if the ratio is large (as $\max \Delta s^p$ approaches zero).

To exemplify the method and results, we analyse a hypothetical but realistic mining project that exists within a regional aquifer in which there is an observation well (say, at the site of a valued ecosystem) located on the pumping well side of a barrier 3 km away from the pumping well (see Figure 2.1 where $r = R = L = 3000$ m). The barrier has not been identified prior to the commencement of the project. Let us assume that dewatering proceeds for 10 years ($\tau_{off} = 3650$ days) where $Q = 10^5$ m³/day (this rate of dewatering is known to occur at large open pit mines, Cook et al. 2016). The other aquifer properties are $K = 0.04$ m/day, $S = 0.1$, $b = 300$ m ($\kappa = 120$ m²/day); giving $r^{2*} = 5$. Although the drawdown at the observation well during pumping is small, residual drawdown during the recovery phase is significant (Figure 2.5). The maximum effect of the barrier during the pumping period, $\max \Delta s^p$, equals 0.7 m, and so the presence of the barrier is unlikely to be detected during pumping. After pumping ceases, as the extent of drawdown reaches the barrier, the residual drawdown curves for the barrier and the non-barrier model results diverge. The barrier-case residual drawdown curve is steeper than the non-barrier curve, as the barrier compartmentalises the aquifer and less water is available on the pumping side of the barrier for water level recovery. During the recovery phase, the maximum difference between the barrier and non-barrier model results ($\max \Delta s^r$) is 47 m observed at a t_{max}^r of 20,693 days (56 years), which is 46 years after the cessation of pumping. The value of ϵ for this example is 67, as the maximum effect of the barrier is considerably greater during recovery than during pumping, which highlights the importance of identifying barriers through other methods, such as hydrogeological mapping and geophysics, as their impact on water levels is delayed beyond the cessation of pumping.

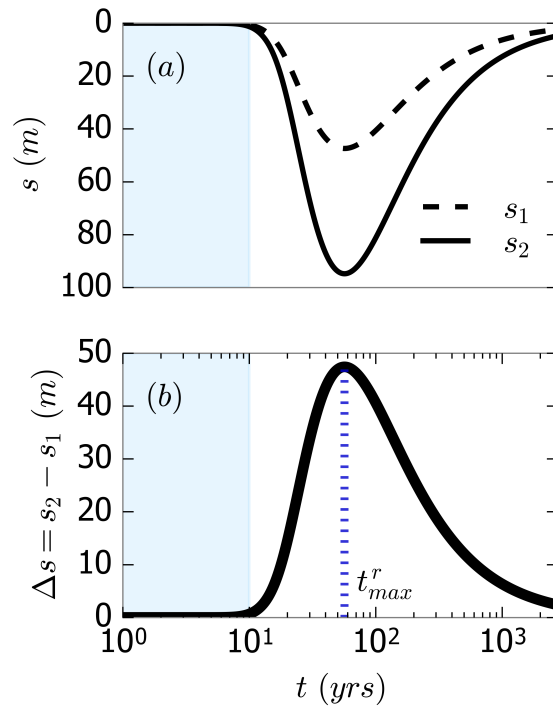


Figure 2.5: Results of analytical simulation of extraction and recovery for an aquifer 300 m thick, where $Q = 10^5 \text{ m}^3/\text{days}$, $r = 3000 \text{ m}$ with $K = 0.04 \text{ m}/\text{days}$ ($T = 12 \text{ m}^2/\text{days}$), and $S = 0.1$. The *blue shaded area* denotes the period of pumping, where $\tau_{off} = 10$ years. (a) Groundwater drawdown for the no barrier case (s_1) and the one barrier case (s_2); (b) the difference between drawdown with and without the barrier ($\Delta s = s_2 - s_1$). t_{max}^r is the time where Δs is the greatest, which occurs at 56 yrs.

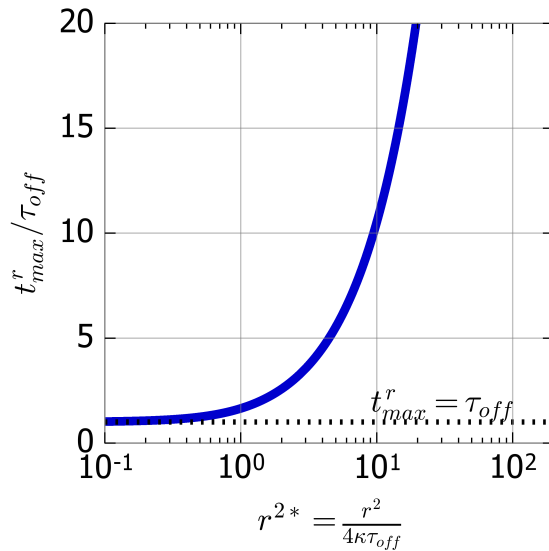


Figure 2.6: The time that the maximum effect of the barrier occurs (t_{max}^r) as a ratio to pumping duration (t_{max}^r/τ_{off}) compared to r^{2*} .

2.5 Timing of the maximum effect of a barrier

The solution to Equation 2.10 for $r = R = L$ enables the comparison of the ratio of t_{max}^r to τ_{off} with r^{2*} (Figure 2.6). This shows when the maximum effect of the barrier in recovery will occur, compared to the total duration of pumping. As r^{2*} increases, t_{max}^r increases with respect to τ_{off} . As r^{2*} decreases, $\frac{t_{max}^r}{\tau_{off}}$ decreases and approaches 1. For $\max \Delta s^p = 1$ m, and $Q/T = 10^2$ m, 10^3 m and 10^4 m, $\frac{t_{max}^r}{\tau_{off}} = 2.0$, 3.6 and 5.5, respectively. This means that, say for a groundwater extraction project that extends for 10 years ($\tau_{off} = 10$ years), the greatest effects of the barrier will not be until 10, 26 or 45 years after pumping ceases for these values of Q/T .

2.6 Groundwater drawdown and recovery with two orthogonal barriers

If there is more than one impermeable barrier, the effect of the barriers on drawdown will be greater than in the single barrier case, as the aquifer becomes more compartmentalised. We study the effect of two orthogonal barriers, with an observation well located on the pumping side of the junction of these barriers, as a case study to exemplify highly compartmentalised systems. In this case, the radial distance from each of the real or imaginary discharging wells will be equal ($r = R_{i1} = R_{i2} = R_{i3}$). Under this assumption, Equation 2.6 simplifies to Equation 2.13, and Equation 2.7 simplifies to Equation 2.14:

$$s_2^p = -\frac{Q}{4\pi T} \left(4\text{Ei} \left(\frac{r^2}{4\kappa t} \right) \right), \quad (2.13)$$

$$s_2^r = -\frac{Q}{4\pi T} \left(4\text{Ei} \left(\frac{-r^2}{4\kappa t} \right) \right) + \frac{Q}{4\kappa T} \left(4\text{Ei} \left(\frac{-r^2}{4\kappa(t - \tau_{off})} \right) \right). \quad (2.14)$$

Note that in this case, as the observation well is immediately adjacent to the junction of the two barriers, $r \neq L$, and thus the barriers are each closer to the pumping well than in the one barrier scenario. Therefore, in this case r represents the distance to both barriers, where they intersect, so in the two barrier scenario: $L_1 = L_2 = \sqrt{r^2/2}$. During both pumping and recovery, $\max \Delta s^*$ decreases with increasing r^{2*} . In comparison to the one barrier solution, overall the values are higher (Figure 2.7). The values of r^{2*} , for which $\max \Delta s^p \leq 1$ m, and $\max \Delta s^r \geq 1$ m, are $2.1 \leq r^{2*} \leq 8.8$, $3.9 \leq r^{2*} \leq 59$ and $5.9 \leq r^{2*} \leq 127$ for $Q/T = 10^2$ m, 10^3 m and 10^4 m, respectively. Respective values of ϵ are 4 to 2.6×10^3 , 22 to 7.6×10^{24} and 149 to 1.9×10^{51} , which can be found using the results for the one barrier case (Figure 2.4), as the ratio $\max \Delta s^r : \max \Delta s^p$ compared to r^{2*} is the same for both case studies. In the two orthogonal barrier case, the values of $\max \Delta s^r$ (for $\max \Delta s^p = 1$ m) are 4 m, 22 m and 149 m.

To determine the timing of the maximum effect of the impermeable barrier, where $r = R_{i1} = R_{i2} = R_{i3}$, and for $t > \tau_{off}$, Equation 2.11 simplifies to become the same as Equation 2.10 and the value of t_{max}^r can be determined using Figure 2.5. For the three values of Q/T described earlier, at $\max \Delta s^r$, where $\max \Delta s^p = 1$ m: $\frac{t_{max}^r}{\tau_{off}} = 2.7$; $\frac{t_{max}^r}{\tau_{off}} = 4.5$; and $\frac{t_{max}^r}{\tau_{off}} = 6.4$, respectively. This shows that for a groundwater extraction project that extends for 10 years ($\tau_{off} = 10$ years), the effect of the barriers will be greatest at 17, 35 or 54 years after pumping ceases if $Q/T = 10^2$ m; $Q/T = 10^3$ m or $Q/T = 10^4$ m, respectively.

2.7 Maximum error in predictions of hydraulic head during recovery

It is also useful to understand: (a) how large the effect of an undetected barrier could be in recovery for any given Q/T and (b) the distances, r , for which this phenomenon may be observed with respect to aquifer and pumping properties. To do this, for each value of Q/T , we can find the value of $\max \Delta s^{p*}$ where $\max \Delta s^p = 1$ m. From this we can derive the corresponding value of r^{2*} (Figure 2.3 or Figure 2.7), and thus also $\max \Delta s^{r*}$ and hence Δs^r . This is shown in Figure 2.8. As Q/T increases, so do $\max \Delta s^r$ and r^{2*} . For values of Q/T between $1-10^4$ m, the non-dimensional

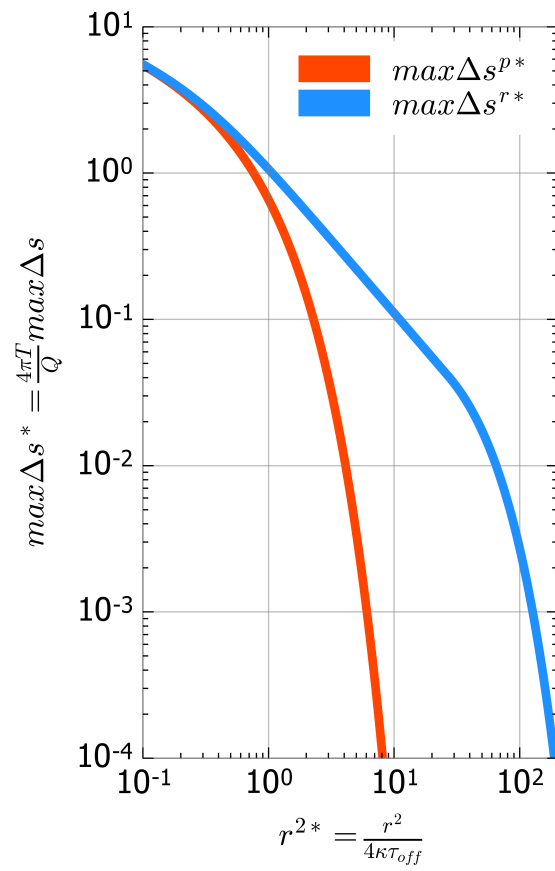


Figure 2.7: Generalised graph of maximum difference in drawdown between the two orthogonal barriers case and the no barrier case during pumping (in *red*) and recovery (in *blue*), where $r = R = L$, as a function of non-dimensional distance (r^{2*}).

values of r^{2*} that results in $\max \Delta s^p = 1$ m range between 0.01–10. The dimensional values of r can be derived by dividing r^{2*} by a specific value of $4\kappa\tau_{off}$. For example, if $Q/T = 10^2$ m, for values of $\kappa\tau_{off}$ between 10^6 – 10^8 m², r ranges between 10^3 and 10^5 m.

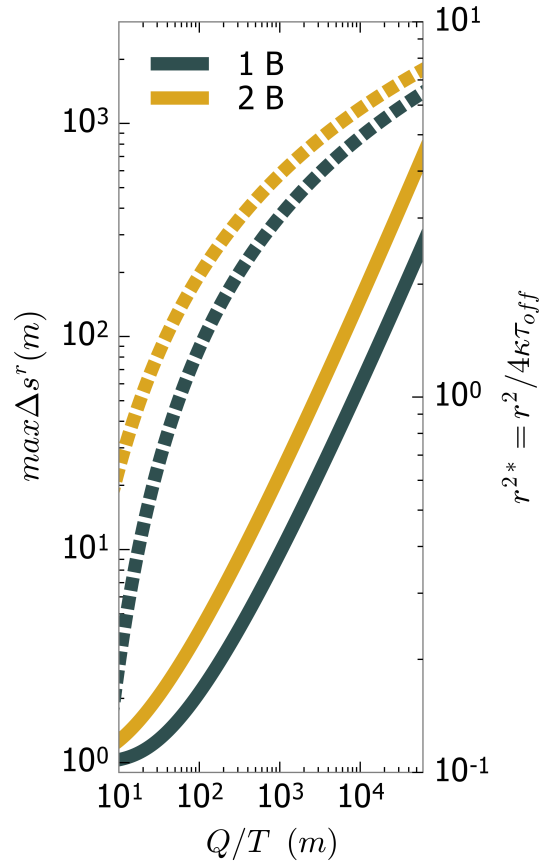


Figure 2.8: The value of $\max \Delta s^r$ for an undetected barrier, where $\Delta s^p = 1$ m, depending on the value of Q/T is shown by the *solid lines* for both the one barrier case (*1 B*) and two orthogonal barrier case (*2 B*). The r^{2*} corresponding to each $\max \Delta s^r$ value for a specific Q/T value is depicted with the *hashed lines*. These r^{2*} values can be used to calculate dimensional values of r , in metres, by dividing them by a specific value of $4\kappa\tau_{off}$.

2.8 Discussion and conclusions

This paper shows that in areas with impermeable barriers, hydraulic head measurements made during pumping cannot reliably be used to predict recovery. This can occur if impermeable barrier(s) exists outside the extent of drawdown induced during pumping. The results indicate that, for an observation well located 3 km from a pumping project, the effect of a barrier on groundwater levels can be less than 1 m during pumping, yet almost 50 m after pumping has ceased. The timing of the

maximum effect of a barrier on groundwater levels is proportional to the duration of pumping and will increase as the distance of the barrier from a pumping project increases.

The results were based on analytical models that used the linearised Boussinesq equations (Dupuit assumption). Other assumptions include: that the hydraulic barrier is completely impermeable, of infinite length, fully penetrating and that the aquifer is homogeneous. Our model of hydraulic barriers is thus highly simplified, and does not consider the permeability structure associated with fault zones (Bense et al. 2013; Caine et al. 1996). We also do not consider multi-aquifer systems in which faults create offsets on aquifer layers, or faults that act as barriers to perpendicular flow across the fault but as a conduits to flow in the vertical direction or along, parallel to, the fault. Steady state analytical models of these systems have been considered (Anderson and Bakker 2008; Anderson 2006). Further research into methods for modelling barriers with complex permeability and isotropy under transient conditions would be useful, where numerical modelling and field studies could complement the use of analytical or analytical-element models. The assumptions of zero permeability and isotropy across barriers in this paper allow for a worst-case assessment of omitting impermeable barriers from predictive models of groundwater levels based on hydraulic head measurements taken during pumping.

Where the effect of a barrier during pumping is insignificant, other methods are required to detect its presence. These might include surface or aerial geophysics (Ball et al. 2010; Vittecoq et al. 2015), geochemistry and environmental tracers (Pereira et al. 2010; Rajabpour and Vaezihir 2016; Sun et al. 2018; Toutain and Baubron 1999; Umeda and Ninomiya 2009), and lineament analysis (Per et al. 1997; Tam et al. 2004). Analysis of the pre-pumping potentiometric surface might also provide information on the existence of barriers to flow (Bense et al. 2003; Seaton and Burbey 2005), although often bore networks are sparse in areas that are not affected by groundwater pumping. This is certainly the case in northwest Australia, where dewatering of large open pit mines occurs in areas of highly complex geology (Cook et al. 2016). Nevertheless, the use of multiple data sets, such as geochemistry, temperature and hydraulic heads, can shed light on past and current groundwater dynamics in regions impacted by pumping (Gumm et al. 2016). However, interpreting variations in hydraulic conductivity and geological structures from some methods can be challenging (Viezzoli et al. 2013). Therefore, simple approaches to understand the impact of impermeable barriers on predictions of future groundwater levels can be very useful.

Chapter 3

Conjoint use of hydraulic head and groundwater age data to detect hydrogeologic barriers

Citation for published article: Marshall, S. K., P. G. Cook, L. F. Konikow, C. T. Simmons, S. Dogramaci, 2020. Conjoint use of hydraulic head and groundwater age data to detect hydrogeologic barriers. *Hydrogeology Journal* 28: 1003–1019

3.1 Abstract

Hydraulic head and groundwater age data are effective in building groundwater system understanding. Yet their joint role in detecting and characterising low-permeability geological structures—hydrogeologic barriers, such as faults and dykes, has not been widely studied. Here, numerical flow and transport models, using MODFLOW-NWT and MT3D-USGS, were developed with different hydrogeologic barrier configurations in a hypothetical aquifer. Computed hydraulic head and groundwater age distributions were compared to those without a barrier. The conjoint use of these datasets helps in detecting vertically-oriented barriers. Two forms of recharge were compared: (1) applied across the entire aquifer surface (uniform), and (2) applied to the upstream part of the aquifer (upgradient). The hydraulic head distribution is significantly impacted by a barrier that penetrates the aquifer’s full vertical thickness. This barrier also perturbs the groundwater age distribution when upgradient recharge prevails. However, with uniform recharge, groundwater age is not successful in detecting the barrier. When a barrier is buried (such as by younger sediment), hydraulic head data also do not clearly identify the barrier. Groundwater age data could, on the other hand, prove to be useful if sampled at depth-specific

intervals. These results are important for the detection and characterisation of hydrogeologic barriers, which may play a significant role in the compartmentalisation of groundwater flow, spring dynamics, and drawdown and recovery associated with groundwater extraction.

3.2 Introduction

Hydrogeologic barriers, including some dykes and faults, are structures that cut off or restrict groundwater flow (Ferris et al. 1962). Detecting hydrogeologic barriers in the subsurface is important because they can compartmentalise groundwater flow (Ferrill et al. 2004; Marshall et al. 2019) and provide a mechanism for spring and wetland formation (Babiker and Gudmundsson 2004; Bense et al. 2013). Steep hydraulic head gradients have been observed across hydrogeologic barriers under natural flow regimes; therefore, detailed potentiometric surface mapping can assist in their identification (Bense and Van Balen 2004; Bense et al. 2003; Ciloni et al. 2015; Stamatis and Voudouris 2003). Yet hydraulic head distributions may not definitively indicate the presence of barriers, particularly if the sampling density is low (Bredehoeft et al. 1992; Smerdon and Turnadge 2015). Although the response of hydraulic head to groundwater pumping can be useful for detecting hydrogeologic barriers (Kruseman and Ridder 2000), the long-duration pumping often required is not always feasible (Singh 2001).

Hydrochemical methods can provide useful information about groundwater flow in regions with hydrogeologic barriers. These have proven useful to identify vertical groundwater flux along faults. For example, Batlle-Aguilar et al. (2017) used major ions, isotopic tracers and dissolved gases to present evidence for mixing of older (upwelling) and younger (infiltrating) groundwater along permeable faults. Stable isotopes, dissolved gases, and temperature data were used by Gumm et al. (2016) to uncover the importance of deep, old groundwater mixing with shallow, young groundwater via faults. Vertical gas exhalation from faults has also been used for their detection and characterisation (Sun et al. 2018; Umeda and Ninomiya 2009). However, these approaches rely on the fault causing connectivity between deep and shallow aquifers, which is not always the case. Hydrochemical approaches can also unravel groundwater flow mechanisms across geologic structures in the horizontal direction. Analytical and numerical methods have illustrated discrete barrier features that displace and widen solute plumes (Sebben and Werner 2016). Field studies demonstrate the relevance of geochemical data, such as ratios of magnesium to calcium in groundwater (Valdes et al. 2007), and discontinuities in total dissolved solids (Rajabpour and Vaezihir 2016), to map fault properties. Geochemistry can also infer

connectivity between aquifers separated by horizontal flow barriers (Apaydin 2010). However, most previous studies are conducted with knowledge of the approximate location of the fault, with geochemistry refining fault properties. Studies that locate new structures using geochemistry are not as common. Advances in inverse methods, however, demonstrate capacity in this area (Comte et al. 2017; Dai et al. 2010; Harp et al. 2008).

Due to the restriction of groundwater flow across a fault or dyke, these structures can impact groundwater velocities. Therefore, they can influence groundwater age, which is usually estimated by measuring environmental tracers in groundwater (Cook and Böhlke 2000). Two-dimensional modelling of the Carrizo Aquifer in Texas showed reduced groundwater velocity downstream of a low-permeability fault, resulting in significantly older groundwater than would have occurred without the fault present (Castro and Goblet 2005). Raiber et al. (2015) examined the influence of regional faults on the interpretation of groundwater age (from radiocarbon data) using the conceptual framework of a 3D geologic model. They found unexpectedly older ages upgradient of some faults, interpreted as groundwater upwelling along the fault. They also found downgradient increases in groundwater age across faults, interpreted as potential leakage through faults from younger, shallower, aquifers. Groundwater age data are known to be useful for model calibration (Konikow et al. 2008; Sanford 2011), but few examples exist that jointly use hydraulic head and groundwater age to detect aquifer structures.

This study uses computer simulations of flow and transport in synthetic, regional-scale aquifers to determine the influence that vertically-oriented hydraulic barriers have on the spatial distribution of hydraulic head and groundwater age. The objective is to determine the detectability of barriers under contrasting recharge settings and barrier configurations. The detection, and any further characterisation, of barriers relies inherently on the availability of data. The objective of this study is not to quantitatively address the impact of data density on barrier detection. Instead, the focus is on when, and to what degree, hydraulic head and groundwater age data may be useful in detecting barriers in simple aquifer systems. This provides a reference for future studies in the vicinity of low-permeability aquifer structures that may involve, for example, the design of monitoring networks, the interpretation of more complex field data or the inversion of similar datasets, such as for model calibration.

3.3 Methods

Evaluating the effect of hydrogeologic barriers on hydraulic head and groundwater age distributions was achieved by first modelling a steady-state flow field with no barrier (Baseline). To understand the difference between Baseline (homogeneous) conditions and those with a barrier, two alternative barrier configurations were simulated. One represents a barrier that fully penetrates the entire depth of the aquifer, and the other a fault or dyke that has been overlain by younger, undeformed (or unintruded), sediment (e.g. Rajabpour and Vaezihir 2016). Two alternative spatial patterns of recharge were applied and the simulations with a barrier were compared to those for the Baseline case.

3.3.1 Theory and numerical models

Groundwater flow was simulated using the MODFLOW-NWT model (Niswonger et al. 2011). Age concentrations were calculated with MT3D-USGS (Bedekar et al. 2016) using direct age simulation (Goode 1996). The model simulates age as a non-reactive solute species using a zeroth order production term to allow water to “age” by one unit of time per unit time. This approach is useful to understand the distribution of groundwater age in the system, based on flow and transport properties. The models were developed and post-processed using the FloPy package for Python (Bakker et al. 2016) and were executed utilising high-performance computing provided by eResearch SA Ltd (eRSA). The flow model equations were solved using the Newton solver with a $1e-5$ m head change convergence criterion. The advective-dispersive transport equation was solved using the standard finite-difference method, due to its superior numerical efficiency. Unlike point-source problems, numerical dispersion was not considered as a significant problem for the calculation of an “age concentration,” which is dominated by advection and the zero-order reaction term. A convergence criterion of $1e-6$ in terms of relative concentration was used. The flow and transport models were executed as steady-state simulations. The results were compared to transient transport model simulations, run for a sufficiently long time to reproduce steady-state conditions, and were in agreement.

3.3.2 Conceptual models

The conceptual models were designed to evaluate groundwater flow in a large, regional-scale groundwater system in a semiarid to arid climate. The Baseline model provides a basis for comparison of potential barrier conditions; it has homogeneous aquifer properties and includes no hydrogeologic barrier. For simulations with a barrier, the hydraulic conductivity in cells representing the barrier is three orders of

magnitude lower. Porosity remains constant across the grid. The dimensions of the model are 10 km by 5 km, with a thickness of 300 m. The model domain is divided into a regular rectangular grid. In the x and y directions, cells have dimensions of 10 m by 10 m. The model is vertically discretised into 12 layers, each 25 m thick. The robustness and resolution of the flow and transport solutions were tested using more finely discretised grids and the results indicated grid convergence. Dimensions and parameters used for each model are shown in Table 3.1.

Parameter	Symbol	Value
<i>MODFLOW-NWT</i>		
Grid size (x and y directions) [m]	$\Delta x, \Delta y$	10
Layer thickness [m]	Δz	25
Anisotropy ratio	K_h/K_y	10
Specific yield	S_y	0.1
Recharge rate [m/d]	R	1.37e-5
Hydraulic conductivity - aquifer [m/d]	K_a	1
Hydraulic conductivity - barrier [m/d]	K_b	1e-3
Barrier width (along x axis) [m]	W_b	50
<i>MT3D-USGS</i>		
Effective porosity	η_e	0.1
Zeroth order reaction rate [yr/d]		1/325.25
Longitudinal dispersivity [m]	α_L	1.5
Ratio of horizontal transverse dispersivity to longitudinal dispersivity	α_{TH}/α_L	0.1
Ratio of vertical transverse dispersivity to longitudinal dispersivity	α_{TV}/α_L	0.01
Effective molecular diffusion coefficient [m ² /d]	D^*	92-6

Table 3.1: Dimensions and universal parameters for modelling various barrier and recharge configurations.

The upstream end, the two lateral sides, and base of the aquifer were assigned no-flow conditions and the downstream end has a fixed general head boundary (Figure 3.1). The upper surface of the model was simulated as water table (unconfined) conditions. The only inflow to the system is via recharge. The first Uniform spatial pattern of recharge represents diffuse recharge from rainfall infiltration evenly across the region. The second Upgradient spatial pattern of recharge involves recharge only in the upper part of a catchment. This might occur for a confined aquifer that outcrops in the upper part of the catchment, but might also occur in unconfined aquifers in semi-arid to arid climates that are dominated by mountain front recharge (e.g. Manning and Solomon 2003). A value of 5 mm/yr for the Uniform recharge scenario is consistent with values estimated for semi-arid regions of Australia (Cook et al. 2016), and the same volume of recharge converts to a rate of 20 mm/yr when only applied to the upper quarter of the catchment. These values were chosen as the

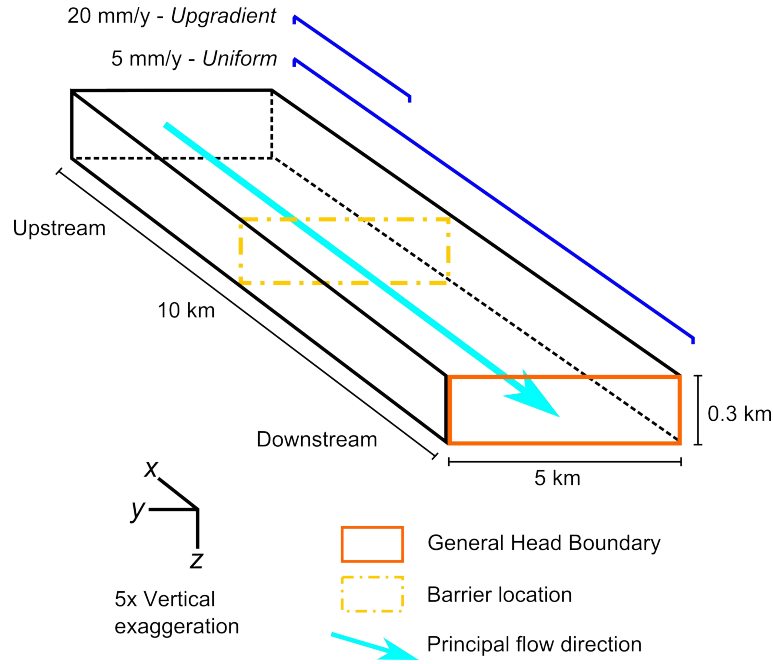


Figure 3.1: Schematic, 3D representation of the simulation domain showing the model dimensions and boundary conditions. The *yellow dot-dash lines* illustrate the central position of a barrier, for relevant cases. The two *navy blue lines* represent the physical extent to which recharge was applied to the uppermost cells in the model for each recharge scenario (recharge applies to all values of y). The *orange model face* indicates where a general head boundary was applied and the *black model faces* indicate those to which no-flow conditions were applied, except the upper x - y model face, which was simulated as water table conditions. The *light blue arrow* shows the principal groundwater flow direction.

work forms part of a larger project assessing groundwater resources in the semi-arid Pilbara region of Western Australia (Manning and Solomon 2003; Underwood et al. 2018).

Transport simulations were performed over the entire grid, where recharge water had an age concentration of zero. The results assess the relative differences in groundwater age, as described below, and the spatial distribution of these differences. As differences are measured, the absolute values of recharge are less relevant to the overall results of the study, as both models being compared were parameterised identically, except for the presence or absence of a barrier. Nevertheless, the absolute values of recharge and other parameters, including hydraulic conductivity, porosity, barrier width, and the ratio of the aquifer to barrier hydraulic conductivities, were assessed in a sensitivity analysis. Two alternative barrier configurations were simulated (Figure 3.2). The Fully-penetrating barrier penetrates all model layers, but not the entire width of the model so that some groundwater can flow laterally around it. The Buried barrier only penetrates the lower half of model layers. In this case, the barrier extends the entire aquifer width. The barrier width (extent

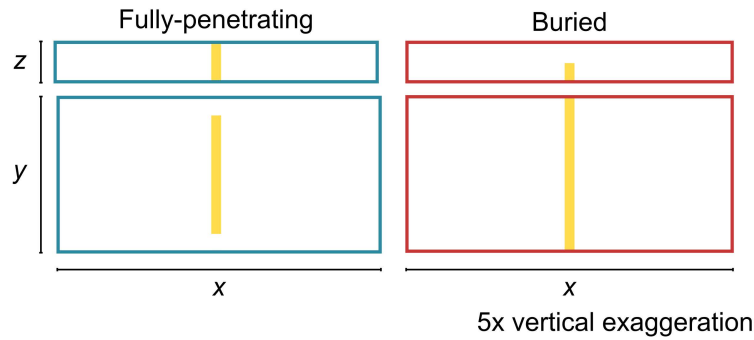


Figure 3.2: Schematic cross-section and plan-view illustrations of the barrier configurations. The *upper rectangle* for both the Fully-penetrating (in *blue*) and the Buried (in *red*) barrier scenarios represent the aquifer in cross-section, taken through the centre of the *y axis* of the model. The lower rectangles represent the aquifer in plan-view, taken from the base of the *z axis* of the model. Note that for the Buried barrier case a plan-view slice through the upper half of the aquifer would display no barrier. The *yellow line* represents the location of a barrier, which is 50 m wide (not to scale).

along *x axis*) is 50 m in all cases.

3.3.3 Hydraulic head and groundwater age difference

To understand how hydrogeologic barriers impact hydraulic head and groundwater age distributions, the differences between these variables in the simulations with and without a barrier were compared. The model difference for hydraulic head (Δh) and groundwater age (Δa) was calculated by subtracting the value for hydraulic head or groundwater age (respectively) at each cell for the Baseline model (with no barrier) from the value at the corresponding cell in the model with a barrier:

$$\Delta_{x,y,z}^h = h_{x,y,z}^b - h_{x,y,z}^{nb}, \quad (3.1)$$

where h^b is the hydraulic head in the case with a barrier and h^{nb} is the hydraulic head without a barrier. The subscripts x , y , z refer to the model cell positions along the x , y , and z axes of model, respectively.

Similarly, the difference in groundwater age was determined:

$$\Delta_{x,y,z}^a = a_{x,y,z}^b - a_{x,y,z}^{nb}, \quad (3.2)$$

where a^b is groundwater age with a barrier and a^{nb} is groundwater age without a barrier. The groundwater age difference was normalised using a fractional age difference, Γ^a (Zinn and Konikow 2007a), for all points in the model grid, defined

as:

$$\begin{aligned} \text{if } a_{x,y,z}^b \geq a_{x,y,z}^{nb}, \Gamma_{x,y,z}^a &= \frac{\Delta_{x,y,z}^a}{\Delta_{x,y,z}^{nb}}, \\ \text{if } a_{x,y,z}^b \leq a_{x,y,z}^{nb}, \Gamma_{x,y,z}^a &= \frac{\Delta_{x,y,z}^a}{\Delta_{x,y,z}^b}. \end{aligned} \quad (3.3)$$

The reason that Δ^a was normalised is because the detectability of a change in age will depend on the age of groundwater in the system. For example, a 100 yr difference in age may be relevant if the average age is 200 yr, but not necessarily if it is 2000 yr. This metric scales positive and negative changes in age in a constant fashion, where if age increased by a factor of 100, Δ^a would equal 99, and if age decreased by a factor of 100, Δ^a would equal -99, which is beneficial over a percent change measurement, as it doesn't disproportionately emphasise large increases in age over large decreases.

3.3.4 Extent of spatial impact of a barrier

The results for the values of Δ^h and Γ^a across the model were evaluated spatially. Here, absolute values of $|\Delta^h|$ and Γ^a were used to show how different the results with and without a barrier are, regardless of which is higher. The volume of the aquifer with a value of $|\Delta^h| > A$ was calculated, where A ranged from 0.1 m to the maximum value of $|\Delta^h|$ in increments of 0.005 m. Similarly, the volume of the aquifer with a value of $|\Gamma^a| > B$ was also calculated, where B ranged from 0.01 to the maximum value of $|\Gamma^a|$ at increments of 5e-4.

The volume of the aquifer for each value of $|\Delta^h|$ and $|\Gamma^a|$ was normalised by the cross-sectional area of the barrier (i.e. the area of the barrier in the $y - z$ plane). Because the barrier cross-sectional area is constant at 1.2 km² and 0.75 km² for the Fully-penetrating and Buried cases, respectively, these plots of normalised volume can be simply converted to true volumes. However, this normalisation was found to be useful, as it represents an "effective distance" from the barrier over which the relevant groundwater parameters have changed. This value is hence related to the distance from a barrier that a well would need to be located to detect such a change.

3.3.5 Change across the barrier

Changes in hydraulic head and groundwater age were calculated across (perpendicular to) the barrier. These results were examined in wells 25 m upstream and

downstream of the barrier. Because the barrier has a width of 50 m, the midpoints of the cells were 100 m apart. The changes in hydraulic head and groundwater age across the barrier were taken by subtracting the value at the upstream point (at $x = 4955$ m) from the downstream point (at $x = 5055$ m), at an equivalent position along the y and z axes. The change in hydraulic head across the barrier was calculated using:

$$\delta h_{y,z} = h^d - h^u, \quad (3.4)$$

where $\delta h_{y,z}$ is the linear change in hydraulic head across the barrier (m), h^d is the value of hydraulic head at the downstream location and h^u is the value of hydraulic head at the upstream location. Similarly, normalised age change across the barrier was calculated by:

$$\delta a_{y,z} = \frac{a^d - a^u}{0.5(a^d + a^u)}, \quad (3.5)$$

where $\delta a_{y,z}$ is the linear change in age across the barrier divided by the average of the two age values (unitless), a^d is the value of age at the downstream location and a^u is the value of age at the upstream location. The spatial patterns of hydraulic head and groundwater age along the barrier will be reflected in $\delta h_{y,z}$ and $\delta a_{y,z}$, which provide a simple proxy for the interpretation of field data across a barrier.

3.3.6 Baseline hydraulic head and groundwater age distributions

The Baseline conditions (Figure 3.3)—hydraulic head and groundwater age distributions without a barrier—show that the regional hydraulic head gradient with Uniform recharge (Figure 3.3a) is lower than that with Upgradient recharge (Figure 3.3c). The groundwater age with Uniform recharge (Figure 3.3b) increases with depth, but not in the principal direction of flow. In this case, the mean age in the aquifer ($\mu = 5662$ yr) is considerably higher than that for Upgradient recharge ($\mu = 3079$ yr). With Upgradient recharge, age increases in the direction of flow as the distance from the recharge region increases, but it varies less with depth (Figure 3.3d). The age distribution with Uniform recharge is similar to analytical expressions for an unconfined aquifer, where age is dependent on depth. Those with Upgradient recharge relate to a confined aquifer, where age also depends on the distance along the aquifer (Cook and Böhlke 2000). Under both recharge scenarios, the hydraulic head and groundwater age do not vary laterally across the aquifer (y direction). In

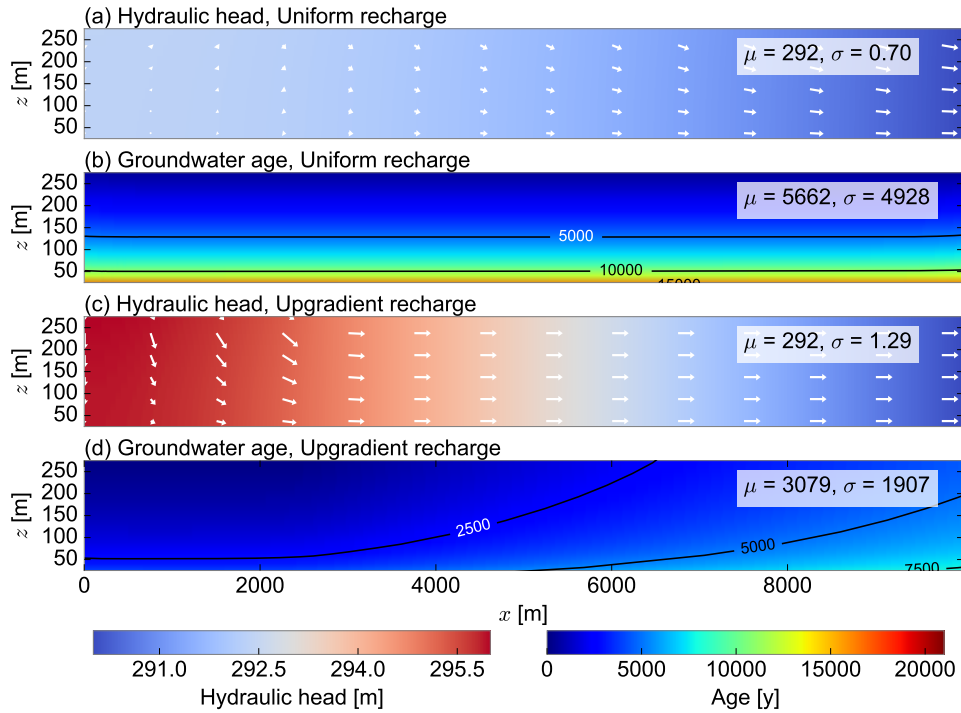


Figure 3.3: Baseline results with Uniform recharge (a, b) and Upgradient recharge (c, d) shown as a cross-section taken through the centre of the y axis of the model. Results show hydraulic head distributions (a, c) and groundwater age distributions (b, d). The arrows on (a) and (c) indicate groundwater flow direction with their length scaled arithmetically by the groundwater velocity.

this and all following sections, cross-section results refer to the $x - z$ plane taken through the centre of the y axis (at $y = 2500$ m). The arithmetic average value (μ) and standard deviation (σ) of hydraulic head, Δ^h , and normalised groundwater age, Γ^a , were calculated for the entire model grid, not only for the cross section or layer for which the results are illustrated.

3.4 Results

3.4.1 Hydraulic head and groundwater age differences

With the Fully-penetrating barrier, a decrease in hydraulic head is observed across the barrier, in the principal direction of groundwater flow. This is not as pronounced with Uniform recharge, where hydraulic head drop across the barrier is approximately 1.5 m (Figure 3.4a), as with Upgradient recharge, where the drop is approximately 2.5 m across the barrier (Figure 3.4d).

With a Fully-penetrating barrier and Uniform recharge, groundwater age does not change noticeably across the barrier (Figure 3.4b). The normalised age difference

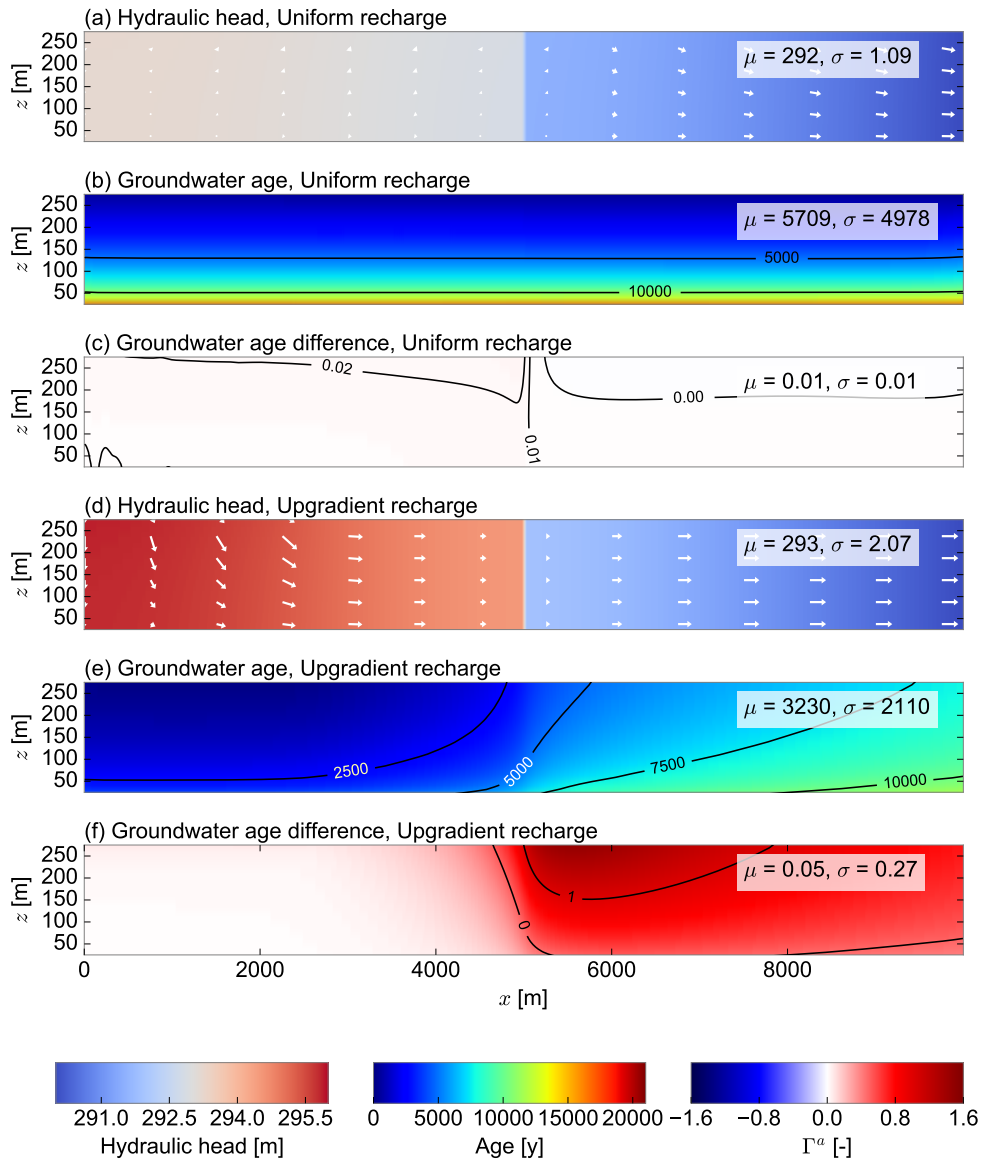


Figure 3.4: Fully-penetrating barrier results with Uniform recharge (a, b and c) and Upgradient recharge (d, e and f), shown as a cross-section taken through the centre of the y axis of the model. Results show hydraulic head distributions (a, d); groundwater age distributions (b, e); and normalised differences in groundwater age (c, f). The arrows on (a) and (d) indicate groundwater flow direction with their length scaled arithmetically by the groundwater velocity.

(Figure 3.4c) shows that groundwater is very slightly younger downstream of the barrier (at a shallow depth) that it would be without the barrier, and only very slightly older upstream of the barrier. This is because groundwater flow upstream of the barrier is obstructed (Figure 3.5a). Fresh water recharging downstream of the barrier is therefore not mixing completely with older water from upstream, especially in the shadow of the barrier, resulting in younger groundwater ages (Figure 3.5b). With Upgradient recharge, there is a sharp increase in age across the Fully-penetrating barrier in the direction of principal groundwater flow (Figure 3.4e). In parts of the aquifer, Γ^a reaches approximately 1.6 (Figure 3.4f), showing the difference in age between the case with and without a barrier is approaching twice the age of the groundwater. The barrier restricts groundwater flow, creating a high head gradient across the barrier (Figure 3.6a). Preferential flow around the barrier results in a “shadow” of comparatively older groundwater in line with, and downstream of, the barrier (Figure 3.6b).

With a Buried barrier (Figure 3.7), the hydraulic head distribution is very similar to Baseline conditions. There is, however, an upwards vertical head gradient on the upstream side of the barrier, and a downwards vertical head gradient on the downstream side of the barrier for both recharge scenarios. These vertical hydraulic head gradients are lower with Uniform recharge (Figure 3.7a), due to the lower flow rate. Nevertheless, this upstream vertical head gradient means that with Uniform recharge, old groundwater from the base of the aquifer is moving upwards and banking up, resulting in older groundwater upstream (Figure 3.7b). Groundwater with a barrier is older than Baseline conditions in the vicinity of the barrier (Figure 3.7c). Because the vertical head gradients either side of the barrier are more pronounced with Upgradient recharge (Figure 3.7d), the role of the barrier in restricting groundwater flow and influencing groundwater age is not as significant (Figure 3.7e). The Baseline system with this recharge scenario has less vertical variation in age so the upwards movement of groundwater over the barrier causes less of an impact on groundwater age in the vicinity of the barrier (Figure 3.7f).

3.4.2 Extent of spatial impact of a barrier

The likelihood of detecting a barrier depends on: (1) the magnitude of difference between the hydraulic head and groundwater age with and without a barrier; (2) the spatial extent of this difference; and (3) the accuracy and precision of measurements of hydraulic head and groundwater age. Here, the results are presented for the spatial extent of impact from a barrier. This provides information on the maximum distance from a barrier that wells could be located to reveal the barrier’s presence. The volume of aquifer over which the absolute difference in hydraulic head between

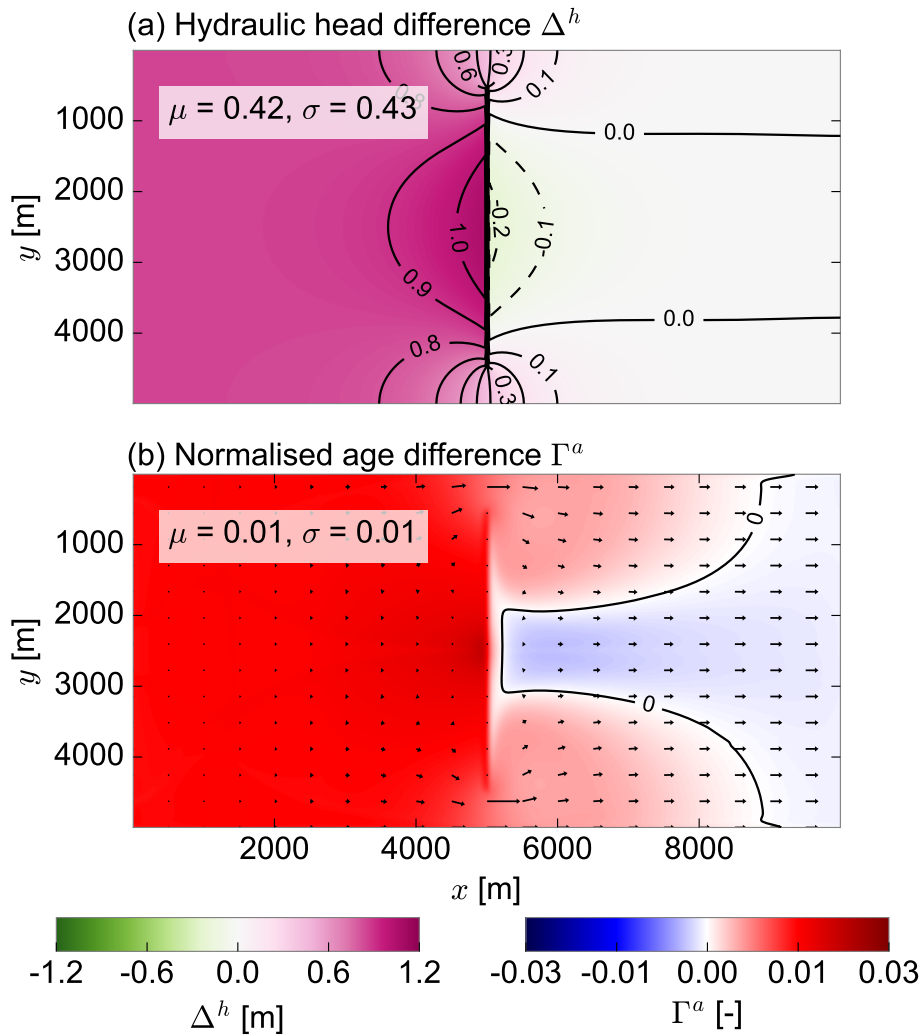


Figure 3.5: Hydraulic head difference (a) and normalised groundwater age difference (b) for the Fully-penetrating barrier with Uniform recharge, in a plan-view slice through the upper half of the z axis ($z = 237.5$ m). Positive values for both hydraulic head difference and normalised groundwater age difference indicate that the value for the barrier scenario is higher than that for the non-barrier scenario. The arrows on (b) indicate the groundwater flow direction, with their length scaled arithmetically by groundwater velocity. Contours are shown as solid or dashed black lines where the contour represents a positive or negative value, respectively.

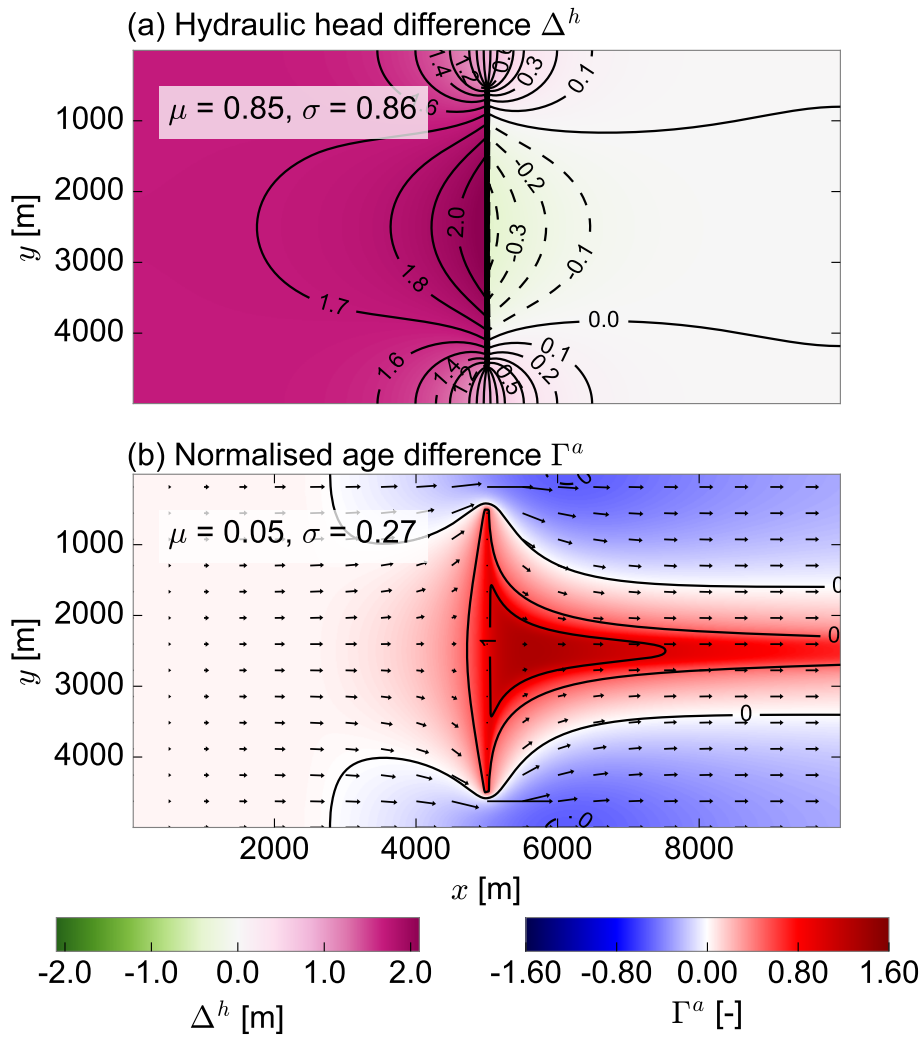


Figure 3.6: Hydraulic head difference (a) and normalised groundwater age difference (b) for the Fully-penetrating barrier with Upgradient recharge, in a plan-view slice through the upper half of the z axis ($z = 237.5$ m). Positive values for both hydraulic head difference and normalised groundwater age difference indicate that the value for the barrier scenario is higher than that for the non-barrier scenario. The arrows on (b) indicate the groundwater flow direction, with their length scaled arithmetically by groundwater velocity. Contours are shown as solid or dashed black lines where the contour represents a positive or negative value, respectively.

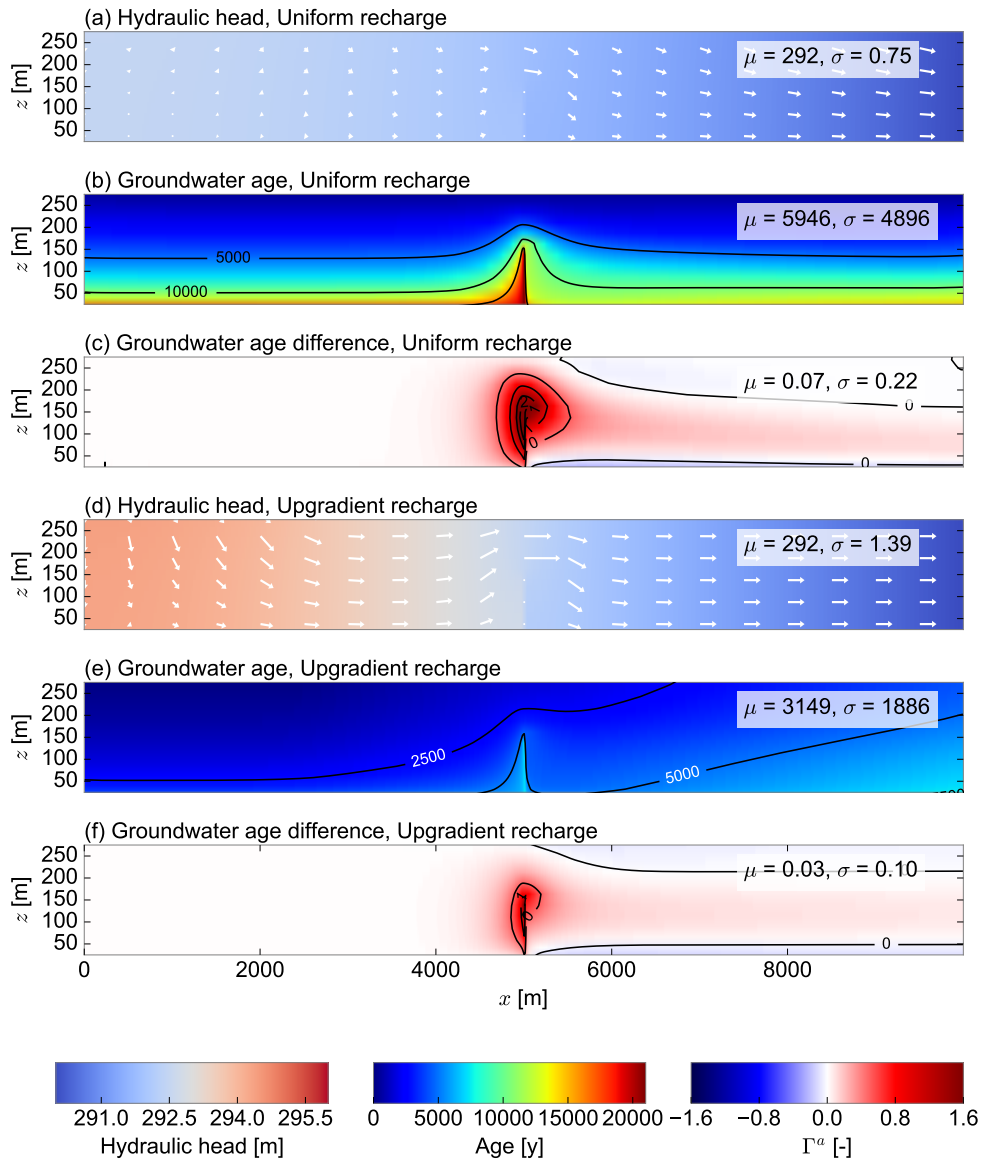


Figure 3.7: Buried barrier results with Uniform recharge (a, b and c) and Upgradient recharge (d, e and f), shown as a cross-section taken through the centre of the y axis of the model. Results show hydraulic head distributions (a, d); groundwater age distributions (b, e); and normalised differences in groundwater age (c, f). The arrows on (a) and (d) indicate groundwater flow direction with their length scaled arithmetically by the groundwater velocity.

the Baseline and barrier simulations ($|\Delta^h|$) exceeded different values was determined. This volume has been normalised by the cross-sectional area of the barrier (in the $y - z$ plane) to determine an “effective distance” of impact from the barrier. These results show that the Fully-penetrating barrier has a greater impact on hydraulic head than the Buried barrier, and that the magnitude of the head difference is greatest for the case with Upgradient recharge, reaching 2.2 m (Figure 3.8a).

A perturbation in hydraulic head was assumed to be detectable and significant if $|\Delta^h| \geq 0.5$ m. Using this cut-off value, for a Fully-penetrating barrier, hydraulic head is significantly perturbed over an effective distance between 6.3 and 6.4 km from the barrier. Yet with a Buried barrier, no hydraulic head difference would be detected, as it is less than 0.5 m across the whole aquifer. For groundwater age, the Fully-penetrating barrier with Upgradient recharge has the largest aquifer volume with the greatest values of absolute normalised age difference, $|\Gamma^a|$. Yet, when normalised to the cross-sectional area of the barrier, these results are similar to those for the Buried barrier with Uniform recharge (Figure 3.8b). In contrast, with Uniform recharge the Fully-penetrating barrier has the smallest impact on relative groundwater age.

The value of normalised groundwater age difference that is discernible in the field will depend on the method used to determine groundwater age. One estimate is that groundwater age can be estimated to within 20 % using certain environmental tracers (Cook and Solomon 1997). Evaluating the groundwater age estimation error using environmental tracers is, however, complicated. It will depend on many factors, such as dispersion, the age of the water itself, and the length of the well screens (Walker and Cook 1991; Zinn and Konikow 2007b). Nevertheless, a value of ($|\Gamma^a|$) ≥ 0.2 was adopted as a benchmark for understanding the field-scale detectability of the barriers. The effective distances from the barrier with ($|\Gamma^a|$) ≥ 0.2 are: 3.6 km, 2.4 km, and 0.9 km for the Fully-penetrating barrier with Upgradient recharge, the Buried barrier with Uniform recharge, and the Buried barrier with Upgradient recharge, respectively. For the Fully-penetrating barrier with Uniform recharge, none of the aquifer has a groundwater age more than 20 % different to the Baseline simulation.

3.4.3 Change across the barrier

The previous section compared differences in hydraulic head and groundwater age data with and without barriers. Here, the changes in hydraulic head and groundwater age across barriers are explicitly examined. As discussed above, the barrier is 50 m wide (along the x axis). The hydraulic head and groundwater age were examined 25 m upstream and downstream of the barriers—a distance of only 100 m, over

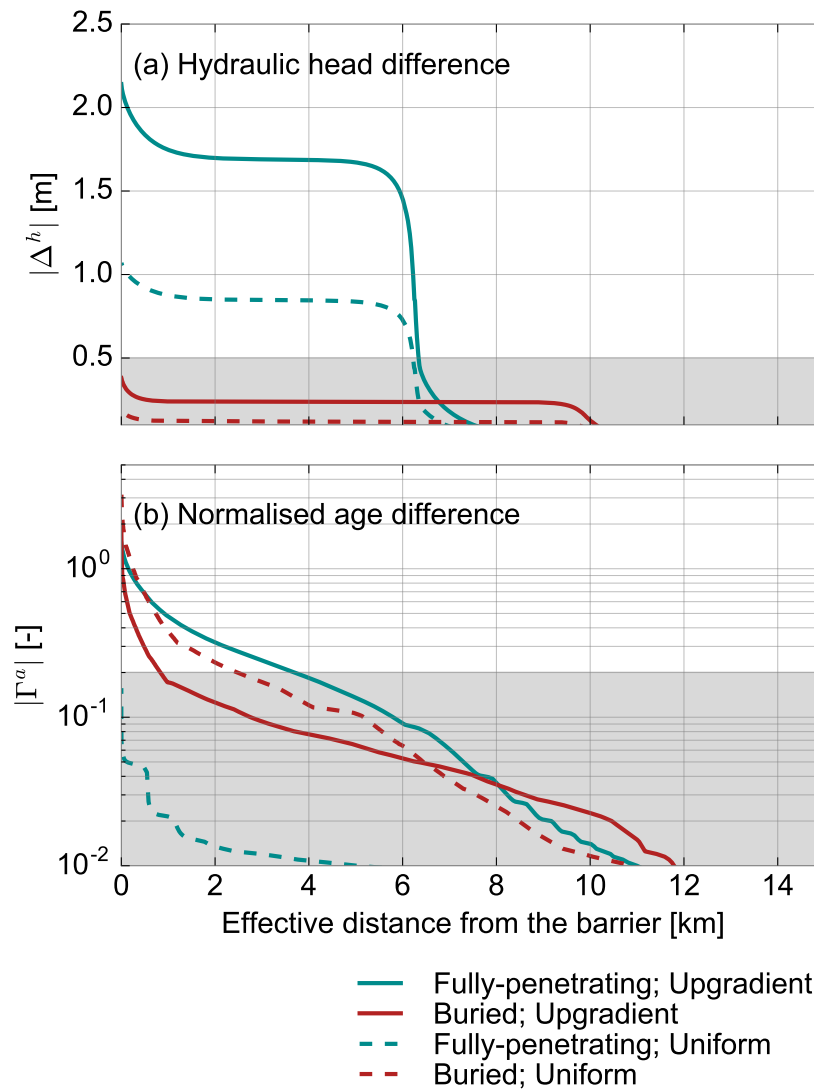


Figure 3.8: Cumulative plots displaying absolute (a) hydraulic head difference ($|\Delta^h|$), and (b) normalised groundwater age difference ($|\Gamma^a|$) compared to the “effective distance from the barrier.” The effective distance is the volume of aquifer normalised by the cross-sectional area of the barrier (1.2 km^2 and 0.75 km^2 for Fully-penetrating and Buried barriers, respectively). The values shaded in grey represent those that would not be detectable with measurement errors of 0.5 m for $|\Delta^h|$ and 0.2 for $|\Gamma^a|$.

which only very small differences in these variables would usually occur in a uniform aquifer. The hydraulic head and normalised groundwater age change across the barrier, $\delta h_{y,z}$ and $\delta a_{y,z}$, were calculated for each value along the y and z axes.

In the case with the Fully-penetrating barrier, values of $\delta h_{y,z}$ do not vary significantly with depth, but do vary with distance along the y axis. The results were therefore averaged along the z axis and compared along the y axis, denoted as $\delta h_{y\bar{z}}$. The value of $\delta h_{y\bar{z}}$ is greatest in the middle of the barrier (centre of the y axis) and decreases towards the barrier's edges (Figure 3.9a). It is higher with Upgradient recharge than Uniform recharge, with maximum values of $\delta h_{y\bar{z}}$ of -2.6 m and -1.3 m, respectively. Groundwater age change (normalised by the average groundwater age across the barrier) was also depth-averaged and compared across the y axis, denoted by $\delta a_{y\bar{z}}$. The value of $\delta a_{y\bar{z}}$ varies more along the barrier with Upgradient recharge compared to that with Uniform recharge (Figure 3.9b). With Upgradient recharge, $\delta a_{y\bar{z}}$ is the most positive in the centre of the barrier, reaching a value of approximately 0.12. Towards the edges of the barrier, it is -0.09, indicating that groundwater downstream is younger than upstream.

The results of $\delta h_{y,z}$ and $\delta a_{y,z}$ for the Buried barrier vary with depth, not length. They were, therefore, averaged along the y axis and compared along the z axis, denoted by $\delta h_{\bar{y}z}$ and $\delta a_{\bar{y}z}$. Values of $\delta h_{\bar{y}z}$ for both recharge scenarios are close to Baseline conditions in the upper half of the barrier (Figure 3.9c). Yet, in the lower half of the aquifer, where the barrier is present, values of $\delta h_{\bar{y}z}$ are more negative. The change in hydraulic head across the barrier is greater with Upgradient recharge compared to Uniform recharge. The change in groundwater age across the barrier $\delta a_{\bar{y}z}$ is approximately the same as Baseline conditions in the upper part of the aquifer (Figure 3.9d). Immediately above the barrier, $\delta a_{\bar{y}z}$ is at its most positive for both recharge scenarios, reaching 0.08. Groundwater is older (than without a barrier) downstream of the barrier and in the middle layer of the aquifer due to the shadowing effect of the barrier (see Figures 3.7c and 3.7f). In the lower half of the aquifer, $\delta a_{\bar{y}z}$ is at its most negative, reaching -0.39 for Uniform recharge. Downstream age is considerably younger than the upstream age at the same depth, because young groundwater flows over the top of the barrier and then downwards on the downstream side of the barrier (see Figure 3.7d).

3.4.4 Impact of barrier orientation

To understand the relation between the orientation of a barrier and the distributions of hydraulic head and groundwater age, simulations were made of the Fully-penetrating barrier oriented at different angles to the principal flow direction. In each simulation, the barrier penetrated all layers of the aquifer and was approxi-

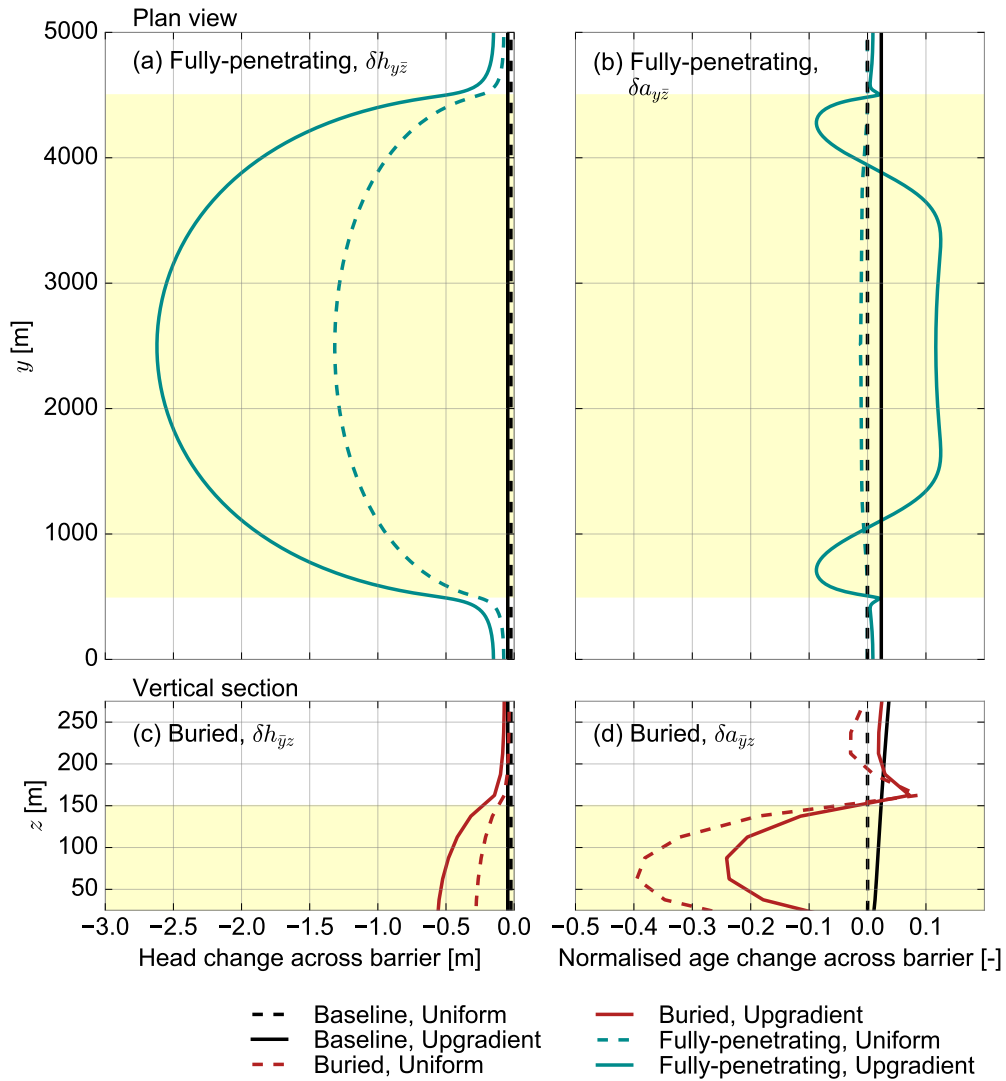


Figure 3.9: Plots showing change in hydraulic head and groundwater age over a 100 m distance across a barrier. The results show the depth-averaged change along the barrier plotted along the y axis for a Fully-penetrating barrier (in blue) for (a) hydraulic head and (b) normalised groundwater age; and the along-barrier averaged change plotted versus depth for a Buried barrier (in red) for (c) hydraulic head and (d) normalised groundwater age. Baseline conditions are shown by black lines. The barrier position is indicated by yellow shading.

mately the same length. (Small variations in length occurred due to the discrete cell size of the model grid.) An angle of 90° represents barriers that are orthogonal to the principal flow direction, as was the case for all previous simulations.

The effect of the barrier on the hydraulic head or groundwater age distribution decreases as the angle of the barrier decreases (Figure 3.10). If a value of $|\Delta h| \geq 0.5$ is again considered as measurable, then only barriers with angles $\geq 56.25^\circ$ will have a measurable impact on the hydraulic head distribution for Uniform recharge (Figure 3.10a), or $\geq 33.75^\circ$ for Upgradient recharge (Figure 3.10b). If $\Gamma^a \geq 0.2$ is again considered measurable, then no barrier orientations have a measurable impact on groundwater age distributions with Uniform recharge (Figure 3.10c). With Upgradient recharge (Figure 3.10d), on the other hand, the effective distance of impact from the barrier is: < 1 km for barriers oriented $0\text{--}22.50^\circ$; between 1–2 km for barriers oriented $33.75\text{--}45^\circ$; between 2–3 km for the barrier oriented at 56.25° ; and > 3 km for barriers oriented $67.5\text{--}90^\circ$ to the principal flow direction. Plan view plots for the middle layer of the aquifer for Upgradient recharge show where in the aquifer groundwater age differs from Baseline conditions (Figure 3.11). Low groundwater velocities resulting from obstruction by the barrier are more pronounced on one side of the barrier ($y = 0\text{--}2500$ m), meaning samples taken across the barrier on one end could have very different results from the other end of the barrier. The “shadow” of older groundwater, forming downstream of the barrier, is not symmetrical if the barrier is not orthogonal or parallel to the principal direction of groundwater flow.

3.4.5 Influence of aquifer properties

The dependence of hydraulic head and groundwater age distributions on aquifer and barrier properties has been assessed through sensitivity analyses for the Fully-penetrating barrier with Upgradient recharge. This case shows the largest effect on hydraulic head and groundwater age. If recharge is fixed, but the hydraulic conductivity of the aquifer, K_a , is decreased (with the same ratio of aquifer hydraulic conductivity to barrier hydraulic conductivity, K_b), then the hydraulic head difference, Δ^h , increases (Figure 3.12a) but the groundwater age distribution is largely unchanged (Figure 3.12b) as groundwater flux is unchanged. If recharge rate is decreased with a fixed K_a , results are similar to those for changing hydraulic conductivity. In addition, when aquifer hydraulic conductivity and recharge rate were changed simultaneously by the same proportional multiplier, no variation in the spatial distribution of hydraulic head or normalised groundwater age difference was observed. Increasing the porosity of the aquifer results in greater groundwater ages, but did not change the hydraulic head distribution or the relative age difference between the barrier and no barrier cases.

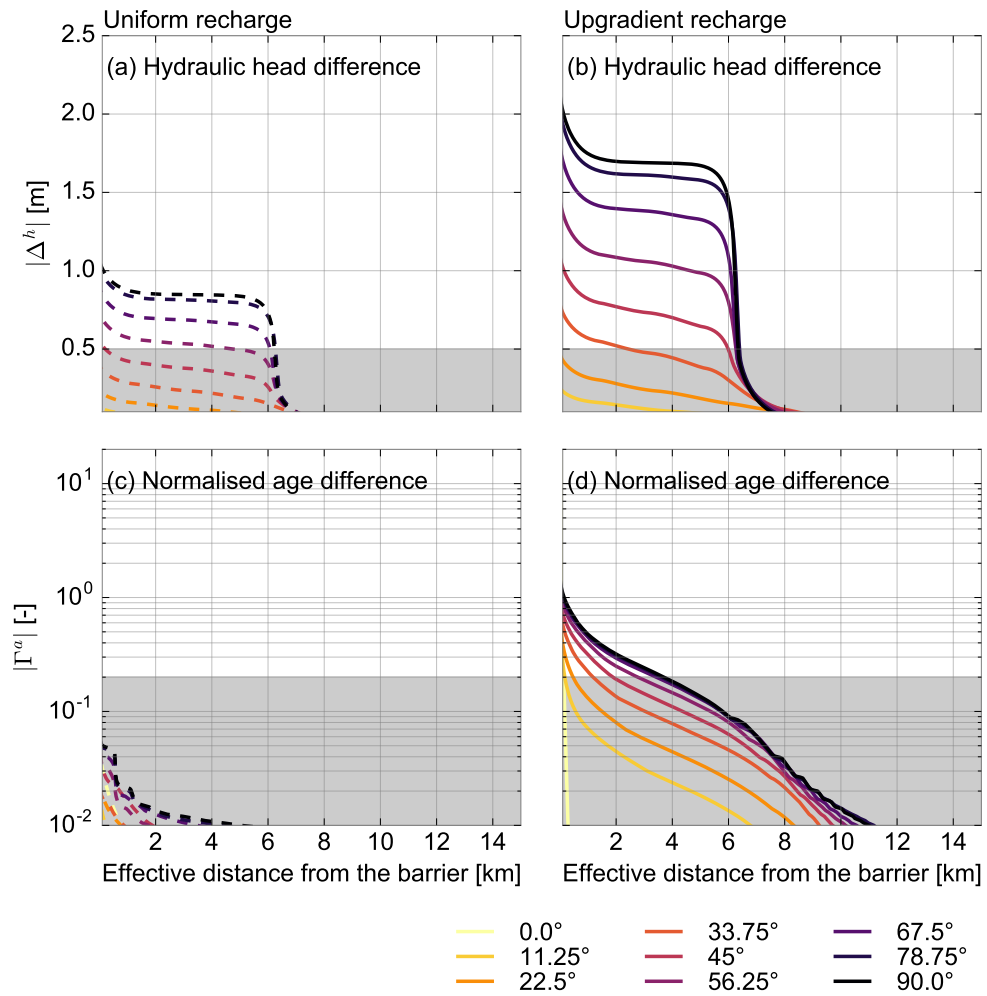


Figure 3.10: Cumulative plots displaying absolute values of (a, b) hydraulic head difference ($|\Delta^h|$), and (c, d) normalised groundwater age difference ($|\Gamma^a|$) compared to the “effective distance from the barrier” for the Fully-penetrating barrier with Uniform recharge (a, c, *dashed line*) and Upgradient recharge (b, d, *solid line*). The angle of 90° (*black line*) indicates that the barrier is orthogonal to the principal direction of flow and 0° (*light yellow*) indicates that it is parallel. The values shaded in grey represent those that would not be detectable with measurement errors of 0.5 m for $|\Delta^h|$ and 0.2 for $|\Gamma^a|$.

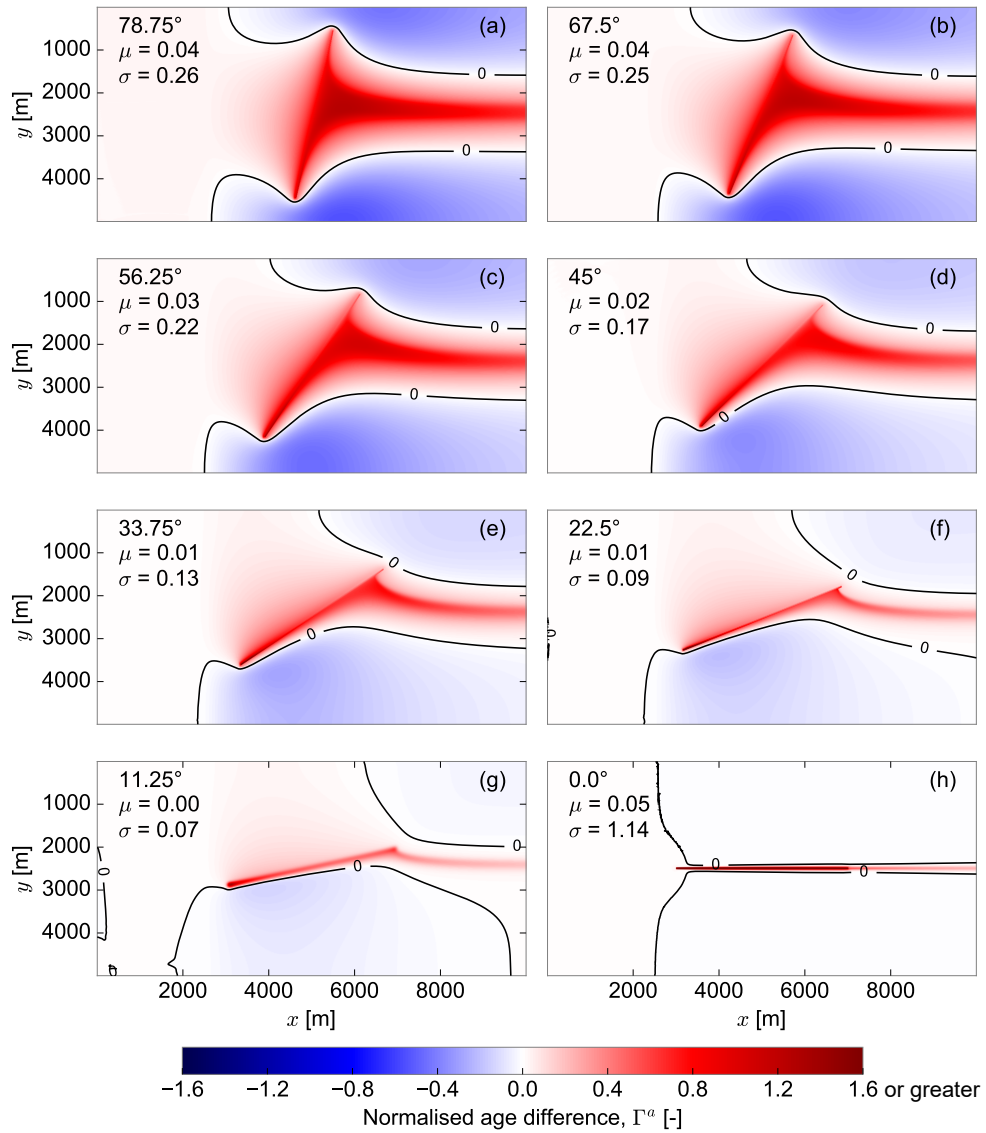


Figure 3.11: Plan view of normalised age difference, Γ^a , for various barrier orientations. Results are shown for the middle layer of an aquifer for a Fully-penetrating barrier with Upgradient recharge. Note that for plots (e) to (h) the colour scale was clipped to a maximum value of 1.6 so all values above this (within the barrier itself) are shown as a deep red.

When the ratios of $K_a : K_b$ is increased ($K_a = 1$ m/d) from 101 to 103, the impact on hydraulic head (Figure 3.12c) and groundwater age (Figure 3.12d) increases. However, beyond 103, the values of Δ^h and Γ^a only marginally increase, illustrating the ratio beyond which any further reduction in K_b , relative to K_a , has little to no influence on groundwater velocity. This represents the point at which groundwater flow through the barrier becomes negligible. Similarly, as the barrier width increases, it becomes more difficult for groundwater to flow across the barrier. Therefore, the maximum hydraulic head difference increases to approximately 4.0 (Figure 3.12e). The age difference due to the barrier also increases (Figure 3.12f). When the width of the barrier is greater than 500 m, values of $|\Gamma^a|$ greater than 10 are observed in some parts of the aquifer. The effective distance from the barrier having values of $|\Gamma^a| > 0.2$ is < 3 km with a width of 50 m, and > 5 km with a width of 1000 m.

3.5 Discussion

3.5.1 Barrier detection

The ability to detect hydrogeologic barriers has many implications for groundwater management. Due to their role in constricting and localising flow, barriers can facilitate spring or wetland formation (Babiker and Gudmundsson 2004; Gleeson and Novakowski 2009), influence drawdown associated with large-scale groundwater extraction (Bense and Van Balen 2004; Gumm et al. 2016; Marshall et al. 2019), or separate high-quality from low-quality water (Mayer et al. 2007). Hydraulic head data form the foundation of groundwater system characterisation and have proven to be useful for detecting hydrogeologic barriers. A sharp change in hydraulic head is observed across the Fully-penetrating barrier. Sharp hydraulic head changes across barriers have been observed in several field studies through regional potentiometric mapping (Bense and Van Balen 2004; Bense et al. 2003; Cilona et al. 2015; Ferrill et al. 2004; Stamatis and Voudouris 2003). The maximum difference in hydraulic head between cases with and without a barrier was only 2.6 m in this study. However, this is dependent on the model geometry, boundary conditions, and applied stresses. The length of the Fully-penetrating barrier was simulated as 4 km (across a 5 km wide aquifer), whereas in reality some tectonic structures can be tens or hundreds of kilometres long. Smerdon and Turnadge (2015) used numerical modelling to demonstrate that a difference in hydraulic head of up to 50 m could be attributed to the presence of hydrogeologic barriers. Some examples of the observed change in hydraulic head across barriers include: approximately 5–10 m in Iran (Rajabpour and Vaezihir 2016); approximately 20–60 m in Germany (Gumm et al. 2016); and over 80 m in California, USA (Mayer et al. 2007).

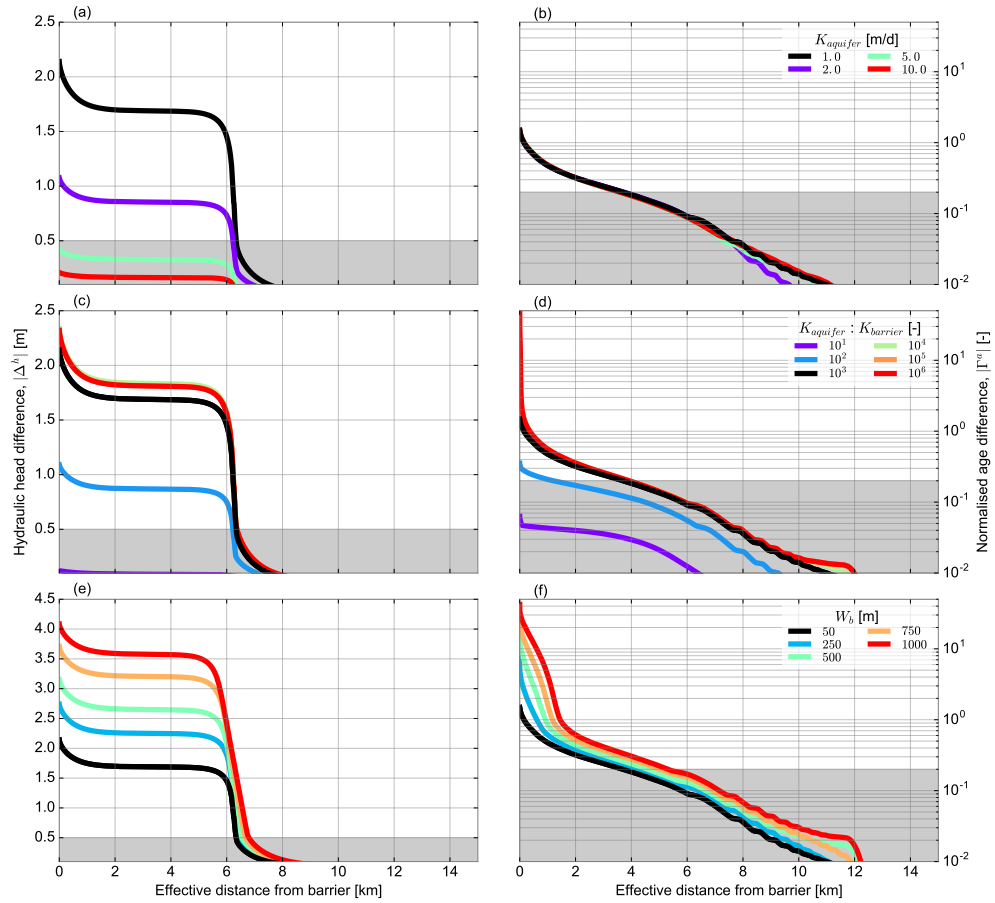


Figure 3.12: Sensitivity of hydraulic head difference and normalised age difference to aquifer and barrier properties for a Fully-penetrating barrier with Uniform recharge. Plots show the effect of changing (a and b) values of K_a (where the ratio of $K_a : K_b$ is held constant at 10^3); (c and d) the ratio of $K_a : K_b$ ($K_a = 1$ m/d); and (e and f) the barrier width (extent along the x axis) on the absolute hydraulic head difference, $|\Delta^h|$ and the absolute normalised age difference, $|\Gamma^a|$. Values used in this study are shown as black lines. The shaded grey region represents values that would not be detectable with a measurement error of 0.5 m for $|\Delta^h|$ and 0.2 for $|\Gamma^a|$.

High hydraulic gradients do not definitively signify that a barrier is present. They may be caused by changes in other aquifer properties; for example, aquifer thinning (Bense and Van Balen 2004). Datasets such as groundwater age, therefore, provide useful additional information. For a Fully-penetrating barrier with Upgradient recharge, groundwater age increases sharply across the barrier. However, for the same barrier type but with Uniform recharge, the barrier only marginally perturbs groundwater age. The difference in the results between these two recharge scenarios is related to the Baseline groundwater age distributions. With Upgradient recharge, groundwater age increases in the horizontal direction, which the Fully-penetrating barrier obstructs. Groundwater age does not considerably increase in the horizontal direction with Uniform recharge, so the impact from the barrier is dramatically less. Under both recharge scenarios, the difference in hydraulic head and groundwater age distributions can be partially explained by the fact that the barrier does not obstruct the same quantity of flow. The cross sectional areas of the Fully-penetrating barrier is 1.2 km^2 and of the Buried barrier is 0.75 km^2 . This is why a metric for the effective distance from the barrier was derived, to normalise the volume of the aquifer by the cross-sectional areas of the barrier and therefore allow a better comparison between the two case studies.

Type of barrier	Uniform recharge	Upgradient recharge
Fully-penetrating	H: Likely A: Unlikely	H: Likely A: Possible
Buried	H: Unlikely A: Possible	H: Unlikely A: Unlikely

Table 3.2: Summary of results where the detection of a barrier is “likely,” “possible,” or “unlikely” given the dataset used, where “H” is hydraulic head and “A” is groundwater age. These classifications are based on the results from the spatial impact of a barrier on hydraulic head and normalised groundwater age distributions (Figure 3.8). They are also based on the effective distances for which $|\Delta^h|$ and $|\Gamma^a|$ are detectable of $\geq 5 \text{ km}$ (“likely”), $2\text{--}5 \text{ km}$ (“possible”) and $< 2 \text{ km}$ (“unlikely”).

The results are summarised in order to answer, for each barrier configuration and recharge scenario: “would hydraulic head and/or groundwater age be useful in detecting the barrier?” (Figure 3.2). In reality this is a complex question. For any particular site, it will depend on the network and quality of monitoring data. Nevertheless, this type of summary provides a useful comparison of the utility of each dataset depending on the barrier type and recharge scenario. Firstly, an assumption made was that, as previously mentioned, a head difference of $\geq 0.5 \text{ m}$ and a normalised age difference of ≥ 0.2 is likely to be detectable in the field. However, this will depend on the natural variability in hydraulic head, the length of the flow path,

and the type of environmental tracer used, amongst other things. A second assumption was based on the results for the ‘Extent of spatial impact of a barrier,’ where the effective distance from the barrier was compared to $|\Delta^h|$ and $|\Gamma^a|$ (Figure 3.8). It was assumed that if the effective distance, where $|\Delta^h|$ and $|\Gamma^a|$ are detectable (i.e. > 0.5 m and 0.2, respectively), is ≥ 5 km, then it is likely the barrier would be detected in the field. Similarly, it was assumed that if the effective distance where $|\Delta^h|$ and $|\Gamma^a|$ are detectable is 2–5 km or < 2 km, then it is either possible or unlikely (respectively) that the barrier would be detectable in the field. While effective distance is not an exact metric for determining the area of an aquifer impacted from a barrier, it is, nevertheless, useful as a first step for understanding how data can be used to locate barrier features. The effective distances can also be loosely related to sampling densities, although the location of sampling along the barrier and the depths of the piezometers are important.

In addition to sampling densities, the locations of samples relative to any aquifer structures are relevant. In general, wells closely spaced across fault zones are uncommon (Bense et al. 2013), so well construction and placement is crucial. With the Fully-penetrating barrier, head changes would be most likely to be observed at the centre of the barrier—only small head gradients were observed within 500 m of the edge of the barrier. With the Buried barrier, the hydraulic head change across the barrier was only detected if measured at specific depths, such as with a nested piezometer. Open wells may have lower resolution if a large part of the well is at elevations higher than the barrier. Field measurements could also be compromised by other confounding sources of information, such as preferential flow paths or transient signals in recharge and pumping.

3.6 Assumptions and limitations

The analyses in this study rely on several assumptions. Firstly, simple constructions of barriers were analysed. The barriers simulated are of a constant thickness, linear, vertical, and their internal properties do not vary. Offset of stratigraphic layers or a changes in topography across the barriers were not considered. This study also does not consider discharge at the surface, and groundwater levels are consistently below the top of the aquifer (and land surface). In reality, geological structures are very complex. Faults may act as conduits or complex conduit-barrier systems and a low-permeability fault core can be surrounded by a higher-permeability “damage zone” (Allen and Michel 1999; Bense and Person 2006; Caine et al. 1996). Dykes may also be preferential pathways for groundwater flow (Wilkes et al. 2004). More research is required to understand how barriers with complex permeability structures and fault

offsets will affect groundwater ages in an aquifer system. Groundwater age was also simulated directly, rather than specific environmental tracers commonly used to estimate groundwater age. Previous authors have shown that when an aquifer is heterogeneous, the use of environmental tracers to determine groundwater age can be challenging (Larocque et al. 2009; McCallum et al. 2014a; Weissmann et al. 2002).

Although we examine the potential to detect barriers using head and age data, and consider the distance from the barrier over which these parameters are significantly modified, we do not specifically consider issues of sampling density. The ability to uniquely ascertain the location of a barrier will depend on the number, position and depth of observations. Inverse modelling is one extension to this study that could assist in better understanding the influence of observation data on aquifer characterisation. This method has been proven to successfully combine datasets to detect and characterise aquifer structures. For example, ground geophysics, hydraulic testing, and tidal fluctuations determined the properties of volcanic dykes (Comte et al. 2017); geophysical data and hydraulic testing identified the distribution of clay in an aquifer (Harp et al. 2008); and pump-test, regional water-level, and discharge data were used for conceptual model identification in a step-wise model inversion (Dai et al. 2010). Using stochastic approaches to characterise the impact of barriers on a certain model output is another area for potential future research. One example of a similar approach uses a global sensitivity analysis to understand the impact of uncertain aquifer fracture characteristics on seawater intrusion modelling (Koohbor et al. 2019). A similar approach could test the influence of unknown locations and properties of barriers on aquifer drawdown, groundwater discharge to surface water systems, or contaminant transport, for example, depending on the overarching management goal.

This study provides some insight into data collection approaches for an ‘ideal’ study investigating an aquifer with suspected low-permeability features. The exact approach taken to identify a barrier and determine its properties would depend on the location and purpose of the study. However, one suggestion based on the outcome of this study is that at sites where no previous data exist, samples for hydraulic head and groundwater age taken at regular spatial intervals could be evaluated. If other datasets, such as geophysics, are available, these may be interpreted to understand if any parts of the aquifer are more likely to contain low-permeability features. Simple interpolation methods for hydraulic head and groundwater age, such as based on kriging, could be evaluated for any zones of high contrast. Ideally, groundwater models could be made with and without barriers and compared to the samples. The outcome of the mapping and the modelling could help to refine zones where an

increased density of sampling would be helpful.

3.7 Conclusions

This study uses numerical simulations of flow and transport to simulate the effect of low-permeability, vertical, linear structures on hydraulic head and groundwater age distributions. It shows where these data are useful for the detection of hydrogeologic barriers under two contrasting recharge settings. The results contribute to further studies in aquifer structure detection, data inversion and monitoring network design. Two key barrier types were tested. The first penetrated the full aquifer thickness (Fully-penetrating barrier), and hydraulic head data were found to be useful for barrier detection, given the sharp hydraulic head gradients. However, for the second barrier type (Buried barrier), hydraulic head measurements would be unlikely to reveal the presence of the barrier.

Using groundwater age to detect a barrier's presence was found to be possible with two cases, a Fully-penetrating barrier under Upgradient recharge or with a Buried barrier under Uniform recharge. In the first case, a strong contrast in groundwater age occurs across the barrier and the difference in age between the case with and without a barrier is 1.6 times the age of the groundwater in parts of the system. In the second case, the Buried barrier's presence causes reduced groundwater velocities in the lower half of the aquifer resulting in older groundwater banking up on the upstream side of the barrier. The usefulness of groundwater age data was found, therefore, likely to depend on the availability of depth-specific sampling.

Barrier orientation is shown to be crucial for whether, and where in the aquifer, hydraulic head and groundwater age data could detect a barrier. For the Fully-penetrating barrier, only those with an angle $\geq 56.25^\circ$ to the principal flow direction with Uniform recharge, or $\geq 33.75^\circ$ with Upgradient recharge would be detectable using hydraulic head data. No barrier orientations had a measurable impact on groundwater age with Uniform recharge, but those oriented at an angle of at least 45° had an effective distance of impact on groundwater age from the barrier of ≥ 2 km. Sensitivity analyses shows that the ratio of the hydraulic conductivity of the aquifer to that of the barrier and the width of the barrier are very relevant in determining the potential for a barrier's identifiability.

Chapter 4

Hydrogeologic barriers in groundwater model inversions: the use of novel phantom structures

Citation for published article: Marshall, S. K., P. G. Cook, C. T. Simmons, L. F. Konikow, S. Dogramaci, Hydrogeologic Barriers in Groundwater Model Inversions: The Use of Novel Phantom Structures. *Submitted Manuscript*, September 2020.

4.1 Abstract

Hydrogeological barriers can significantly impact groundwater model predictions. They are, however, often excluded from, or misrepresented in, groundwater models due to incomplete knowledge of their geometric and physical properties. Few existing methods exist for including narrow, linear structures such as faults and dykes in model inversions. Here we show that sharp barriers can be included in groundwater model inversion, even where their presence is uncertain. We introduce a method utilising ‘phantom structures’—randomly located, linear groups of model cells assigned a unique hydraulic conductivity value—to improve identifiability of barriers. Automated parameter estimation using PEST is implemented to determine models structures that best match the hydraulic head and groundwater age observation data from a hypothetical aquifer. Our results show that with more than approximately one observation well per four square kilometres we are able to largely deduce the location and properties of a hydrogeologic barrier. We compare these results to model inversion using traditional pilot points. With pilot points, the model-to-measurement misfit is lower than with phantom structures for observation

well locations, but is higher for other cells across the remaining model grid. The phantom structures approach shows promise in identifying hydrogeological structures and in reproducing groundwater flow across a model. Our results demonstrate that the geometric properties of geological structures can remain flexible in a model inversion. This is a step towards reducing conceptual model uncertainty where the presence and properties of hydrogeologic barriers are undefined.

4.2 Introduction

Numerical model development to predict or describe groundwater flow and transport is based on a practitioner’s understanding of an aquifer system, known as its conceptualisation. Yet a large amount of uncertainty can exist in groundwater system understanding related to physical processes and the subsurface geological framework, amongst other things (Beven 2005; Enemark et al. 2019; Gupta et al. 2012; Singh 2001). Model inversion, such as history matching (or model calibration), is one procedure whereby expert knowledge and direct measurements can be combined to help estimate a groundwater system’s parameters. The most common parameter estimated in this manner is hydraulic conductivity, K . Many examples demonstrate the use of hydraulic head and groundwater age for the estimation of aquifer properties (Knowling et al. 2020; Konikow et al. 2008; Sanford 2011; Zell et al. 2018). Embedding knowledge about aquifer structures helps to ensure that an inversion is well-posed and therefore parameter values are uniquely estimable. When inverting with a pre-determined model conceptualisation, however, parameter estimates may appear optimal despite misrepresenting salient aquifer features (Carrera and Neuman 1986). This uncertainty in model structures can result in a ‘perfectly calibrated’ model that remains incorrect with respect to the prediction of interest (Moore and Doherty 2005).

Some methods exist for determining aquifer structures in model inversions where no prior knowledge of their geometric properties exist. The use of pilot points—assigning hydraulic properties to specific positions within the model domain rather than directly to the whole model grid, allows for flexibility in determining the location and shape of model parameters (Doherty 2003). However, this method requires a form of spatial averaging, often resulting in a smoothed parameter field, which may not be suitable where sharp changes in hydraulic properties are known to exist. Another method to estimate structural parameters establishes the proportions, geometry, and pattern of aquifer facies (such as horizontal clay lenses) and allows for flexibility in the positioning of facies boundaries (Harp et al. 2008). The use of training images has also shown to be successful in understanding changes between

high and low permeability units that result from a braided fluvial setting or changes in aquifer facies, for example (Chen and Rubin 2003; McCallum et al. 2014b). In these examples, many conditioning points, or considerable knowledge of existing aquifer properties, are required at the outset to interpolate other aquifer structures. However, there may be just one (or a few) relatively narrow low permeability barriers in an otherwise higher-permeability aquifer. These are likely to be more difficult to detect and may not have been intersected at all by direct measurements.

Faults (Bense and Van Balen 2004; Caine et al. 1996) and dykes (Babiker and Gudmundsson 2004; Comte et al. 2017; Wilkes et al. 2004) are examples of where sharp changes in K can occur between a higher-permeability host rock and lower-permeability barriers. They can form important controls on groundwater flow (Bense et al. 2003; Cilona et al. 2015; Ferrill et al. 2004), chemistry (Gumm et al. 2016; Sebben and Werner 2016), age (Castro and Goblet 2005; Janos et al. 2018; Marshall et al. 2020), discharge processes (Babiker and Gudmundsson 2004; Bense and Kooi 2004; Gleeson and Novakowski 2009), and drawdown (Hadley et al. 2020; Marshall et al. 2019). Locating and characterising hydrogeologic barriers, however, can be difficult and costly. Wells intersecting or surrounding geologic structures such as faults are uncommon (Bense et al. 2013). Even where direct and indirect measurements of K at or adjacent to barriers exist, challenges exist in scaling these measurements to a regional area.

Model inversion studies have been used to estimate the properties of hydrogeologic barriers. For example, the hydraulic conductivity, effective porosity and storativity of volcanic dykes were estimated in Northern Ireland using manual trial-and-error parameter estimation (Comte et al. 2017). Hadley et al. (2020) compared simulated hydraulic head drawdown data to observed values from a large-scale aquifer test to refine estimates of K of the Sandwich Fault Zone in Illinois. Simulated and observed pumping test data were also used to estimate the K values of three regional faults and a volcanic intrusive unit in Valley of Queretaro, Mexico (Ochoa-González et al. 2015). Similarly, the hydraulic conductivity of the Mission Creek fault in California was estimated by Mayer et al. (2007) by comparing simulated groundwater elevation data with field observations collected over six decades. Regional hydraulic head distributions were also used by Marler and Ge (2003) to characterise the Elkhorn Fault in Colorado. In all of these examples, however, the locations and geometric properties of structures (such as width, strike and dip) were known and fixed.

In this study, our objective is to include hydrogeologic barriers in a model where their presence is suspected but unknown. A new method is proposed that allows for the inclusion of thin impermeable structures, which may include faults and dykes, in a model inversion, without knowing their location or properties in advance.

The method utilises novel ‘phantom structures’—randomly located, linear groups of model cells that are assigned unique representative properties during model inversion. The term phantom structures has not, to the authors’ knowledge, been used in the hydrogeological literature. Instead, the term was created to illustrate that the structures can be seen but do not really exist. The use of the term phantom has been used in other statistical disciplines, for example in medical imaging or cosmology. However, this study was not based on these and the meaning is unrelated. In this study, the phantom structures have different locations, geometric properties, and physical properties (in this case K). Automated parameter estimation is used to determine the smallest number of these structures that produce the best match to the hydraulic head and groundwater age observation data. Our method aims to avoid conceptual model ‘surprise’ and unforeseen consequences of incorrect model structures in the implementation of numerical models (Bredehoeft 2005). This study utilises tools and techniques already widely available in the groundwater industry and is intended as a prototype upon which further studies utilising field examples can be based.

4.3 Materials and methods

4.3.1 Hypothetical model

The study is designed to evaluate the use of advanced groundwater modelling and parameter estimation methods to help identify heterogeneous linear features in an aquifer. We create a hypothetical aquifer system containing an embedded linear low-permeability feature, which provides a ‘ground-truth’ or control basis. We then assume it is unknown and use numerical methods to try to identify and characterise the feature given varying assumptions about the availability of known head and age data. Here we attempt to emulate the challenges faced in a real system with some, but limited, data available.

We initially set up a model with a known location of a hydrogeologic barrier, herein referred to as the *real* model. This is a simple model that includes only two zones of differing hydraulic conductivity. The hydraulic conductivity of the aquifer, K_a , is homogeneous, except for a single barrier with a value of hydraulic conductivity, K_b , three orders of magnitude lower than K_a . A simple model set up ensures that we can test and demonstrate the feasibility of this approach without other complicating factors, such as additional heterogeneity. It also ensures rapid model processing times that are preferred for undertaking multiple model inversions.

Groundwater flow was simulated using MODFLOW-NWT (Niswonger et al. 2011).

The groundwater flow equation was solved with the Newton solver using a head change and residual convergence criterion of $1e-6$ m. Groundwater age was calculated using MT3D-USGS (Bedekar et al. 2016) with direct age simulation (Goode 1996). Age was simulated as a nonreactive solute species where water age increases by one unit of time per unit time. This approach allows age mixing (dispersion) by applying the advection-dispersion transport equation, which is not the case with purely advective approaches. A value of longitudinal dispersivity of 1.5 m, representing transport over approximately 100s of metres (Gelhar et al. 1992), was adopted. This, as well as other flow and transport parameters (Table 1) were held constant. However, actual parameter values are not highly relevant as the purpose is to demonstrate a new approach for model inversion. A standard finite-difference method was used to solve the transport equation, with a convergence criterion of $1e-5$ in terms of relative concentration.

Parameter	Symbol	Value
<i>MODFLOW-NWT</i>		
Grid size (x and y directions) [m]	$\Delta x, \Delta y$	100
Layer thickness [m]	Δz	300
Specific yield	S_y	0.1
Recharge rate [m/d]	R	$1.37e-5$
Hydraulic conductivity - aquifer [m/d]	K_a	1
Hydraulic conductivity - barrier [m/d]	K_b	$1e-3$
<i>MT3D-USGS</i>		
Effective porosity	η_e	0.1
Zeroth order reaction rate [yrs/d]		$1/365.25$
Longitudinal dispersivity [m]	α_L	1.5
Transverse dispersivity [m]	α_T	0.15
Effective molecular diffusion coefficient, water [m ² /d]	D^*	$9e-6$

Table 4.1: Model dimensions and universal parameters for the real model.

Dimensions of the real model are 20 km by 10 km with a cell size of 100 m x 100 m. It is a one layer model and grid size was held constant between the forward and inverse models. A 2D rather than a 3D model was used for simplicity and efficiency given that faults and dykes are largely vertically inclined. The left and right model sides both have general head boundaries, and a regional head difference of 100 m across the domain was imposed (an overall hydraulic gradient of 0.005 m per metre). The two lateral sides and base of the model are no-flow boundaries and the upper surface is simulated as a free water-table boundary. Recharge is applied uniformly across the aquifer at a rate of $1.367e-5$ m/d (5 mm/yr). This synthetic example was devised to represent plausible real-world examples in arid climate regions and at the same time allow for rigorous examination of the robustness of this inversion technique with respect to the known aquifer structure. It is subjectively based on

what is conceptually known about aquifer systems in the arid Pilbara region of Western Australia, as this work forms part of a larger project assessing groundwater resources in this region (Cook et al. 2016; Underwood et al. 2018). It is not, however, intended to directly model this system and is purely hypothetical with no calibration to field data undertaken.

The hydraulic conductivity of the aquifer, K_a , is 1 m/d in all cells except those at the location of the barrier. Barrier cells have a hydraulic conductivity of $1e-3$ m/d and are located in the central part of the aquifer (Figure 4.1). The barrier location was randomly chosen and its length and width is again based on what is known of barrier characteristics in the Pilbara field region. The length of the barrier is 5,515 m and it is one cell width wide (100 m). The models were set up and post-processed using the FloPy package for Python (Bakker et al. 2016). Both the flow and transport models were executed as steady-state simulations.

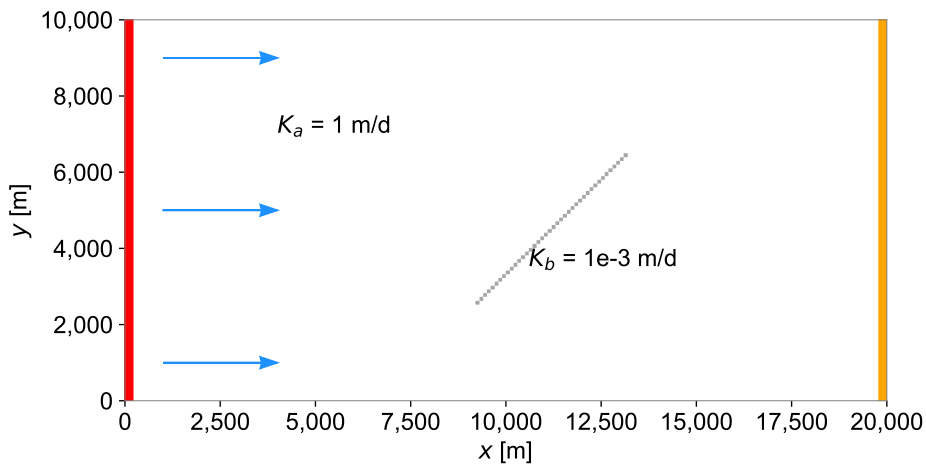


Figure 4.1: Schematic, 2D plan-view representation of the simulation domain showing the dimensions of the model and boundary conditions. The *slanted grey line* shows the location of the low permeability barrier. The *red and orange lines* show general head boundaries. Top and bottom boundaries are no-flow. The *blue arrows* show the principal direction of groundwater flow. Recharge is added uniformly to the surface of the model.

4.3.2 Phantom structures

Phantom structures are introduced in this study as groups of model cells assigned a single fitting parameter (per group) in the inversion, in this case barrier hydraulic

conductivity (K_b). Their name stems from the fact that they are a representation of something abstract or ideal in that they can be ‘seen’ in the inversion, when they are in fact not (necessarily) real. In a sense, including phantom structures is similar to using model zones or pilot points (i.e. using ‘pilot lines’), in that phantom structures are included to simplify the parameter field to define a well-posed problem. They are different from model zones because more phantom structures than are actually thought to occur are included, with the focus being on narrow, linear structures generally not well-represented in model inversion. Unlike pilot points, phantom structures are not intended to be the basis for spatial interpolation but similar to pilot points, phantom structures or ‘pilot lines’ are a spatial parameterisation device to help guide the solution towards convergence.

One hundred phantom structures were included in each inversion. The location, orientation and length of each structure were randomly assigned using the random package in python. Phantom structures are conceptualised as groups of grid cells. Prior limits were placed on the characteristics for each phantom structure. They had to occur on the grid with a length between 100 and 10,000 m. Orientation was assigned randomly between 0 and 180°. Tests were conducted for including fewer or more phantom structures. Ideally, as many as possible would be included—this increases the possibility that one phantom structure would occur in the same position as the real structure. Three configurations of phantom structures, herein referred to as Phantom Structures 1, 2 and 3 (PS1, PS2 and PS3) were tested for each observation well configuration (Figure 4.2) to improve the likelihood that a phantom structure with similar geometric properties as the real structure occurs.

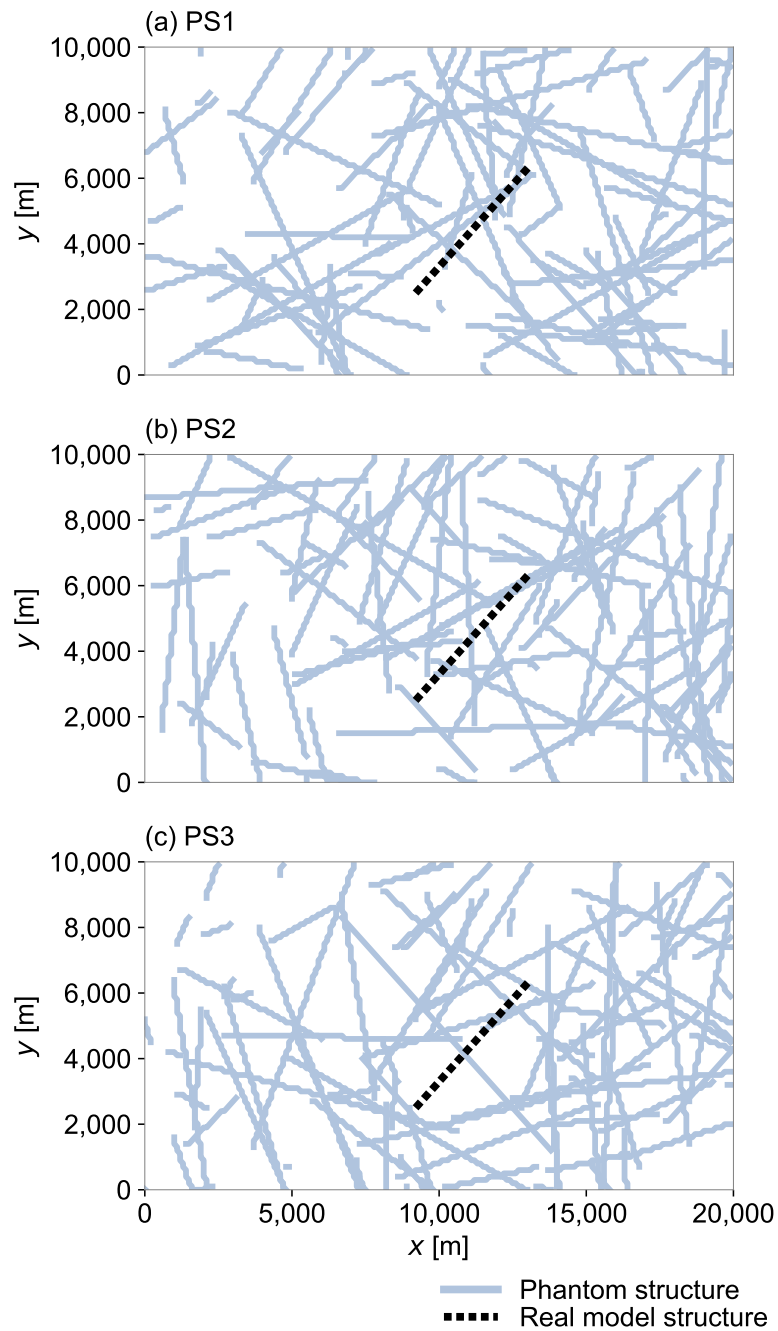


Figure 4.2: Locations of phantom structures represented by *solid blue-grey lines* for each phantom structure configuration, (a) PS1, (b) PS2, and (c) PS3. The real structure is shown as a *dashed black line*.

4.3.3 Hydraulic head and groundwater age data

Results of running the model with parameters listed in Table 4.1 show that hydraulic heads gradually decrease in the direction of groundwater flow except across the barrier, where it sharply declines (Figure 4.3a). Groundwater age increases gradually in the direction of groundwater flow except downstream of the barrier, where a trail

of older groundwater extends from the barrier towards the downstream end of the aquifer (Figure 4.3b). The mean groundwater age in the model domain is 623 yrs. The age downstream of the barrier reaches a maximum of 1290 yrs.

Randomly selected points (cells) across the model grid are designated as observation wells, and calculated hydraulic head and groundwater age data at these locations in the real model are used as observation data to estimate hydraulic conductivity values in all inversions. Observation wells were randomly sampled within the grid, excluding cells where phantom structures are present, using the random package in python. No measurement error was added to the model-produced ‘observation data’. Inversions were completed with 500, 250, 100, 50, 25, 10, or 5 observation wells. For each observation well density, three different configurations of observation wells (OW1, OW2 and OW3) were tested to ensure that the number, or density, of wells was tested, rather than the specific placement of particular wells (Figure 4.4). For each well configuration, initially the largest number of wells (500) was randomly allocated and each lower well density is a subset of that original well distribution.

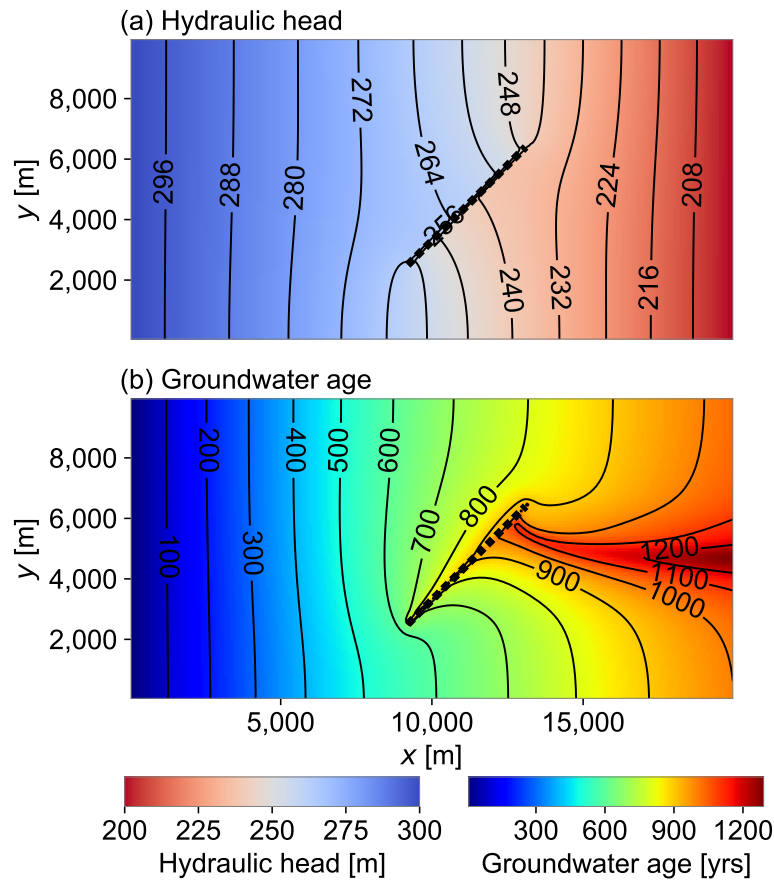


Figure 4.3: Model-calculated real system (a) hydraulic head, and (b) groundwater age distributions; hydraulic barrier denoted by *dashed black line*.

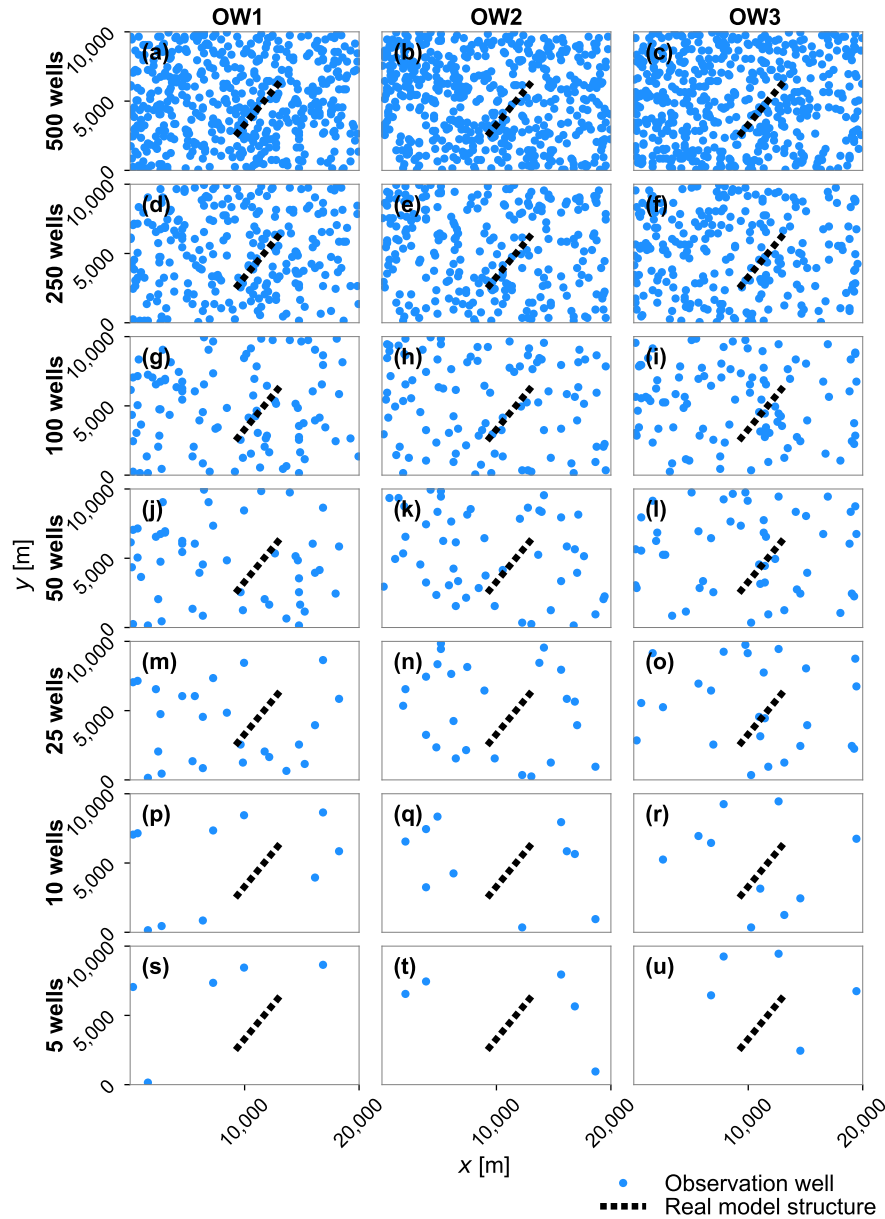


Figure 4.4: Observation well locations, shows by the *blue markers*, for the three different observation well configurations, OW1, OW2 and OW3, represented each by a column. Each row represents a different observation well density, (a – c) 500 wells, (d – f) 250 wells, (g – i) 100 wells, (j – l) 50 wells, (m – o) 25 wells, (p – r) 10 wells, and (s – u) 5 wells. The real structure is shown as a *dashed black line*.

4.3.4 Model inversions

We used 100 phantom structure parameters (K_b) and one parameter for the remaining aquifer (K_a). The model was calibrated to the hydraulic head and groundwater age observation data using the model-independent parameter estimation code PEST (Doherty 2018b) and executed using pyEMU (White et al. 2016). Within PEST,

the Gauss-Levenberg-Marquardt algorithm is used to iteratively minimise a measurement objective function ϕ_m , calculated from the weighted sum of squares of the residuals between observed (measured) and modelled data:

$$\phi_m = \sum_{i=1}^{NP} w_{hi}(\hat{h}_i - h_i)^2 + \sum_{i=1}^{NP} w_{ai}(\hat{a}_i - a_i)^2 \quad (4.1)$$

where h and a are observed values (hydraulic head and groundwater age, respectively), \hat{h} and \hat{a} are the equivalent modelled values, NP is the number of parameters, and w_h and w_a are the weights applied to the hydraulic head and groundwater age measurements, respectively. The objective is to minimise ϕ_m to achieve an acceptable level of model-to-measurement fit.

Hydraulic head and groundwater age data were simultaneously included in a single measurement objective function. Weights of $w_h = 25$ and $w_a = 1$ were used so that the two datasets had approximately the same contribution to the total objective function (Doherty and Hunt 2009). The limits for the posterior values of hydraulic conductivity were set between 1e-10 m/d and 1 m/d. That is, the structures were only permitted to form barriers to groundwater flow and not to be conduits.

For each inversion, PEST was run in regularisation mode. This means that a total objective function, ϕ_t , was minimised. This includes a term for the regularisation objective function, ϕ_r , as well as for ϕ_m :

$$\phi_t = \phi_m + \mu^2 \phi_r, \quad (4.2)$$

where μ is a regularisation weighting factor determined by PEST in the inversion. The purpose of regularisation is to achieve a unique suite of parameters where there are a large number of unknowns (Doherty 2015; Hill and Tiedeman 2007). In this study, Tikhonov regularisation was employed, which allows for prior information (i.e. expert knowledge) to be included as a constraint to the inversion. To achieve this, a regularisation objective function that penalises any difference between K_a and K_b was applied to every cell that constitutes a phantom structure:

$$\phi_r = \sum_{i=1}^n w_{ri} e^{K_a - K_{bi}}, \quad (4.3)$$

where n is the number of phantom structures and w_r is the regularisation weight used, where $w_r = 1$. We used an equation for ϕ_r that exerts a preference for parsimony. That is, phantom structures only ‘appear’, or only have $K_b \neq K_a$, if they

provide a large enough reduction in ϕ_m to offset the increase in ϕ_r .

For each configuration of phantom structures and each well configuration tested, two model inversions were run. In the first, the target measurement objective function, ϕ_m^t , was set extremely low at 1e-10, meaning that the inversion results could be considered as overfitted with little or no regularisation employed. The resulting value of ϕ_m from this inversion was then multiplied by 1.1 and used as the value of ϕ_m^t with exactly the same model set-up. Then the minimisation of ϕ_r is constrained by ϕ_m not exceeding ϕ_m^t . This is a compromise between reducing observation well data residuals while also accommodating regularisation. It was based on a similar approach used by Fienen et al. (2009). Only those for the second inversion including Tikhonov regularisation are shown in these results.

We compared the results from the phantom faults approach to one using pilot points. In the pilot point approach, the values of hydraulic conductivity estimated through the model inversion are assigned to 170 discrete points across the model domain. These values are used as the basis of a kriging algorithm used to assign hydraulic conductivity values to the remaining model cells. In this case, ϕ_r was used to minimise the (linear) difference between values of K assigned to pilot points and a prior K value of 1 m/d.

4.3.5 Sensitivity analysis

Composite sensitivity for each head and age observation was calculated for each inversion by PEST. Composite sensitivity is a measure of the sensitivity of an observation to all parameters involved in the parameter estimation process (Doherty 2015). This highlights observations that are sensitive to many parameters. One limitation is that it does not distinguish if there is another (or several other) observations, for example in the same area, that also have high composite sensitivities. Recording and comparing sensitivity data for observation data is useful because it provides insight into the locations of observation wells that are most useful in estimating a hydraulic conductivity field with a barrier present.

4.3.6 Metrics for evaluating inversion results

Assessing fit when real model is unknown

As there are many model inversions with multiple phantom structure configurations and observation well locations, it is useful to have methods for comparing the results from each inversion. The first step was to analyse the model-to-measurement misfit. We use a simple measure of root mean square error (RMSE) calculated for

the hydraulic head and groundwater age data, which is larger where the misfit is greater:

$$RMSE_h = \left[\frac{1}{NO} \sum_{i=1}^{NO} (\hat{h} - h)_i^2 \right]^{0.5}, \quad (4.4a)$$

$$RMSE_a = \left[\frac{1}{NO} \sum_{i=1}^{NO} (\hat{a} - a)_i^2 \right]^{0.5}, \quad (4.4b)$$

where NO is the number of observation wells, \hat{h} and \hat{a} are the posterior values of hydraulic head and direct age determined in the inversion and h and a are the values of hydraulic head and direct age extracted from the real model (representing ‘measured’ observations). A combined error term, $RMSE_c$ was also determined:

$$RMSE_c = \sum_{i=1}^{NO} w_h RMSE_{hi} + w_a RMSE_{ai}, \quad (4.5)$$

using the same values of w_h and w_a of 25 and 1 (respectively) as used in the model inversions.

Key phantom structures

We want to know if all one hundred phantom structures are required to best represent the model, or if there is a subset of one or more that are the most significant given the observation data. The first step was to distinguish phantom structures with $K_b < 0.99K_a$, in order that only structures that are notably different from the aquifer are assessed. Phantom structures with $K_b \approx K_a$ effectively disappear from the model and therefore are discarded as not useful to the results. The second step was to see which phantom structures had a high value of identifiability.

Identifiability is a measure to assess which of the parameters (i.e. which phantom structures) can be uniquely estimated based on the observation data (Doherty and Hunt 2009). It is based on the sensitivity statistics of each model output with respect to all adjustable parameters. Identifiability values for each phantom structure were calculated with a solution space cut-off of ten singular values using the IDENPAR executable provided with the PEST software suite (Doherty 2018b). The value of identifiability for a given parameter lies between zero (complete non-identifiability based on the observation data) and one (complete identifiability based on the observation data). An arbitrary value of 0.8 was used as a cut-off to determine which phantom structures are identifiable. Any phantom structure with an identifiability

below this value was discarded. The phantom structures that then remained after removing those with $K_b \approx K_a$ or with identifiability < 0.8 are denoted key structures in the inversion results and were ranked from high to low identifiability.

To isolate the smallest number of phantom structures that are most useful for representing our real model, we calculated how the value of $RMSE$ changed with different combinations of the key structures. First, $RMSE_h$, $RMSE_a$ and $RMSE_c$ were calculated for a model with no structures (completely homogeneous), then they were calculated for a model with the first ranked structure (that with the highest identifiability) only, then for a model with the first ranked structure and the second ranked structure, then for the first three ranked structures and so forth until all of the key structures had been evaluated. This shows how many of the structures are required to achieve a considerable drop in $RMSE$.

Assessing fit when real model is known

Because we do know the real model in this analysis, we made a final assessment of inversion results based on comparing the real model's head and age distribution with each inversion's posterior head and age distribution. To do this, both hydraulic head and groundwater age distributions from the model results were filtered to avoid observation wells, phantom structures and model boundaries. This was done to select only cells not active in the model inversion, or which could be subject to boundary effects, and is referred to as the filtered model (or the filtered cells). For all filtered cells, the modelled hydraulic head and groundwater age values were compared to those from the real model. Again, $RMSE_h$, $RMSE_a$ and $RMSE_c$ were calculated as per Equations 4a, 4b and 5 but with a value of NO equivalent to the number of filtered cells.

A methodological chart describing the approach in this study is shown in Figure 4.5.

INPUTS	PROCESSES	OUTPUTS
<i>Setting up model</i>		
Real K array Prior distributions for barrier location, orientation and length of barrier	1. Run real model 2. Set up phantom structures 3. Set up observation well locations	Real hydraulic head and groundwater age distributions PS1, PS2 and PS3 Observation well locations
<i>Sampling real model to extract observation well data</i>		
PS1, PS2 and PS3 Observation well locations	4. Sample real hydraulic head and groundwater age data at observation well locations	"Measured" hydraulic head data "Measured" groundwater age data
<i>Model inversions</i>		
"Measured" hydraulic head and groundwater age data	5. Run PEST	Jacobian matrix Sensitivity data Posterior values of K for aquifer and barriers
<i>Post processing</i>		
Jacobian matrix Posterior values of K for aquifer and barriers	6. Calculate identifiability for phantom faults 7. Determine key phantom faults	Identifiability for each phantom structure Key phantom structures

Figure 4.5: Workflow metric to describe the process for model inversion using phantom structures.

4.4 Results

The results are first presented for those of a single model to illustrate the process. We then show results for all observation well and phantom structure configurations. For the single inversion, results are shown for a case with PS1 (Figure 4.2a) and OW1 with 500 observation wells (Figure 4.4a).

4.4.1 Single inversion

After calibration of the dataset of 500 hydraulic head and 500 groundwater age observations with 100 phantom structures, the key phantom structures were determined using the approach outlined in the Materials and Methods section above. The hydraulic conductivity of the four identified key structures, when compared to the real model (Figure 4.6) show that key phantom structures are located in the vicinity of the real barrier and display a substantially reduced K_b . Those structures that are approximately the same orientation as the real structure (Structure 1 and 3) have K_b values of $1.1\text{e-}2$ and $4.7\text{e-}2$ m/d, which is one order of magnitude higher than the real structure, which has a K_b of $1\text{e-}3$ m/d (Table 2). Structure 2 is the closest in distance to the real structure and has a K_b value of $5.3\text{e-}3$ m/d. Structure 4 has the K_b of $7.1\text{e-}2$ m/d, closest to that of the aquifer (1 m/d), possibly because it is furthest in distance from the real structure. The posterior value for K_a was 0.99 m/d, within 1 % of the real K_a of 1 m/d. The identifiabilities of the key structures that are closer to the location of the real structure and more similar in orientation have the higher values of identifiability. Structures 1, 2 and 3 all have identifiability values of 1.00. Structure 4 has a marginally lower value of identifiability of 0.998.

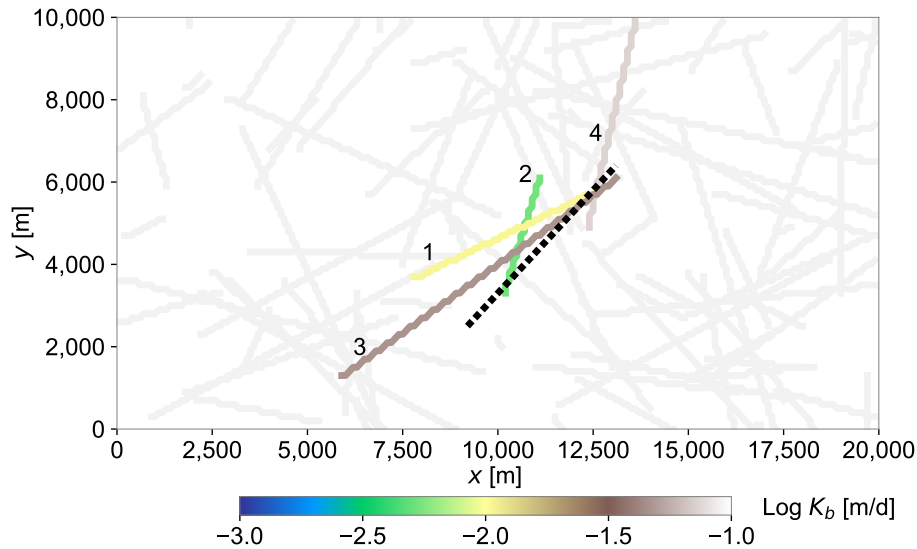


Figure 4.6: Results for a single inversion showing the posterior value of $\log K_b$ for each key phantom structure. Phantom structures not deemed as key are shown as *light grey lines*.

The difference in hydraulic head and groundwater age distributions for a model with these phantom structures and those for the real model show that over the entire model domain, the maximum difference in hydraulic head is -16 m (Figure 4.7a). Overall, the area of greatest hydraulic head difference is confined to a narrow zone

Phantom structure	K_b [m/d]	Identifiability	Distance from real [m]	Orientation [°]	Length [m]
1	1.1e-2	1.00	1020	66	5239
2	5.3e-3	1.00	632	18	2941
3	4.6e-2	1.00	1879	56	8653
4	7.1e-2	0.998	3413	13	5142

Table 4.2: Parameter values for key phantom structures in the single inversion with 500 wells and PS1. The real barrier parameters: $K_b = 1\text{e-}3$ m/d; orientation = 45° ; and length = 5515 m. Note that the order of phantom structures is based on identifiability values, which are shown to three significant figures.

adjacent to the location of the real barrier. The remainder of the model has been relatively well reproduced with negligible error. The maximum difference in groundwater age is 300 yrs (Figure 4.7b). Once again, the differences are limited to small areas near the real barrier. For the remainder of the model domain the groundwater age distribution has been reproduced well, including the trail of older groundwater extending downstream of the real barrier. As the groundwater age in the vicinity of the real barrier is on the order of 700–1000 yrs, a difference of 300 yrs (43–30 %) is significant, though highly localised.

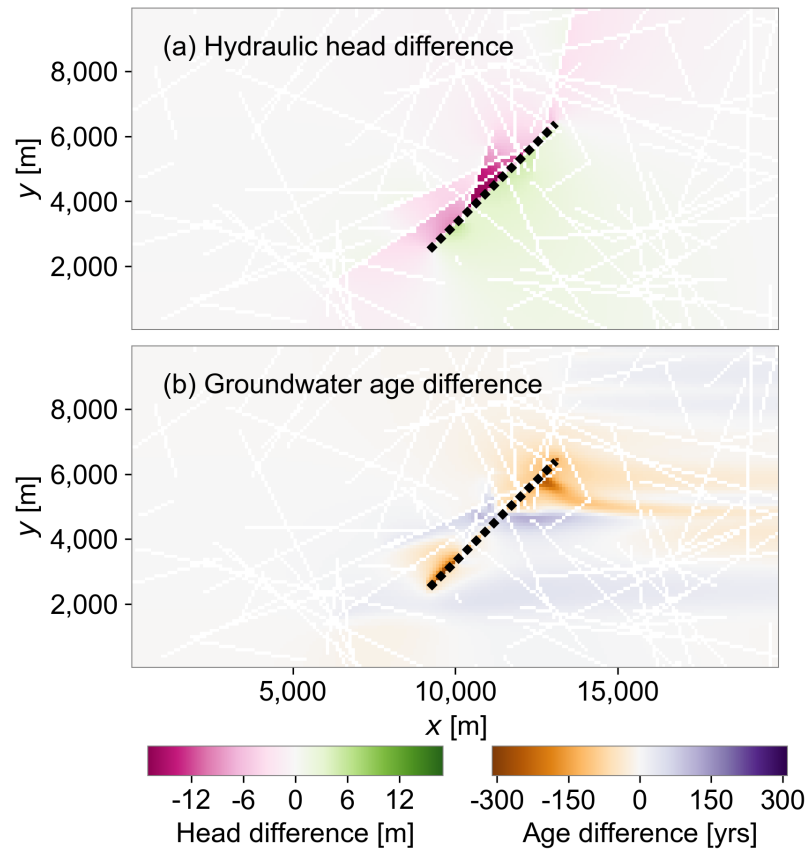


Figure 4.7: Difference between real model and the posterior parameterisation in single example for (a) hydraulic head, and (b) groundwater age. The difference represents posterior single example results minus known (real model) values.

The values of $RMSE_h$, $RMSE_a$ and $RMSE_c$ all follow a similar pattern of decline with each key phantom structure added subsequently in order of identifiability (Figure 4.8). Initially, without any structures in the system, $RMSE_h$, $RMSE_a$ and $RMSE_c$ are equal to 3.0, 85.1, and 161.3, respectively. These values drop considerably (by 0.7, 50.1 and 68.6 respectively) with the additions of Structures 1 and 2. These drops show that inclusion of Structures 1 and 2 in the inversion, with high values of identifiability, at close distances to the real structure, yield a good fit with the observation data. The addition of both the third and fourth structures results in additional drops in $RMSE_h$, $RMSE_a$ and $RMSE_c$ of 0.2, 6.6, and 12.1 respectively. After structures 1, 2, 3, and 4, no considerable further decrease in $RMSE_h$, $RMSE_a$ and $RMSE_c$ occurs with the addition of the other 94 phantom structures that were not key.

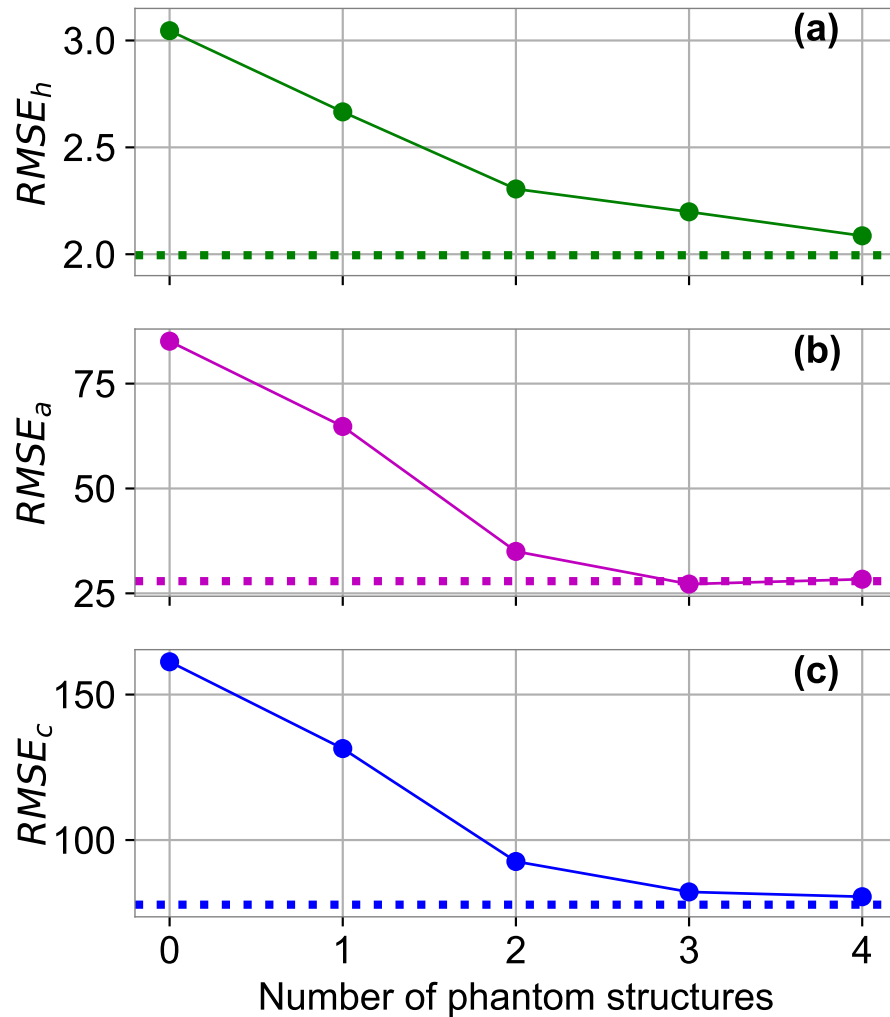


Figure 4.8: The $RMSE$ values for the single example with each key phantom structure, added cumulatively in order of identifiability for (a) hydraulic head, (b) groundwater age, and (c) hydraulic head and groundwater age combined. The dotted lines show the $RMSE$ value with all 100 phantom structures.

Evaluating sensitivity of the observation well data shows the sampling locations that are most useful for defining K_b values of the phantom structures. Sensitivity data for hydraulic head is highest for observation wells located close to (within approximately 2 km) the real structure predominantly on the upstream side (Figure 4.9a). The sensitivity of groundwater age observation illustrates that data collected both close to the barriers and within the trail of old water extending downstream of the real structure have higher sensitivities than elsewhere in the model (Figure 4.9b).

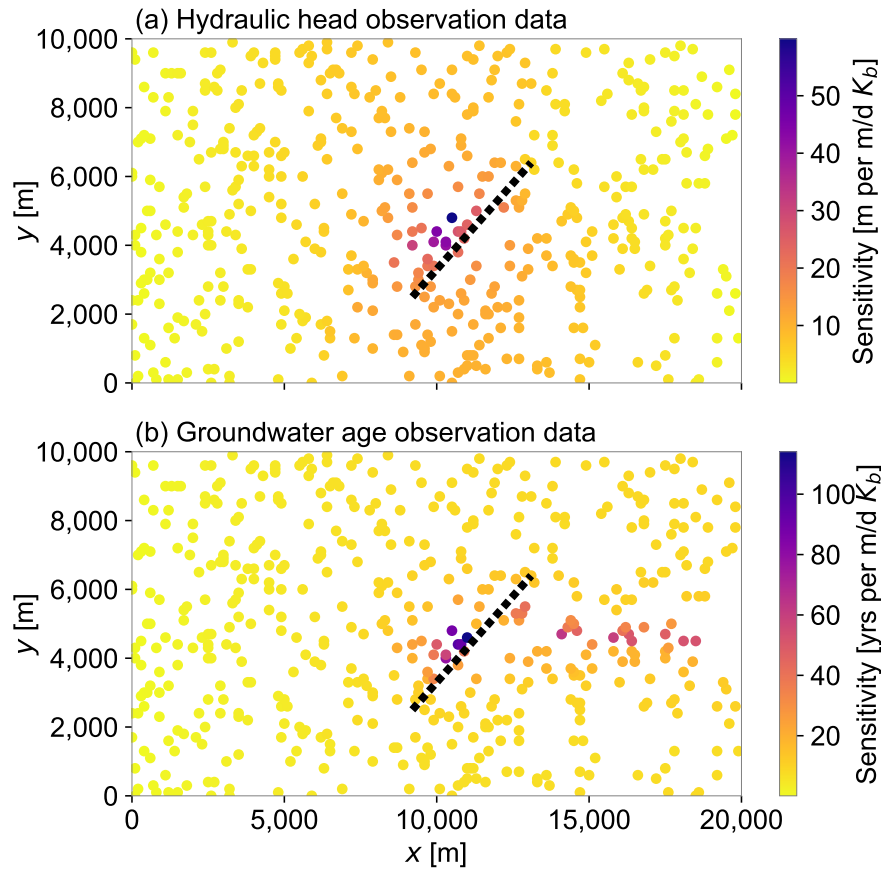


Figure 4.9: Composite sensitivity of observation well data for (a) hydraulic head, and (b) groundwater age for the single example.

4.4.2 All simulations

Key phantom structures

As the observation well density and phantom structure configuration vary, so does the posterior value of K_b for each phantom structure. For each observation well configuration, the K_b results with the same number of wells were averaged, and show (Figure 4.10) that as the number of wells increases, the key phantom structures are more centrally located around the site of the real structure. This can be particularly seen for PS1 where, as the number of wells increases to 100 or more, all phantom structures are located within a short distance of the real structure (Figure 4.10a, d and g). This trend is similar but not as pronounced with PS2 and PS3. This is likely because the randomly allocated phantom structures were not as good of a fit as for PS1; there were not as many phantom structures with a location similar to the real structure. The K_b of the key structures are mostly between 0 and $1e-3$ m/d.

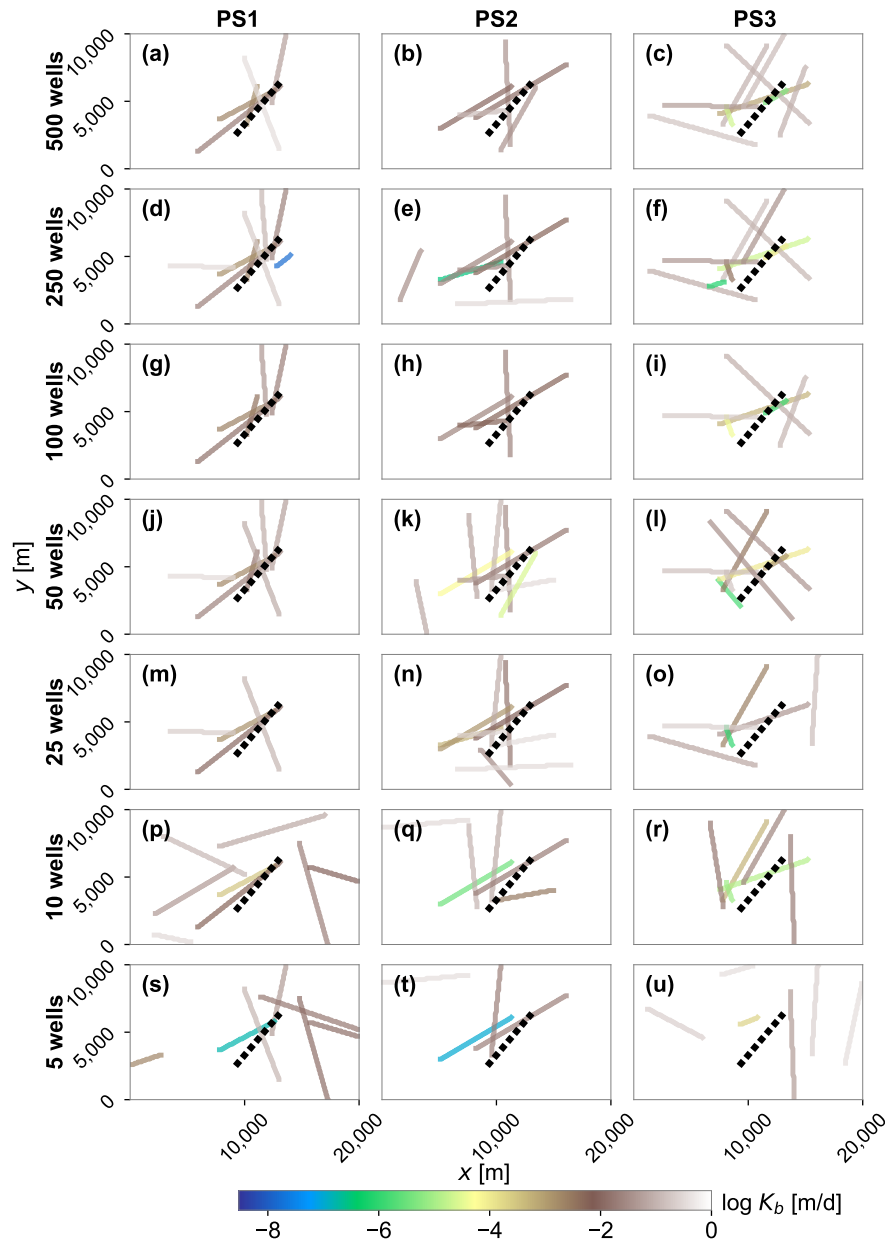


Figure 4.10: The mean values of K_b for each key phantom structure, where columns represent different phantom structure configurations, and rows represent different observation well densities. The mean is taken for each well configuration with the same number of observation wells. Only the key structures are shown.

Assessing fit when real model is unknown

As with the single inversion example (Figure 4.6), we can assess how many of the key structures contribute to the fit of modelled-to-measured misfit at the observation well locations. These results (Figure 4.11) show $RMSE_c$ for the key phantom structures determined for each inversion. $RMSE_c$ generally increases as the number of wells increases, up until 100 wells. The reason for this is because, the fewer the number

of wells, the easier it is to fit a trend surface for those wells only. The larger the number of wells, the more points there are to fit and the more that the fit at one well can be offset by trying to fit to another well. Among 100, 250 and 500 wells there is no large difference in $RMSE_c$. As the number of phantom structures increases from 0 to 1, in all cases the $RMSE_c$ decreases. This is also usually the case for addition of a second and a third phantom structure. With 5 to 100 wells, change in $RMSE_c$ is more variable and does not follow a smooth downward trend.

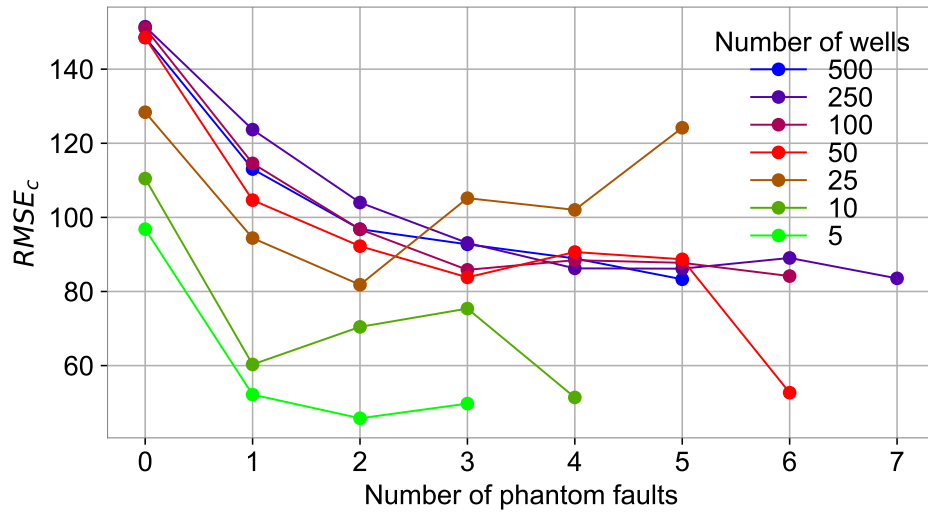


Figure 4.11: The $RMSE_c$ for all simulations with the same number of observation wells (taken as a mean across the three different observation well scenarios) for key phantom structures.

Assessing fit where real model is known

We compared the $RMSE_c$ calculated using data from observation wells to that calculated using data from the other cells in the model, excluding the observation wells (the filtered model) (Figure 4.12a–c). The $RMSE_c$ calculated with the observation wells represents the model fit that would be determined in the usual situation where the true properties of the real model are not known. This increases as the number of wells increases until 100 wells, then it does not change significantly between 500, 250 and 100 wells. $RMSE_c$ values for the filtered models (Figure 4.12a–c) follow an opposite trend. As the number of observation wells increase, the $RMSE_c$ decreases. The average misfit is higher overall for the cells of the filtered model than for the observation wells themselves. This suggests that the actual distribution of hydraulic head and groundwater age across the model becomes more divergent from the real model with fewer observation wells included in the inversion. For our model, 50 wells are required for a reasonable fit across the model domain.

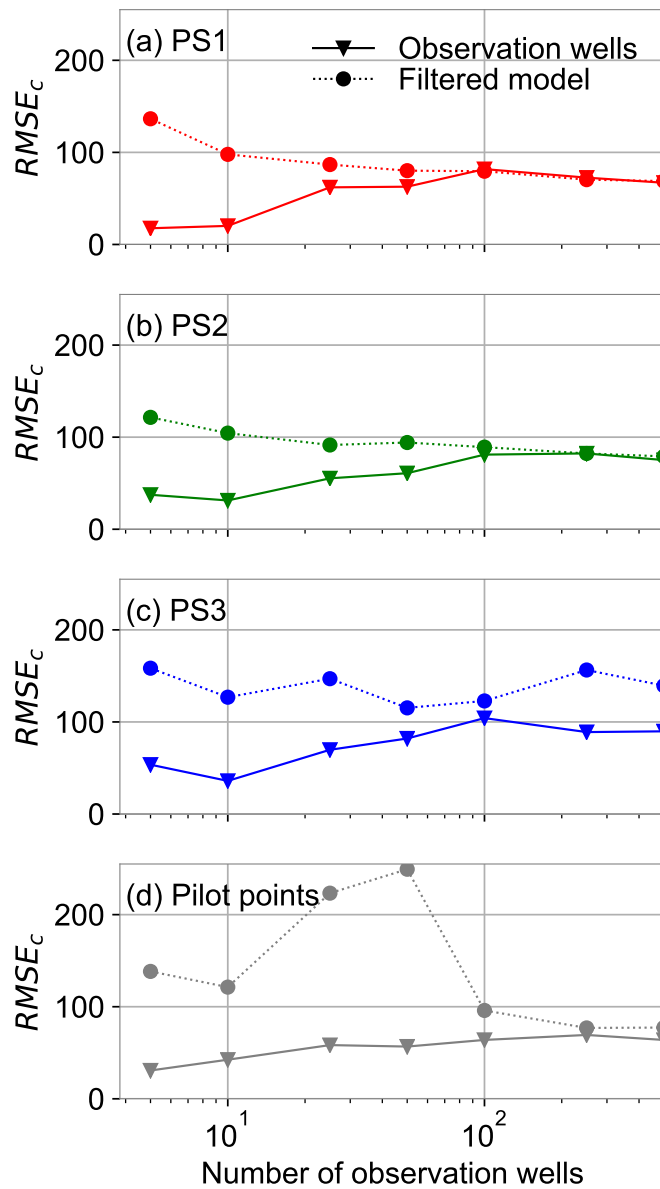


Figure 4.12: $RMSE_c$ values from model inversions using phantom structure configurations PS1 (a), PS2 (b) and PS3 (c), and from the model inversions using pilot points (d). $RMSE_c$ values are shown when calculated for observation wells only (solid lines with triangle markers) and for all cells in the filtered model that excludes observation wells (dotted lines with circle markers). Each marker represents the mean result of the three observation well configurations for that number of observation wells.

4.4.3 Pilot points

We again compared the $RMSE_c$ at the observation wells to the filtered model for the pilot point method (Figure 4.12d), which does not include the use of phantom structures. The $RMSE_c$ calculated with the observation wells shows a similar trend to that of the phantom structures as it increases as the number of wells increase.

For the filtered model, $RMSE_c$ decreases as the number of wells increase, with large additional increase for 50 and 25 wells. Across most of the observation well range, the filtered model $RMSE_c$ values are higher with pilot points than with phantom structures.

The posterior K field from the pilot point inversions with 500 and 250 wells (Figure 4.13a and b, respectively), show a zone of low K approximately at the same location as the real structure with a similar trending orientation. With the K fields with 100 and 50 wells (Figure 4.13c and d, respectively), we also visualise low K fields at approximately the same location as the real structure, but with less continuity. They consist of smaller, partially connected patches of low K rather than a single elongated low K zone. With 25 wells (Figure 4.13e), two small circular zones of low K are present on the upflow side of the real structure. The cases with 10 and 5 wells (Figure 4.13f and g, respectively) show almost homogeneous K fields with a similar K to the real model K_a of 1 m/d. In all cases, the K values are not estimated to be as low as the real structure K_b of 1e-3 m/d.

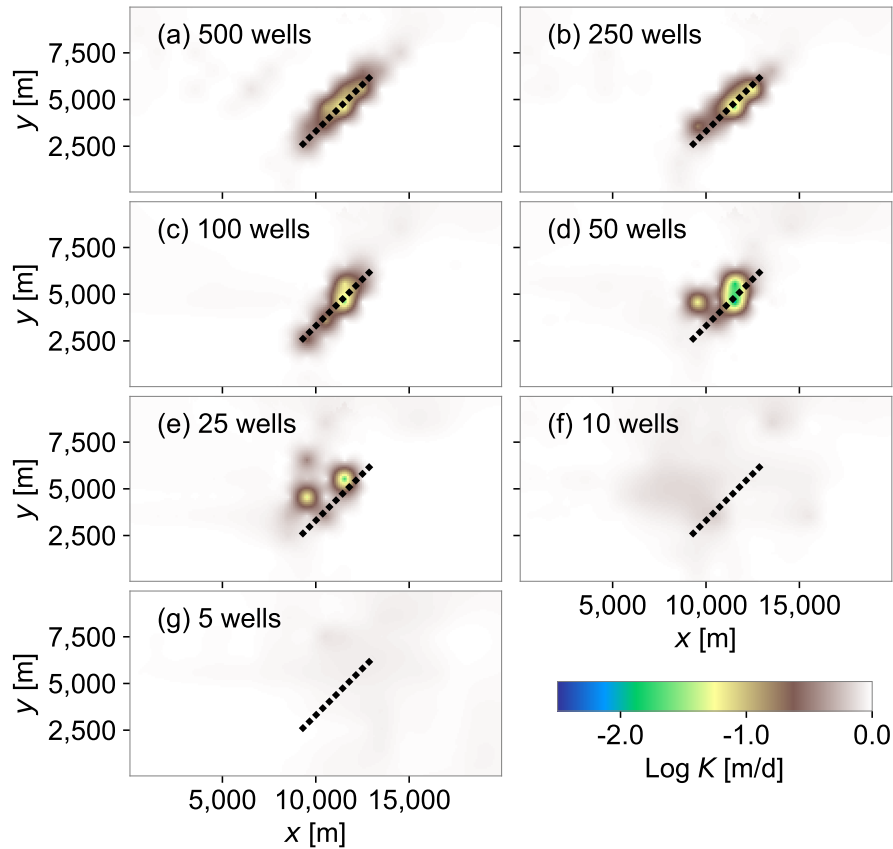


Figure 4.13: Inversion results for $\log K$ when using the pilot point approach with (a) 500, (b) 250, (c) 100, (d) 50, (e) 25, (f) 10, and (g) 5 wells and no phantom structures. Results shown are the mean results of the three different well configurations for that number of observation wells.

4.5 Discussion

Developing approaches to address conceptual model uncertainty (structural noise) in groundwater modelling studies is an established, and growing, field of study (Beven 2005; Enemark et al. 2019; Gupta et al. 2012; Ye et al. 2010). Innovative methods have also been developed to better understand uncertain model structures specifically (e.g. Chen and Rubin 2003; Harp et al. 2008; Koohbor et al. 2019). However, few are applicable to structures such as faults and dykes, which may only comprise a very minor spatial extent in an aquifer. This study demonstrates that groundwater model inversion can be used to conceptualise hydrogeologic barriers where no prior knowledge of them exists. The phantom structures method is not intended to reveal the exact properties of a natural system's barrier(s). Rather, the results indicate locations and geometries where barriers are likely to exist. We see that, for

most observation well scenarios, the phantom structures located closest to the real barrier are parameterised with a low K_b close to that of the real barrier. In many cases, only minor, localised variations exist in the distribution of hydraulic head and groundwater age when compared to the real model.

The ability to include hydrogeologic barriers with unknown geometric properties in model inversion depends on the number of observation wells used. The ability to identify a barrier using this approach is most optimal with 50 or more observation wells across the aquifer (or approximately one well per four square kilometres). However, given the high cost of drilling observation wells, this may be economically unfeasible. Using the value of $RMSE$ to evaluate the ‘success’ of a model inversion given a certain well density should be carefully interpreted. Using the phantom structures method, as the number of observation wells decreases, the value of $RMSE_c$ calculated at observation wells decreases. This is suggesting that there is a lower model-to-measurement misfit with fewer wells. However an opposite trend can be seen in the results when analysing the $RMSE_c$ calculated using data from the other cells in the model, excluding the observation wells (the filtered model). In this case $RMSE_c$ increases as the number of wells decrease. This shows that with fewer wells the actual ability of the inversion to reproduce the hydraulic head and groundwater age distribution is compromised.

We compared the results with phantom structures to that with pilot points, as using pilot points is a known approach for identifying regions of an aquifer with contrasting physical properties (Doherty 2003). When $RMSE_c$ is calculated for the observation wells, the results with pilot points were approximately the same as those for phantom structures. However, when $RMSE_c$ is calculated with the filtered model, the $RMSE_c$ is poorer with pilot points than with the phantom structures over much of the observation well range. This shows that using phantom structures has resulted in a better representation of hydraulic head and groundwater age across the model, likely because the sharp changes in hydraulic head and groundwater age are difficult to reproduce with the smoothed hydraulic conductivity profile generated using pilot points. One cannot definitively use these results to determine which method is superior. The best method should be based on the model purpose and the impact of hydrogeologic barriers on specific model predictions.

The results show that it is important to consider the location and type of observation data used in a model inversion. The sensitivities of the observation well data show that it is useful for hydraulic head data to be collected within approximately 2 km of the barrier. Steep hydraulic head gradients across barriers have been observed in other studies and often can be used to determine their properties (Bense and Van Balen 2004; Bense et al. 2003). Many of the inversions with few observation wells

close to the real barrier also resulted in a good distribution of phantom structures, however, showing that wells spaced further apart are still helpful for the delineation of geological structures. Nevertheless, the results are strengthened by including groundwater age alongside hydraulic head data. Our study shows that groundwater age data are useful when collected not only close to the barrier but also on the downstream side of the fault, in the trail of older groundwater that extends further away from the barrier. Incorporating groundwater age data in model inversions can shed light on groundwater system processes or parameterisations that may not otherwise be evident (Schilling et al. 2019). Although previous studies have utilised groundwater age data in model inversion (Konikow et al. 2008; Reilly et al. 1994; Sanford 2011; Zell et al. 2018), or tested how faults may impact groundwater age distributions (Castro and Goblet 2005; Janos et al. 2018; Marshall et al. 2020), very few studies have used groundwater age data in model inversions to identify or characterise structures such as faults and dykes.

Evaluating how many phantom structures are key in an inversion is important so that the smallest number of structures with the largest impact on hydraulic head and groundwater age could be determined. Regularisation is therefore critical as it plays a role in limiting the number of key phantom structures with low K_b values. We used a regularisation objective function that increases its penalty as the values of K_b diverges from K_a . Nevertheless, the inversions do not result in identifying a single structure exclusively, even though there is only one in the real model. The single example showed that most of the decline in $RMSE_h$, $RMSE_a$ and $RMSE_c$ was achieved with the two phantom structures that had the highest values of identifiability. The other results showed a similar pattern, that most of the decline in $RMSE_c$ was achieved with three phantom structures. However, the geometries of the phantom structures to begin with is also a critical factor in determining the final number of key phantom structures. With a smaller grid spacing over the same area, one can represent a greater variety of phantom structures, which would improve the likelihood that the geometric properties of phantom structures align with the real hydrogeologic barrier. The prior geometric properties of phantom structures could also be further refined, for example by using soft knowledge of known hydrogeologic barrier properties in a region.

4.5.1 Limitations and future studies

This study, although valuable for demonstrating a new method to include hydrogeologic barriers in model inversions, has limitations that could be further examined and extended upon in further studies. Four key limitations/extensions are described in the following paragraphs.

First, we focus on hydrogeologic barriers, rather than permeable features. Permeable structures do not necessarily result in sharp changes of hydraulic head and groundwater age and are therefore likely to be more challenging to identify using the phantom structure approach. Nevertheless, this could be investigated in more detail.

Second, the real model was controlled with fixed recharge and other model parameters. We know that recharge can control hydraulic head and groundwater age distributions across barriers, as can the geometry of the barrier itself (Marshall et al. 2020). Future studies could include additional parameters in the model inversion, such as heterogeneous K_a , recharge, transport parameters, and barrier geometries. It could also test variable grid configurations.

Third, our results show that an important variable is the location of the phantom structures to begin with. One hundred phantom structures were used in this study, but more could be included to increase the likelihood that one is located at the site of the real barrier. However, the number of phantom structures used depends on the grid spacing in the model. With a smaller grid spacing over the same area you can represent a greater variety of phantom structures, which would improve the likelihood that the geometric properties of phantom structures align with the real hydrogeologic barrier. For this study, we used a wide constraint to define the geometric properties of phantom structures, for example structures could be any length between 100 m and 10,000 m and at any orientation. However, these constraints can be further refined, for example:

1. Using soft (or quantitative) knowledge of known hydrogeologic barrier properties in a region; or
2. By implementing the process of inversion several times. Using the results from the first inversion could refine the geometric properties of phantom structures for a second inversion.

Another possibility that could result in better alignment of a single, calibrated model structure with a real structure would be to directly estimate the geometric properties of the phantom structures within the model inversion. This would allow the location, length and orientation of structures to be completely flexible and to be optimised based on the observation data. Other options for using pilot points to identify hydrogeologic barriers could also be tested, which would allow for more flexibility in the barrier location and shape. Using more pilot points would minimise their smoothing effect. However, the ability to include more pilot points depends on the computational resource available and could also result in parameter over-fitting (Moore and Doherty 2005). Alternatively, an interpolation algorithm that favours

sharp structures could be used instead of standard kriging (Doherty 2018a).

Finally, an important point to consider for future studies is that the approach taken to address uncertainty in model conceptualisation should depend on the specific study's purpose. A specific aspect of conceptual uncertainty, such as that arising from unidentified hydrogeologic barriers, is only relevant if it has an impact on the overall purpose of the modelling study. In our study we use model inversion to describe the hydraulic properties of an aquifer, not for a particular model prediction. The prediction of interest, and whether it is sensitive to a particular type of conceptual uncertainty, is paramount in considering how we address any conceptual uncertainty (Doherty and Welter 2010; Moore and Doherty 2005).

4.6 Conclusions

This study introduces a new method—phantom structures—for identifying the geometries and hydraulic conductivities of barriers in models. Phantom structures are a regularisation device that allow sharp structures, such as faults and dykes, to be included in a model inversion where no previous knowledge of their location exists. The results show that two to three phantom structures can reasonably and successfully reproduce hydraulic head and groundwater age distributions for a hypothetical, 'real' aquifer that has one hydrogeologic barrier. We found good agreement between the lengths, orientations and hydraulic conductivities of the key phantom structures and the real hydrogeologic barrier. The location and geometric properties of phantom structures approach the real structure when more than 50 observation wells were used in an inversion. They also indicate that hydraulic head data are most useful within approximately 2 km of the barrier. Groundwater age observations can also be useful when located at great distances downstream of the barrier, where groundwater age is higher due to the constricting presence of the barrier on groundwater flow. We compared the results with phantom structures to those with more traditional pilot points. As the number of wells decreases, both approaches become less successful in replicating the hydraulic head and groundwater age distribution across the model grid (not including observation wells). Yet we found that the fit was overall better with phantom structures than with pilot points over much of the observation well range. This shows that the method is successful when compared to pilot points for replicating groundwater flow resulting from sharp structures such as faults and dykes. The best approach to use, however, will depend on the purpose of a specific model inversion study. Overall, the novel phantom structures method shows promise for recognising and including hydrogeologic barriers in model inversions where their presence is not predetermined.

Chapter 5

Conclusions

5.1 Overview

Due to the hidden nature of the subsurface, it can never be perfectly represented by any model attempting to emulate its behaviour. This thesis employs different investigative approaches to the common problem of conceptual model uncertainty related to the distribution of geological structures, specifically hydrogeologic barriers. In groundwater systems, uncertainty in physical structures is one of the greatest issues in groundwater modelling because of incomplete sampling of the subsurface (Guillaume et al. 2016). In fact, according to Oreskes and Belitz (2001): “Conceptualisation is probably the most thorny issue in modelling”. The challenges related to uncertainty in hydrogeologic barriers pose important questions. What implications do the limitations in our knowledge of geological structures have on the outcomes of a modelling exercise? How can we best conceptualise complex geological structures using available field data? Can we design novel methods to advance modelling practices, in light of this geological uncertainty?

In order to address these questions, I have used analytical models, numerical models of groundwater flow and transport, and inverse models to explore the relations between groundwater pumping, aquifer properties, barrier properties, and hydraulic head and groundwater age data. Using a suite of models, from simple (i.e. analytical) to complex (i.e. three dimensional numerical and calibrated models), has several advantages. Simple models can be run thousands, or more, times and thus can investigate a plethora of parameter combinations otherwise not possible in a more complex model. This thesis demonstrates that they can therefore be employed as a guide to direct future data acquisition, or more complex modelling. On the other hand, three-dimensional modelling helps to show more realistically how a real aquifer system may appear. Complex geometries and processes that are not easily

represented in an analytical model can be captured. The systematic advancement from simple to complex modelling is a framework espoused by Doherty and Simmons (2013), among others, for conscientious modelling to support decision making. By employing a range of approaches, I have shown how the issue of understanding, detecting, and conceptualising hydrogeologic barriers in groundwater models can be approached from different angles.

As explained in Chapter 1, the objectives of this study stem from an overarching project based in the Pilbara region of Western Australia. This region is geologically complex and contains known flow barriers, mostly in the form of faults and dykes. In many regions, data collection is sparse and may be centralised around sites easily accessed, or where infrastructure exists. Indeed, in the Pilbara, data collection is concentrated in the immediate vicinity of mines, with fewer data available across the regional landscape (e.g. Cook et al. 2016). New and existing data collected at one particular field site within the Pilbara known as Baby Hope are summarised in Appendix A. The sharp hydraulic head changes across inferred barriers at this site provided part of the basis for the research questions in this thesis. After environmental tracer data (to infer groundwater age) were also collected, this led to questions about how sampled ages would be impacted by hydrogeologic barriers, ultimately leading to the outcomes of the modelling shown in Chapter 3 particularly. Although a complete analytical or numerical modelling study of Baby Hope, required to field-test the theoretical approaches demonstrated in the thesis, is not part of this thesis, a conceptualisation of the site has nevertheless been prepared (Appendix A). This demonstrates one example of the types of sites that require further insight into ways that hydrogeologists can consider hydrogeologic barriers in groundwater modelling studies.

Across the Pilbara, and across the world, geological structures such as hydrogeologic barriers are usually not detected or fully characterised. Groundwater models are nevertheless used to characterise groundwater systems containing such structures and to predict changes to them resulting from various climate or management scenarios. Each of the three bodies of research presented in this thesis are designed to address problems that are relevant to the mis-characterisation or non-inclusion of barriers in groundwater models. The objectives of the thesis grew from groundwater issues arising in the Pilbara and the outcomes are helpful when applied to this region. As a whole, however, the research in the thesis is general and not singularly focused on any one field region. Large-scale groundwater extraction is not only required in mining regions for dewatering, but it is common in urban and industrial areas for water supply purposes. In Chapter 2, this thesis helps to show the degree to which models of groundwater drawdown could be incorrect if barriers

are undetected. It quantifies the timescales over which this occurs. In Chapters 3 and 4, numerical modelling and inverse modelling studies are developed using hypothetical aquifer settings loosely based on the field characteristics in the Pilbara. The outcomes are relevant to the general pursuit of improving conceptualisation and prediction of groundwater systems with geological structures that are difficult to characterise.

5.2 Limitations and future work

Limitations specific to each study are included in the relevant chapters. Several limitations that span the research as a whole are summarised in the following paragraphs. These are augmented with suggestions for future work based on the findings of this thesis.

1. Incorporating geological structure heterogeneity

In this thesis we make assumptions about the characteristics of the hydrogeologic barriers modelled. In Chapter 2, the barriers are modelled as being completely impermeable, of infinite length, fully penetrating and with an aquifer that is homogeneous. In Chapters 3 and 4, barrier characteristics are of a constant thickness, linear, vertical, and their internal properties do not vary. In reality, faults can have complex permeability structures (Bense et al. 2013; Caine et al. 1996). Our modelling did also not account for anisotropy, for example where faults may act as barriers to perpendicular flow across the fault but as a conduits to flow in the vertical direction or along, parallel to, the fault (e.g. Gumm et al. 2016). Offset of stratigraphic layers or changes in topography across the barriers were also not considered. Using a simplified approach, however, can be an exceptionally useful first step for exploring the impact of the obstruction to groundwater flow caused by a hydrogeologic barriers without additional complexity to complicate any findings.

2. Testing approaches at a specific field study

The models used in this thesis were simplified and hypothetical, not intended to represent a particular field site. However, it would be beneficial to test the insights gained, and the new approaches developed, at a specific field site. This could include geological drilling across barriers, to understand the intricacies of their permeability structures. It could also be combined with other field-based data collection such as groundwater temperature data and geophysics to help understand groundwater flow dynamics at the site of hydrogeologic barriers. The conceptual model shown in Appendix A, of Baby Hope, would

be an appropriate site to apply a detailed modelling study.

3. Modelling surface discharge processes

Hydrogeologic barriers can strongly influence surface discharge processes. In this thesis, however, discharge at the surface was not considered and groundwater levels were consistently simulated to be below the top of the aquifer (and land surface). Future studies may consider testing various modes of spring discharge based on the presence of hydrogeologic barriers and how spring discharge may be impacted by groundwater pumping, for example.

4. Including environmental tracers

In Chapters 3 and 4, groundwater age was simulated directly, rather than simulating specific environmental tracers commonly used to estimate groundwater age. Previous authors have shown that when an aquifer is heterogeneous, the use of environmental tracers to determine groundwater age can be challenging (Larocque et al. 2009; McCallum et al. 2014a; Weissmann et al. 2002). Combining the collection of several environmental tracers with their simulation for the detection or characterisation of hydrogeologic barriers would be a natural extension of this research.

5. Calibrating for recharge

In Chapter 3, two variable recharge settings were tested. The results showed that recharge can significantly influence hydraulic head and groundwater age distributions across barriers. We did not, however, test variable recharge settings in Chapter 4. Recharge could also be included as an inversion parameter to be estimated during groundwater model inversion.

5.3 Summary of findings

The key conclusions from the three studies presented in this thesis are:

1. Understanding the effect of undetected barriers on groundwater recovery

This research shows that in areas with impermeable barriers, hydraulic head measurements made during pumping cannot reliably be used to predict recovery unless the presence and effects of the barrier boundary are recognised and accounted for. Problems will occur if impermeable barrier(s) exist outside the extent of drawdown induced during pumping. This finding is demonstrated using simple, non-dimensional analytical solutions based on the Theis (1935) solution to radial flow to a well, adapted using the principle of superposition

and image well theory. We establish the conditions under which barriers impact groundwater level recovery, expressed in terms of aquifer diffusivities, timescales, and distances from a pumping site to a barrier.

The research presented in Chapter 2 has improved the understanding of how lack of knowledge about hydrogeologic barriers can affect water level drawdown and recovery at sites with large-scale groundwater extraction. Specifically, they show that the magnitude of the impact from an undetected barrier will increase as the ratio of pumping rate to aquifer transmissivity increases. The timing of the maximum effect of a barrier on groundwater levels is proportional to the duration of pumping and will increase as the distance of the barrier from a pumping project increases. The results are exemplified for a hypothetical aquifer with an unknown barrier 3 km from a pumping well. The difference in drawdown between a model with and without a barrier may be < 1 m in the ten years while pumping is occurring, but up to 50 m after pumping has ceased.

2. Detecting hydrogeologic barriers using hydraulic head and groundwater age data

The research in Chapter 3 uses numerical simulations of flow and transport to simulate the effect of low-permeability, vertical, linear structures on hydraulic head and groundwater age distributions. Two key barrier types and two recharge settings were tested. For the Fully-penetrating barrier, hydraulic head data were found to be useful for barrier detection, given the sharp hydraulic head gradients. The hydraulic head distribution is significantly impacted by the barrier under both Uniform and Upgradient recharge settings. With the Buried barrier, hydraulic head measurements would be unlikely to reveal the presence of the barrier, regardless of the recharge scenario.

Using groundwater age to detect a barrier's presence was found to be possible with two cases, a Fully-penetrating barrier under Upgradient recharge or with a Buried barrier under Uniform recharge. In the first case, a strong contrast in groundwater age occurs across the barrier and the difference in age between the case with and without a barrier is 1.6 times the age of the groundwater in parts of the system. In the second case, the Buried barrier's presence causes reduced groundwater velocities in the lower half of the aquifer resulting in older groundwater banking up on the upstream side of the barrier. The usefulness of groundwater age data was found, therefore, likely to depend on the availability of depth-specific sampling.

Barrier orientation is shown to be crucial for whether, and where in the aquifer,

hydraulic head and groundwater age data could detect a barrier. For the Fully-penetrating barrier, only those with an angle $\geq 56.25^\circ$ to the principal flow direction with Uniform recharge, or $\geq 33.75^\circ$ with Upgradient recharge would be detectable using hydraulic head data. No barrier orientations had a measurable impact on groundwater age with Uniform recharge. Sensitivity analyses shows that the ratio of the hydraulic conductivity of the aquifer to that of the barrier and the width of the barrier are very relevant in determining the potential for a barrier's identifiability.

3. Conceptualising hydrogeologic barriers in groundwater model inversions

The research in Chapter 4 demonstrates that sharp barriers can be included in groundwater model inversion, even where their presence is uncertain, using the new approach introduced in this research of "phantom structures". Good agreement was demonstrated between the lengths, orientations and hydraulic conductivities of the key phantom structures and the real hydrogeologic barrier. The geometries of the phantom structures to begin with is also a critical factor in determining the final number of key phantom structures. We found that two to three phantom structures can reasonably and successfully reproduce hydraulic head and groundwater age distributions for a hypothetical, 'real' aquifer that has one hydrogeologic barrier. However, the prior geometric properties of phantom structures could also be further refined using soft knowledge of barrier properties in a region, which could result in a single, rather than multiple, phantom structures successfully reproducing the observation data.

The location and geometric properties of phantom structures approach the real structure when more than 50 observation wells (one observation well per four square kilometres) were used in an inversion. Hydraulic head data are most useful within approximately 2 km of the barrier. Groundwater age observations can also be useful when located at great distances downstream of the barrier, where groundwater age is higher due to the constricting presence of the barrier on groundwater flow.

The results are compared to model inversion using traditional pilot points. As the number of wells decreases, both approaches become less successful in replicating the hydraulic head and groundwater age distribution across the model grid (not including observation wells). Yet, the fit was better with phantom structures than with pilot points over much of the observation well range. The results of this study demonstrate that the geometric properties

of geological structures can remain flexible in a model inversion. This is a step towards reducing conceptual model uncertainty where the presence and properties of hydrogeologic barriers are undefined.

Overall, this research helps to show what the effects of complex geology, such as the geology of the Pilbara region, have on groundwater resources and on the use of groundwater models. It develops new approaches of aquifer characterisation, using modelling, to shed light on the conceptualisation of hydrogeologic barriers using commonly-collected hydrogeological datasets. This information is critical for making decisions now about how to minimise impacts on an aquifer system that may occur for many years into the future. The findings do not solve the issue of conceptual model uncertainty, which is a broad field and is the subject of extensive research (for a recent review see Enemark et al. 2019). However, they do contribute to improving groundwater modelling outcomes in regions that contain hydrogeologic barriers. The results contribute to further studies in aquifer structure detection, data inversion and monitoring network design. These results are important for the detection and characterisation of hydrogeologic barriers, which may play a significant role in the compartmentalisation of groundwater flow, spring dynamics, and drawdown and recovery associated with groundwater extraction.

Appendix A

Conceptual model of Baby Hope: a site in the Pilbara region of Western Australia

A.1 Introduction

This appendix describes a field site where the presence of hydrogeologic barriers are thought to occur. This site, known as Baby Hope, is an area in the Pilbara region of Western Australia, with planned iron ore mining. The underlying Archaen to Palaeoproterozoic geology has been significantly deformed structurally and intruded by dolerite dykes.

Two dolerite dykes have been mapped in the eastern part of the site. Two hydrogeologic barriers (with an unknown geology) have also been inferred in the western part of the site. Large head drops can be observed across each of these sets of structures. This forms part of the evidence for interpreting these geological structures as hydrogeologic barriers. The barriers have implications for the management of water resources at the site before, during and after scheduled open-pit mining. The barriers can influence volumetric estimates of mine dewatering, as well as groundwater flow to surface water systems and groundwater-dependent ecosystems.

Despite the significance of these inferred barriers, their hydrogeological properties are not completely known. To improve hydrogeological understanding of the site, new data were collected. These included environmental tracer data to interpret groundwater residence times and stable isotopes data to improve understanding of recharge mechanisms. However, in order to interpret this data and elucidate the characteristics of the barriers specifically, more understanding as to how barriers

control groundwater flow is required. The research presented in this thesis will assist with this.

Improving the understanding of how barriers can impact sites with large scale groundwater extraction, which occurs at iron ore mines that neighbour Baby Hope (and may possibly occur at Baby Hope in the future), is the basis for the technical study shown in Chapter 2. Better characterising how barriers control hydraulic head and groundwater age, so that new data can be interpreted at a site like Baby Hope, is the basis for the technical study shown in Chapter 3. Determining new methods for how barriers with unknown geological or hydrogeological properties can be included in a groundwater model, which could be eventually implemented at Baby Hope, is the basis for the technical study shown in Chapter 4. This appendix presents a real-world field site to which the research presented in this thesis is applicable.

A.2 Project background

The Hope Downs Iron Ore Project is located approximately 75 km northwest of Newman in the Pilbara region of northwestern Australia (Figure A.1a). Two existing major ore bodies, Hope Downs 1 North (HD1N) and Hope Downs 1 South (HD1S) (Figure A.1b), are currently mined to produce iron ore at a rate of 32 million tonnes per annum. A new development is beginning as a part of the Hope Downs Project at a site known as Baby Hope. The Baby Hope site is expected to be developed with three above water table pits, associated waste dumps, stockpiles, haul roads and infrastructure. Three mine voids will remain after mine closure (Hope Downs Management Services Pty Ltd 2000).

A.2.1 Site description

Baby Hope is situated within the Hamerley Basin, which extends over an area of approximately 40,000 km² in the Pilbara region (Rojas et al. 2018). Within the Hamersley Basin, the dominant landforms include ranges, river valleys and eroded plains. Surface water drainage predominately comprises ephemeral creeks (Vreeswyk et al. 2004). The Baby Hope site is located on the northern flanks of a broad shallow valley between two low ranges of hills within the Hamersley Range (Figure A.1c). The ranges and valley are oriented in an east-west direction. Mineralisation at Baby Hope primarily occurs within the Marra Mamba Iron Formation, which is above the water table. The deposit is approximately 8 km long and 1.5 km wide (Parrod 2019).

There is a major drainage line known as Pebble Mouse Creek that flows from west to

east through the valley. It is a tributary of the Weeli Wolli Creek. Weeli Wolli Creek, and its associated tributaries, flow in a northeast direction. The total catchment area of the Pebble Mouse Creek is 340 km² culminating at the confluence with Weeli Wolli Creek (Hamersley HMS Pty Ltd 2015). Pebble Mouse Creek is a generally well-defined, meandering creek and it contains minor braiding. It is a low-flow channel with an average width of 10 m and an average depth of 1.5 m. It is ephemeral and only flows as a result of intense rainfall. After significant rainfall, the drainage line floods and overbank flow events form (Hamersley HMS Pty Ltd 2015).

Surface water drainage in the Pilbara in general consists of sandy to gravelly channels that are mostly dry except during periods of flooding. Springs provide a permanent source of surface water, which are maintained by inflows from groundwater and are often downstream of geological structures (McKenzie et al. 2009). Weeli Wolli Spring is a natural surface discharge site of groundwater. It is located 8.2 km downstream of the Baby Hope site. The surface water catchment upstream from Weeli Wolli Spring has an approximate area of 1450 km² (RPS Group 2015). This spring is protected under the *Aboriginal Heritage Act 1972*. As a part of the HD1 Project, the site is managed to sustain spring flow to maintain the integrity of riparian vegetation supported by the creek system and protect the defined environmental values of the Weeli Wolli Spring and Creek. Dogramaci et al. (2015) studied the effect of continuous discharge of surplus mining water on the water budget of the Weeli Wolli Creek. Continuous discharge has occurred into the Weeli Wolli Creek due to mine dewatering since 2007. As a result, permanent pools have developed where previously there was previously only ephemeral flow.

A.2.2 Climate

In the Pilbara region, the climate is arid to semi-arid. It is defined by a hot summer from October to April and a mild winter from May to September. Most rainfall occurs during summer, from December to March. This is driven by the northern tropical rainfall system, which brings thunderstorms and occasional cyclones. A less dominant weather process is the southern winter rainfall system, causing some rain from April to June (Vreeswyk et al. 2004).

Data from three weather stations were used to determine rainfall and temperature conditions at the site: Marillana, Newman Aero and Prairie Downs (Bureau of Meteorology 2020). These are located approximately 50 km, 85 km and 60 km from Baby Hope, respectively (Figure A.1). Mean monthly rainfall varies between 2 and 64 mm and is often highest at the Marillana station (Figure A.2a). Mean maximum and minimum temperatures are greatest from November to February and are at their lowest from June to August. Mean maximum temperatures at Newman Aero

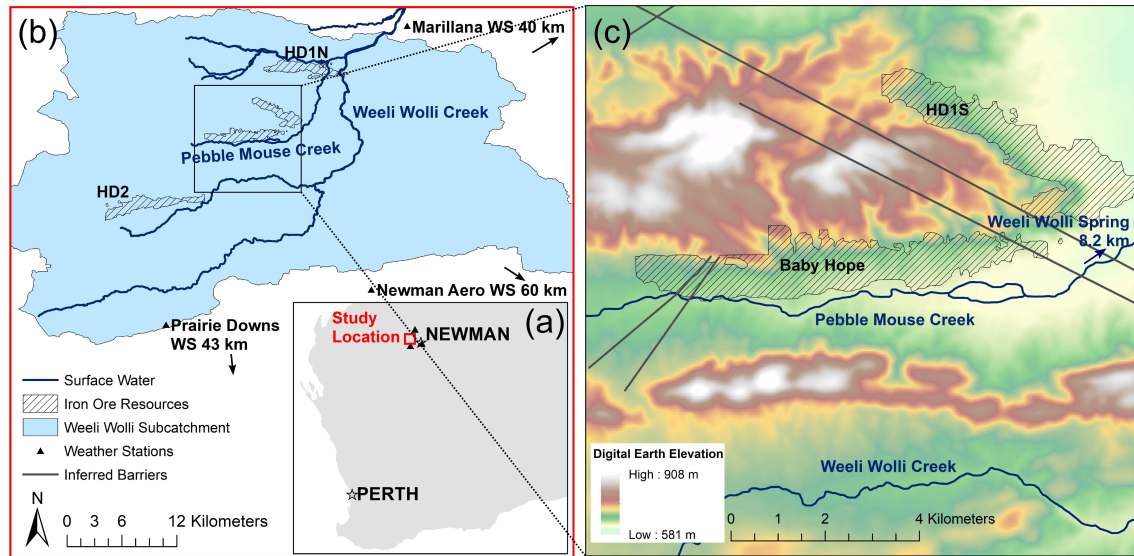


Figure A.1: Site description of Baby Hope region. (a) The study location in context of the Australian coastline and its proximity to cities Perth and Newman, including the locations of weather stations; (b) The study location in relation to the Weeli Woli catchment, note that weather stations (WS) are not on the map and the labels, along with the arrows, are used to show the approximate location and distance to them from the study location; and (c) the extent of the Baby Hope and HD1S ore deposits, including the digital elevation model (DEM), note that the Weeli Woli spring is not on this map and the arrow indicates the approximate direction and distance from the site to the spring.

reach approximately 40 °C and the minimums are as low as 6 °C (Figure A.2).

As well as variability between seasons, there is also large year-to-year variation in rainfall. The annual rainfall (data collected from Bureau of Meteorology 2020) calculated over periods of 1936–2020, 1971–2020, and 1968–2019 show large annual variation with minimum to maximum recorded rainfalls of 0–832 mm, 0–619 mm, and 0–626 mm, for Marillana, Newman Aero and Prairie Downs stations, respectively (Figure A.3). On average, potential evaporation exceeds average annual rainfall by a factor of up to 20 (McKenzie et al. 2009).

Some studies have reconstructed palaeoclimate in the Pilbara. For example, Rouillard et al. (2016) used an approximately 200-year sediment sequence from the Fortescue Marsh in the eastern Pilbara region to interpret the climate history of the region. They found that the wettest period in the last 2000 years has occurred between 1990 and the present day.

A.2.3 Hydrogeology

In general across the Pilbara, the hydrostratigraphy can be broadly subdivided into four main aquifer types (Johnson 2004):

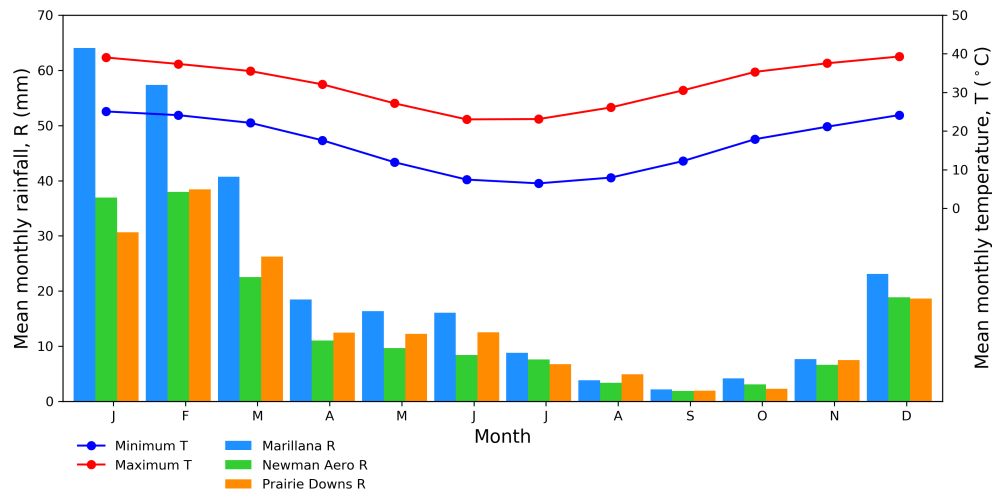


Figure A.2: Mean monthly rainfalls for Maillana, Newman Aero and Prairie Downs weather stations shown on the *left axis*. Mean monthly minimum and maximum temperature for the Newman Aero station is shown on the *right axis*.

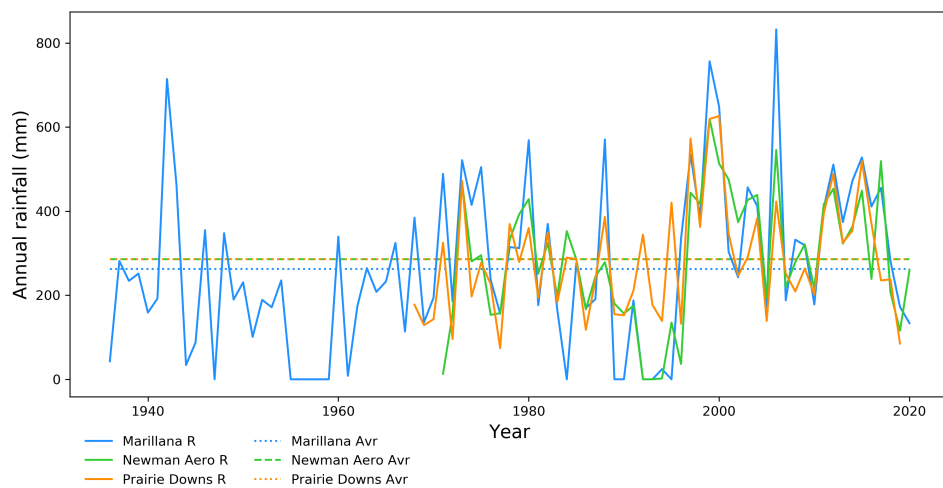


Figure A.3: Annual recorded rainfall for the Marillana, Newman Aero and Prairie Downs weather stations are displayed as *solid lines*. *Horizontal, dashed or dotted lines* show the average annual rainfall over the recorded time period. The average values for Newman Aero station and Prairie Downs station are almost indistinguishable at 286 mm and 285 mm, respectively.

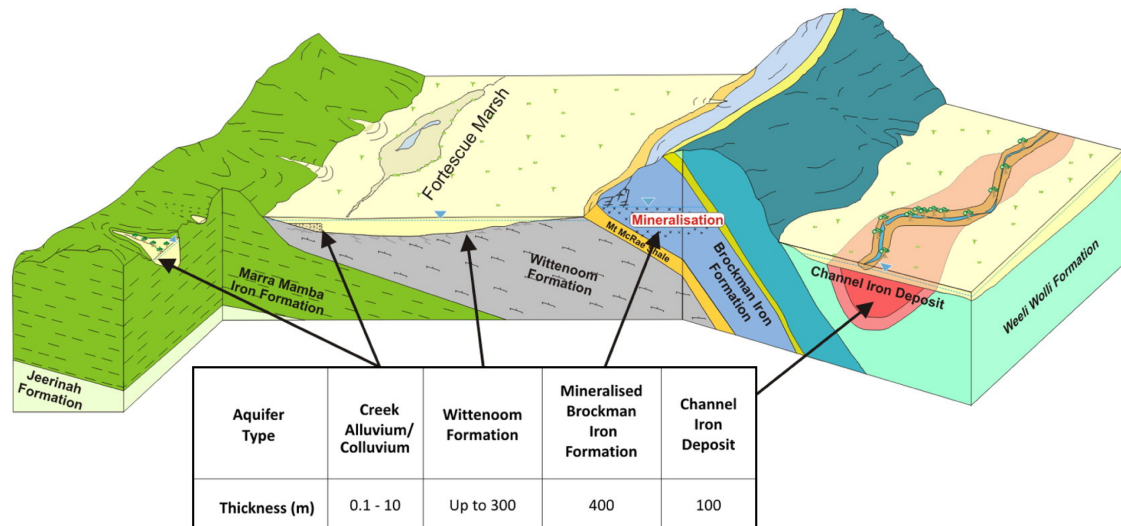


Figure A.4: Three dimensional conceptual model showing the main aquifer types surrounding the Fortescue Marsh, a region that is approximately 80 km northeast of Baby Hope (from Dogramaci and Skrzypek 2015).

1. Superficial aquifers in coastal and valley-fill alluvium.
2. Calcrete and pisolithic limonite aquifers.
3. Sedimentary rock aquifers in dolomites, banded iron and sandstone formations.
4. Fractured sedimentary and igneous rock aquifers.

Other important aquifers include inland valley aquifers and palaeovalley aquifers, including channel iron deposits, calcrete and gravels. Alluvial sediments associated with modern alluvial systems can also be important aquifers (McFarlane 2015). A conceptual model of the hydrogeology of the Pilbara region in general (depicting the region near the Fortescue Marsh, which is approximately 80 km northeast of Baby Hope) helps to demonstrate the variety of aquifer types occurring in this region (Figure A.4).

Within the Pilbara, the Hamersley Basin is formed from the approximately 1.5 km thick sediments of the Hamersley Group (Morris and Horwitz 1983). The Hamersley Group has three key water-bearing formations. From oldest to youngest these are the Marra Mamba Iron Formation, the Wittenoom Formation and the Brockman Iron formation (Dogramaci and Skrzypek 2015).

The Archaen to Palaeoproterozoic rocks of the Hamersley Group have been significantly structurally deformed and have been folded, faulted and intruded with dolerite dykes. The full impact of this structural deformation on groundwater flow is not completely understood. In parts of the Pilbara, there is evidence of groundwater divides (no-flow boundaries) occurring due to the presence of dolerite dykes.

The dewatering at HD1N itself is thought to be constrained by the presence of a large dolerite dyke (Latscha 2010). Yet each geological structure in the Pilbara has a different effect on groundwater levels. The hydrogeological properties of dykes, as well as of faults and other geological structures, is thought to vary from having no impact on groundwater flow to significantly impinging groundwater flow across the Pilbara (Latscha 2010).

Permeability characteristics of the main aquifers can vary greatly depending on a number of factors. The fractured rock aquifers often underlie alluvial aquifers. Hydraulic connectivity of alluvial aquifers and underlying aquifers depends on local conditions and the presence or absence of confining units (Rojas et al. 2018). Enhanced permeability is associated with mineralised successions of the Mount Newman Member of the Marra Mamba Iron Formation and the West Angela Member of the Wittenoom Formation (Dogramaci and Skrzypek 2015). Iron ore formation generated a network of fractures, resulting generally in areas of increased hydraulic permeability (Dogramaci et al. 2012). This effect is heterogeneous across the Pilbara, depending on topography and existing structural geology. It is expected that the un-mineralised Marra Mamba Iron Formation (MacLeod and Nammuldi Members) and the Mount McRae Shale form no-flow groundwater boundaries.

The Wittenoom Formation consists of interbedded shale, dolomite, sandstone and mudstone. It conformably overlies the Marra Mamba Iron Formation and is overlain by the Brockman Iron Formation. Extensive resource drilling and hydrogeological studies across the catchment has shown that the primary permeability occurs within this formation to an average depth of approximately 100 m. Whether or not the Wittenoom Formation forms an aquifer depends on whether or not significant weathering and karstification processes have occurred. The Wittenoom Formation has been estimated to have a hydraulic conductivity value of 50–100 m/d (Kellogg Brown Root 2008). These estimates were made using pumping tests.

The Baby Hope site is situated within an alluvial valley underlain by the Wittenoom Formation and Marra Mamba Iron Formation. The alluvial valley is separated by the unmineralised Marra Mamba Formation and the Jeerinah Formation in the north and the southern boundary is defined by the McRae Shale Member of the Brockman Iron Formation (Parrod 2019).

The main aquifer at Baby Hope comprises the Tertiary Detrital sediments and the Wittenoom Formation collectively. These are hydraulically connected and their porosity and permeability depend on the degree of weathering (Parrod 2019). Surficial, Tertiary Detrital sediments comprise alluvial silts, clay, pisolite and calcrete. Cross sections in the N-S and E-W orientations through the Baby Hope site (Fig-

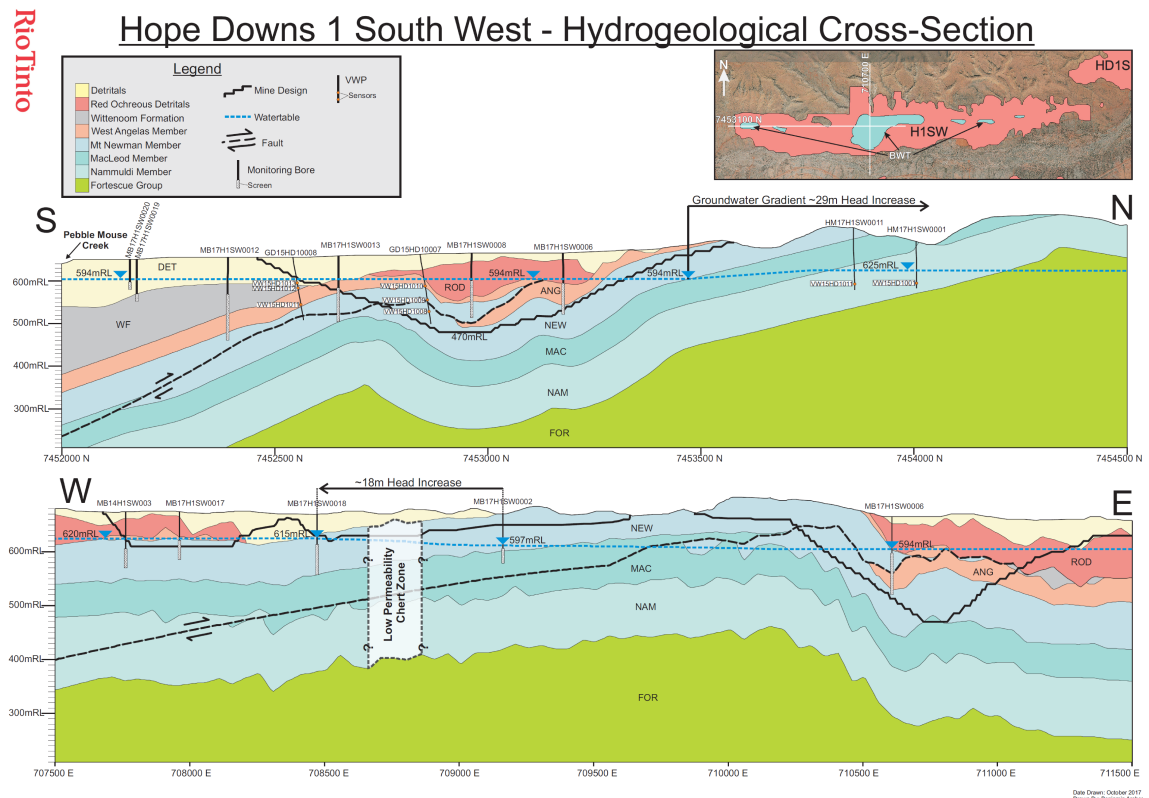


Figure A.5: N-S and E-W oriented cross-sections through the Baby Hope deposit (G. Kirkpatrick, 2020 pers comms.).

ure A.5) show that the thickness of the aquifer varies considerably across the site. In the N-S direction, it thickens towards Pebble Mouse Creek, in line with being part of an alluvial valley. The Tertiary, surficial units ('Detritals' and 'Red Ochreous Detritals') and the Wittenoom Formation together are between 100–200 m thick.

These cross sections, provided by Rio Tinto (G. Kirkpatrick, 2020 pers comms.), shows the mine design as occurring below the water table, although other reports have stated that the Baby Hope mine will occur above the water table and will not require dewatering (Hope Downs Management Services Pty Ltd 2000). In addition, it shows a low-angle thrust fault occurring predominantly within the Mt Newman and MacLeod Members, the hydrogeological implications of which are unknown. Based on these cross sections, Rio Tinto interpreted the aquifer to be 174 m thick (Figure A.6).

A three dimensional geological model using the software Leapfrog has been developed for the Baby Hope site to investigate its geology (Parrod 2019). Cross-sections through this model show the simplified stratigraphic framework of the Detrital Formations overlying the Wittenoom Formation and the Marra Mamba Formation (Figure A.7 and Figure A.8). The model illustrates the variation in stratigraphic thicknesses and the implications of the central thrust fault in controlling the stratigraphy

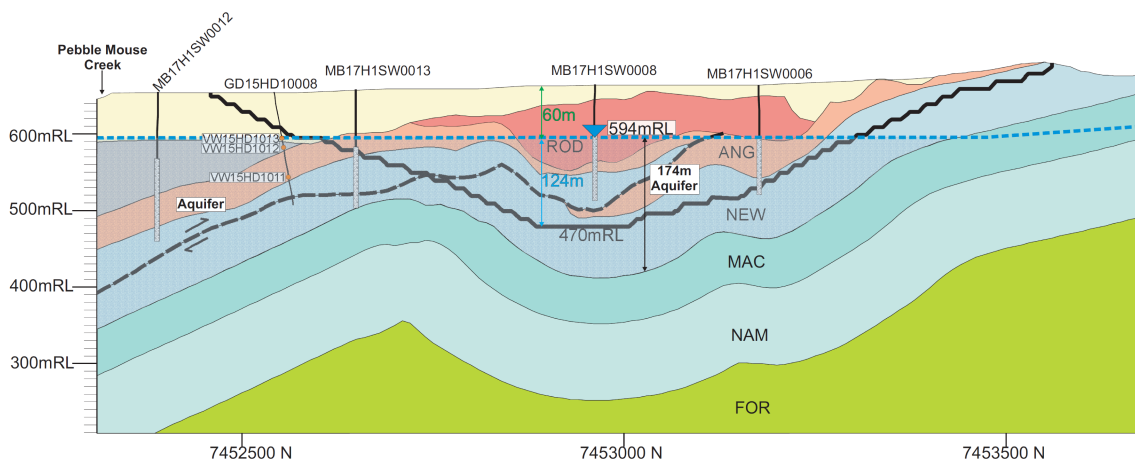


Figure A.6: Hydrogeological conditions interpreted from the E-W oriented cross-section through the Baby Hope deposit shown in Figure A.5 (G. Kirkpatrick, Rio Tinto 2020 pers comms.).

(Figure A.7). It also shows the role of the dolerite dykes in the eastern side of the deposit in controlling hydraulic heads (Figure A.8). Despite this interpretation, at the Baby Hope site the hydrogeology is still not well understood, as groundwater monitoring is focused on areas to be mined with fewer wells spaced regionally across the Weeli Wolli catchment. Wells are also generally developed with large screened intervals, designed for dewatering, rather than for targeting specific aquifer formations.

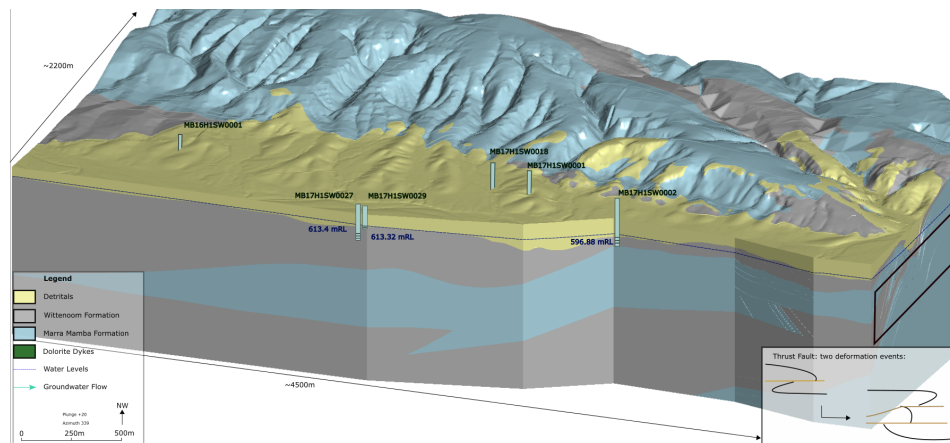


Figure A.7: Three-dimensional geological model interpretation of the western side of the site.

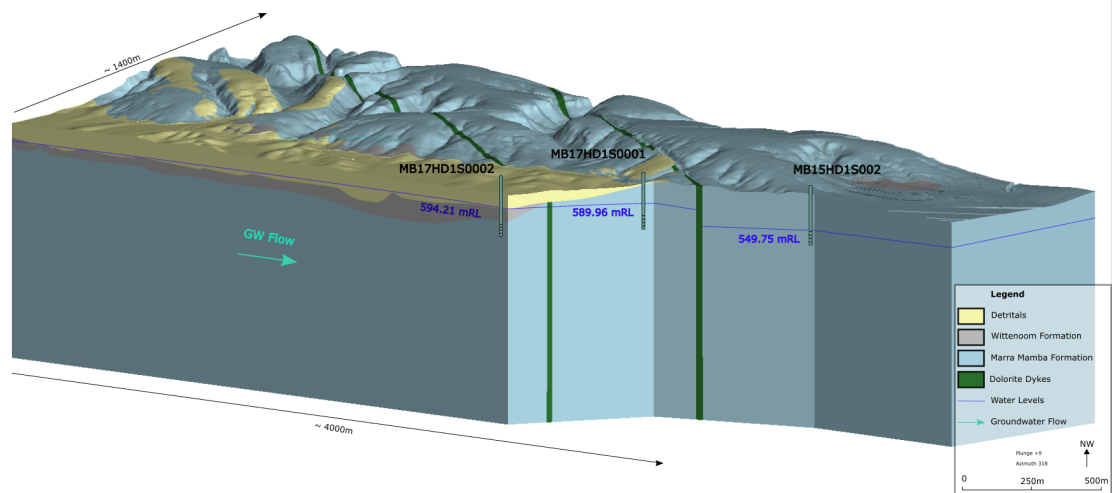


Figure A.8: Three-dimensional geological model interpretation of the eastern side of the site.

A.2.4 Groundwater recharge

There have been no specific studies of recharge in the Baby Hope region. There is some understanding of recharge process across the Pilbara, however. Recharge processes include both diffuse (i.e. rainfall infiltration) and point (or line) source (i.e. infiltration from ephemeral creeks and mountain fronts) recharge (Dogramaci and Skrzypek 2015). Groundwater recharge is associated with high precipitation events at times of low evaporation (Dogramaci et al. 2012). Recharge to the fractured rock aquifer, where it underlies the alluvial aquifer, is also thought to occur when water levels in the alluvium aquifer are high, such as after a flood. A study by McCallum et al. (2017) found that four primary age distributions are present in Pilbara groundwater: (1) less than 20 years old; (2) between 50 and 200 years; (3) between 100 and 600 years; and (4) between 1000 and 2000 years. In this paper, the authors employed a multi-tracer technique using ^3H , ^{85}Kr , CFCs, SF_6 , ^{39}Ar and ^{14}C to assess the groundwater age distribution. The results correlate well with rainfall episodes determined by studies of palaeoclimate by Rouillard et al. (2016).

Diffuse recharge

Rainfall infiltrates directly to the fractured rock system via preferential pathways in the fractures. A minimal amount of evaporation is thought to occur during this process and recharge water can be quite fresh (Dogramaci and Skrzypek 2015). However, according to Pham (2016), in a different part of the Pilbara (the West Angeles area), direct rainfall recharge is expected to be low due to the low rainfall, the depth to groundwater and the thickness of the detrital sediments. Recharge has been estimated to be between one and three percent of rainfall annually (Dogramaci

and Dodson 2009).

Point source recharge

Dogramaci et al. (2012) used the isotopic characteristics of rainfall, groundwater and surface water to assess the significance of rainfall to recharge to aquifers in the Pilbara. The authors found that intense rainfall events of > 20 mm with limited evaporation prior to infiltration contribute most to recharge. A study by Cook et al. (2020) estimated that the recharge rate due to infiltration of surface water is approximately 1 mm/y.

A.2.5 Groundwater chemistry

In the Hope Downs area, natural groundwater is considered to be fresh and slightly alkaline with reported concentrations of total dissolved solids (TDS) ranging from 260 to 540 mg/L and pH ranging from 6.7 to 8.1 (Hope Downs Management Services Pty Ltd 2000). In general, the TDS concentrations increase downstream (Hope Downs Management Services Pty Ltd 2000). Groundwater at HD1 is fresh, with TDS generally in the range of 600–700 mg/L. This groundwater contains ions mostly of magnesium, calcium and bicarbonate (Cook et al. 2016).

A.2.6 Hydrogeologic barriers

Several hydrogeologic barriers are inferred to occur in the Baby Hope area. Two barriers (or possibly one single barrier) are inferred on the western end of the Baby Hope Deposit (Figure A.1c). These will be referred to as the ‘Western Barrier(s)’. Two barriers are also inferred on the eastern end of the deposit, between Baby Hope and HD1S, these are referred to as the ‘Eastern Barrier(s)’. All barriers were identified by Latscha (2010).

Western barrier(s)

A NE-SW trending structure was identified based on groundwater levels falling from 615 m Reference Level (mRL) to 595 mRL over 500 m. It is not considered to be a narrow linear structure such as a dyke and no dolerite has been observed in drill cuttings. The structure is interpreted to be a massive chert band within the Wittenoom Formation and may be as wide as 500 m (Latscha 2010).

Eastern barrier(s)

Approximately 6.5 km away from the Western Barrier(s), two NW-SE trending hydrogeologic barriers have been mapped. These dykes have been confirmed by

geological mapping and drilling. These are interpreted to be dolerite dykes and act as low-permeability barriers where hydraulic head drops from 593 mRL to 573 mRL in an easterly direction. In addition, dewatering of wells at HD1S do not appear to impact groundwater levels to the west of the structures, which is more evidence that they are likely to be low-flow barriers. The dykes are dipping in the north-northwest direction with an angle of approximately 90° and are estimated to be approximately 25 m thick (Parrod 2019). The 3-D geological model has interpreted well logs to show that the barriers are inferred to extend through the Wittenoom and Marra Mamba Formations, but are overlain by and do not intrude through the Tertiary Detritals.

A.3 Groundwater data

Well data has been made available by Rio Tinto for 49 wells across the site (Table A.4 and Table A.5, Figure A.9). Most of the wells are located within the Baby Hope footprint both north and south of the Pebble Mouse Creek. The majority of wells are completed with 50–100 mm diameter steel casing. Well depths range from 41.6 m below ground level (BGL) to 182 m BGL. Screen intervals are up to 160 m long.

Of these wells, 47 have available static water level data and 33 have transient water level data. The wells were sampled at different times between July 2006 and August 2016. Approximately one third of all available groundwater level data did not have a recorded date attributed to the record. Very little change in water level has occurred in these wells over time, except where wells have been impacted by groundwater pumping in the vicinity of HD1S. Most wells had detailed construction information, including screen intervals and top of casing (TOC) measurements. However, some only had an elevation measurement and not a TOC. In cases where both elevation and TOC data are available, in some cases these values are equivalent but not in all cases. Radiocarbon data are available for 15 wells. These data were processed in October 2019. CFC data are available for 13 wells, where a sample from each well was processed twice. These samples were processed in July and August 2019. Stable isotope data ($\delta^{18}\text{O}$ and $\delta^2\text{H}$) are available for 18 wells, these data were processed in August 2018.

The practice for sampling the groundwater wells was to sample them through a nylon tube attached to production bore taps using brass fittings, for wells that are production wells. These wells that were pumping at the time of sampling did not require purging, but purging was conducted where necessary. Samples for radiocarbon analyses were collected in 500 mL HDPE bottles. Radiocarbon samples were analysed by the GNS Rafter Radiocarbon Laboratory (New Zealand). Radiocarbon

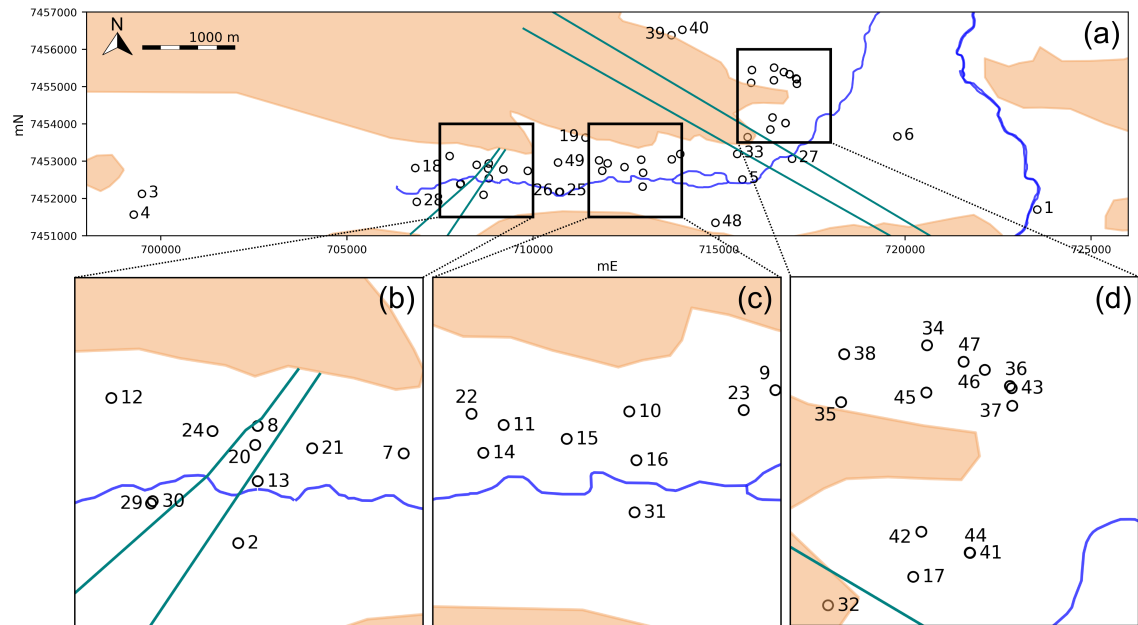


Figure A.9: Groundwater wells across Baby Hope site. Wells are represented by *open circles*, inferred hydrogeologic barriers by *teal lines*, surface water features by *blue lines* and aquifer boundaries by *light brown patches*. Numbers are referred to as ‘Well Reference (WR)’ in Table 4.

isotope data are reported in delta notation, as per mil (‰) and ^{14}C are also reported in percent modern carbon (pmC) according to the convention described in Stuiver and Polach (1977). Samples for CFC analysis were collected in 125 mL clear glass bottles with metal screw lids and analysed for CFC-11, CFC-12, and CF-113 concentrations by gas chromatography using a purge and trap system with electron capture detector at the GNS Water Dating Laboratory, New Zealand.

A.4 Hydraulic head data

A.4.1 Steady state, pre-pumping data

Steady-state hydraulic head data were interpreted based on water level data collected across the site. For each well, where only one data point was provided, that value was used. Where more than one data point was provided, if those values did not vary significantly (i.e. by greater than 1 m), an average of the values was used. In some parts of the site, the water level data was influenced by groundwater pumping and showed a significant decline in water levels. In these cases, the earliest, pre-pumping water level measurement was used.

Higher water levels in the western part of the site and lower water levels in the southern part of the site indicate that groundwater flow is from west to east. This reflects the same flow direction as the surface water systems towards the discharge point of

Weeli Wolli spring, to the northeast of the Baby Hope. The steady-state hydraulic head data (Figure A.10) show higher hydraulic heads in the western side of the site with highs of 627 mRL at wells LHRP13 and LHRP3. Across a flow path of approximately 3.5 km to the western-most inferred dolerite dyke (to wells MB17H1SW0027 and MB17H1SW0029), the water level decreases approximately 14 mRL to 613 mRL (gradient of 0.004 m/m). Across the two inferred Western Barriers, the water level drops to 595 m, which is a change of 18 m over approximately 250 m (gradient of 0.072).

In the centre part of the aquifer, between the Western and Eastern Barriers, water levels do not significantly change through time. All water levels are between 593–595 mRL, except for WB16BHT0001 with a water level of 590 mRL and MB16H1SW0002 with a water level of 614 m. These wells are a further distance from Pebble Mouse Creek than the other wells. It would be helpful if more wells were located some distance south of Pebble Mouse Creek to understand if there is lateral flow in the south to southeast direction, or if this data point just represents an anomaly. In the centre part of the aquifer, between the Western and Eastern dykes, the water level change is at most 2 m, over a distance of approximately 3.2 km (gradient of 0.0006). Across the Eastern Barriers, the water level drops from 593 mRL to approximately 574 mRL (wells PZ07HD1S010 and PZ07HD1S011). This indicates a head drop of 19 m over a distance of approximately 400 m (gradient of 0.05). To the east of the Eastern Barriers, again water levels do not appear to significantly change. To determine a gradient for this part of the aquifer, it would be reliable if additional wells were located in the north-eastern part of the aquifer. However, due to groundwater pumping at HD1S, any new wells drilled in this area would not provide steady-state data for appraisal of the pre-pumping potentiometric surface.

A.4.2 Transient data

Transient water level data from the area of the aquifer west of the Western Barriers show (Figure A.16) that all water levels are within the range of 612–621 mRL. Each well shows a water level trend that is largely constant and show no evidence of seasonal or long-term trends. Transient water level data from the area between the two inferred Western Barriers also show that water levels have largely remained constant (Figure A.17). For well MB13H1SW002 (WR 8), data are available from the beginning of 2014 until 2018. Some minor (< 1 m) seasonal variation in water levels appear to exist but overall water levels have been constant at approximately 599 mRL throughout that time.

Transient water level data from the middle part of the aquifer between the Western

in 2010.

A.5 Groundwater chemistry

A.5.1 Radiocarbon data

Radiocarbon data are available for 15 wells across the site (Table A.1). Thirteen of these samples were collected recently, for this study, but two sample results have been taken from Cook et al. (2016), as indicated in the table.

Site ID	WR	Date analysed	$\Delta^{13}C$ [‰]	$\delta^{13}C$ error	$\Delta^{14}C$ [‰]	$\delta^{14}C$ error	pmC
HDD0004	1	27/09/2019	-13.11	0.2	0.98	3.2	100.1
LHRP1	2	27/09/2019	-10.57	0.2	-822.28	3.58	17.77
LHRP4	5	27/09/2019	-10.47	0.2	-749.57	3.35	25.04
MB16H1SW0001	18	27/09/2019	-10.22	0.2	-900.13	3.83	9.99
MB17H1SW0018	24	27/09/2019	-9.81	0.2	-932.98	3.95	6.7
MB17H1SW0019	25	27/09/2019	-10.86	0.2	-727.77	3.29	27.22
MB17H1SW0020	26	27/09/2019	-15.11	0.2	-527.24	2.87	47.28
MB17H1SW0024	27	27/09/2019	-12.7	0.2	-711.43	3.25	28.86
MB17H1SW0027	29	27/09/2019	-10.46	0.2	-721.64	3.28	27.84
MB17H1SW0029	30	27/09/2019	-13.78	0.2	-407.33	2.75	59.27
MB17H1SW0030	31	27/09/2019	-11.02	0.2	-630.24	3.06	36.98
MB17HD1S0001	32	27/09/2019	-13.08	0.2	-505.71	2.82	49.43
MB17HD1S0002	33	27/09/2019	-10.55	0.2	-826.22	3.59	17.38
WB10HD1S001	46	-	-11.4	-	-	-	39.8
WB10HD1S002	47	-	-10.9	-	-	-	35.2

Table A.1: Radiocarbon data. Data for WB10HD1S001 and WB10HD1S002 are collated from Cook et al. (2016), the remaining data were newly collected by Rio Tinto for this study.

Some gradation exists from older groundwater with lower pmC to younger groundwater with higher pmC in the direction of groundwater flow. This trend of older groundwater in the western part of the catchment can be observed where the data are plotted in cross section (Figure A.11). It also shows that, in general, younger groundwater occurs in the shallower parts of the aquifer and older groundwater occurs in the deeper parts of the aquifer. An interesting feature is that WR 32 and WR 33 are approximately the same depth, but have quite different values of pmC (49.43 and 17.38 respectively). This is suggesting that WR 32 has sampled groundwater that is younger than WR 33. WR 32 is between the two Western Barriers and WR 33 is between the Eastern and Western Barriers, in the central part of the aquifer. WR 1 has very young groundwater, with pmC of 100.1. This well is located

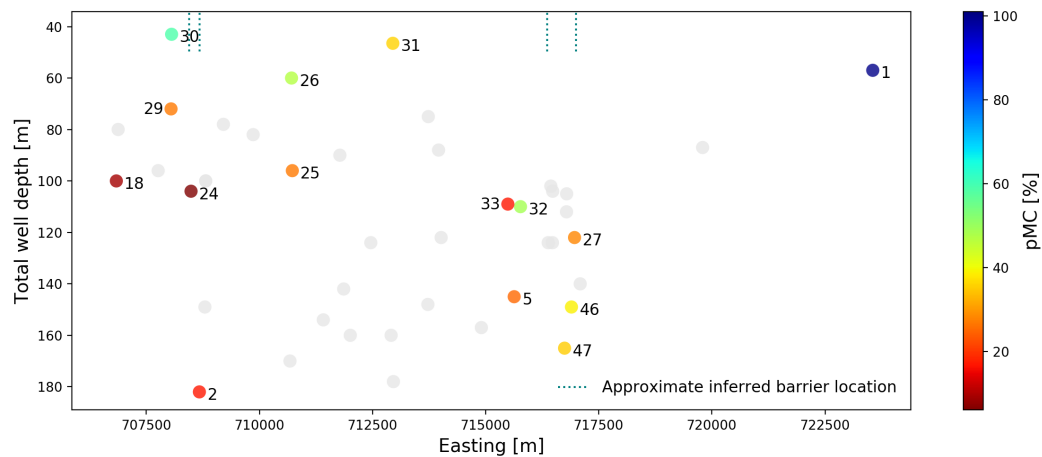


Figure A.11: Radiocarbon data (pmC) in cross section below water table, where the x -axis shows the Easting of the well and the y -axis shows the total well depth. Coloured dots represent wells for which a radiocarbon measurement is available and the colour is scaled by the value of pmC as shown on the scale bar. Grey dots show wells for which no radiocarbon value is available. Teal dotted lines show the approximate location of inferred barriers, note that their Easting depends on the Northing value of the cross section, which is not shown, so barriers are indicated to just penetrate the upper part of the aquifer for an approximate guide. The number next to each circle represents the sample's Well Reference number.

adjacent to the Weeli Wolli Creek and could indicate a high connectivity between surface water and groundwater at this location.

When the data are plotted to compare the depth of the well screen with the value of pmC (Figure A.12), we see that there is some relation between the depth of the well screen and the value of pmC. However, this trend is not strong, and some samples with relatively shallow screens (i.e. WR 18 and WR 24) also have low values of pmC, indicating that the groundwater is relatively old. Both of these samples are in the western part of the catchment and are located to the west of the Eastern Barriers. This could potentially indicate that some anomalously older groundwater occurs upstream of these barriers.

A.5.2 CFCs

CFC data are available for 13 samples across the site, where duplicate samples for CFC analysis were collected on most wells (Table A.2). CFC-12 data shown in cross section (Figure A.13), indicating that there is no clear trend between location in the aquifer and the value of CFC-12. Again, as was seen by the values of pmC, we can see that there are two samples located at approximately the same depth and within a close distance, WR 32 and WR 33. The results for CFC-12 show that the value is higher in WR 32, which is between the two Western Dykes. WR 25 also appears to have anomalously high values (indicating younger groundwater) of

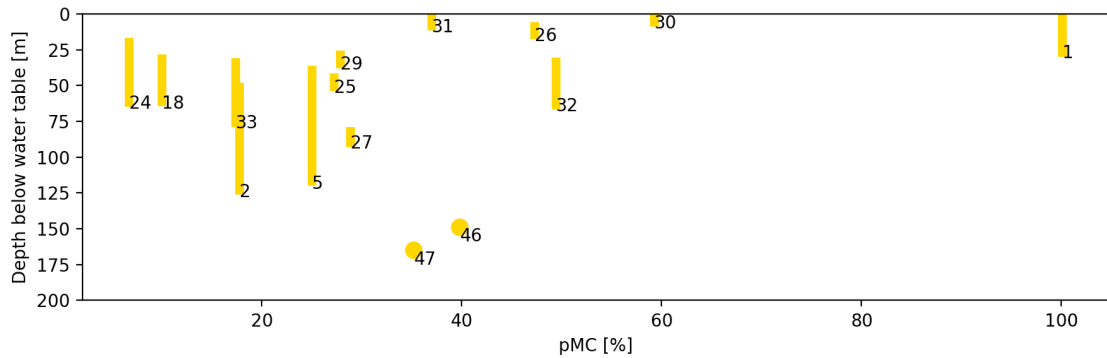


Figure A.12: Measured value of pmC compared to the depth of the well screen below the water table are shown by the *yellow lines*. Note that WR 46 and 47 either did not have well screen information or groundwater level data available so they are represented as a *circle* denoted by their total well depth.

Site ID	Well Reference (WR)	Sampling Date	CFC-11 [pg/kg]	CFC-12 [pg/kg]	CFC-113 [pg/kg]	Temperature [°C]	Excess Air [mL(STP)/kg]
HDD0004	1	01/08/2019	155.2	171.7	31.9	23.9	8.6
HDD0004	1	01/08/2019	175.8	168.1	35.6	23.9	6.6
LHRP1	2	20/07/2019	9.6	4.8	3.7	30.2	3.6
LHRP1	2	20/07/2019	19.2	13.3	3.7	31.7	5.8
LHRP4	5	20/07/2019	2.7	26.6	3.7	29.3	4.4
LHRP4	5	20/07/2019	19.2	26.6	3.7	28.8	3.3
MB16H1SW0001	18	03/08/2019	26.1	14.5	5.6	27.8	4.3
MB16H1SW0001	18	03/08/2019	24.7	14.5	7.5	28.6	4.2
MB17H1SW0018	24	03/08/2019	23.4	9.7	7.5	33.8	3.9
MB17H1SW0018	24	03/08/2019	26.1	9.7	5.6	32.7	3.5
MB17H1SW0019	25	03/08/2019	513.7	185.0	33.7	13	10.3
MB17H1SW0019	25	03/08/2019	501.4	180.2	39.3	13.3	9.4
MB17H1SW0020	26	03/08/2019	1.4	101.6	1.9	23.7	5.1
MB17H1SW0020	26	03/08/2019	13.7	107.6	7.5	24.3	6.3
MB17H1SW0024	27	20/07/2019	37.1	41.1	7.5	28.8	0.6
MB17H1SW0024	27	20/07/2019	42.6	49.6	9.4	29.1	0.4
MB17H1SW0027	29	20/07/2019	0.0	8.5	1.9	30.8	4.6
MB17H1SW0027	29	20/07/2019	5.5	13.3	3.7	32.8	4
MB17H1SW0029	30	03/08/2019	1.4	71.3	3.7	31.1	1.8
MB17H1SW0029	30	03/08/2019	33.0	73.8	5.6	31	2
MB17H1SW0030	31	03/08/2019	37.1	18.1	0.0	26.8	1.1
MB17H1SW0030	31	03/08/2019	35.7	19.3	7.5	26.9	1.3
MB17HD1S0001	32	20/07/2019	64.6	70.1	13.1	22.6	2.3
MB17HD1S0001	32	20/07/2019	59.1	50.8	9.4	20.8	1.2
MB17HD1S0002	33	20/07/2019	11.0	10.9	3.7	31.2	2.1
MB17HD1S0002	33	20/07/2019	5.5	20.6	5.6	28.4	1.9

Table A.2: CFC data for baby Hope samples.

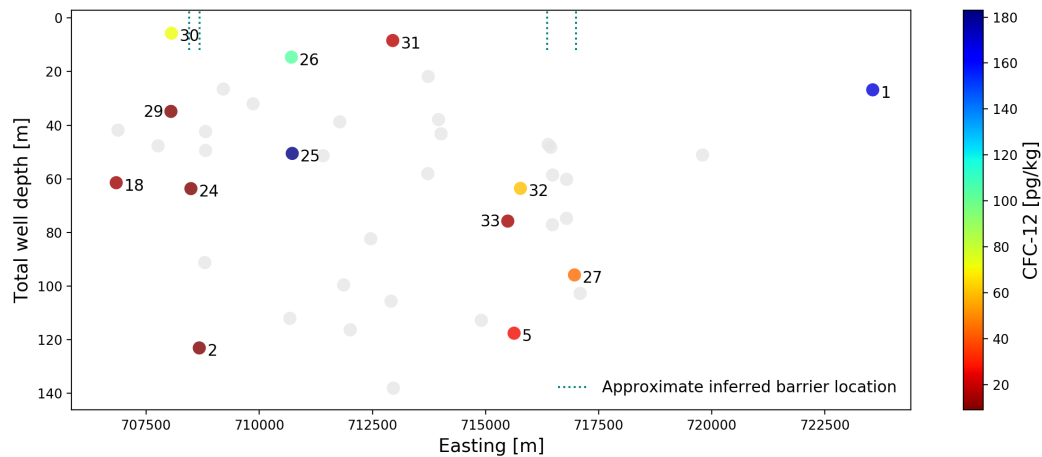


Figure A.13: CFC-12 data in cross section below water table, where the x -axis shows the Easting of the well and the y -axis shows the total well depth. *Coloured dots* represent wells for which a CFC-12 measurement is available and the colour is scaled by the value of CFC-12 as shown on the scale bar. Where more than one CFC-12 measurement were available, an average was used. *Grey dots* show wells for which no CFC data are available. *Teal dotted lines* show the approximate location of inferred barriers, note that their Easting depends on the Northing value of the cross section, which is not shown, so barriers are indicated to just penetrate the upper part of the aquifer for an approximate guide. The number next to each circle represents the sample's Well Reference number.

CFC-12 when compared to samples further upstream of the Western Barriers at the same depth. When observing the value of the CFC-12 compared to the depth of the well screen below the water table (Figure A.14), it can be seen that there is no clear trend between the depth of the well screen below the water table and the value of CFC-12.

A.6 Stable isotopes

Stable isotopes data, including values for $\delta^{18}\text{O}$ and $\delta^2\text{H}$ are available for 18 wells across the site (Table A.3).

The stable H and O isotope values are all within a close range of values representative of the general range observed in other studies of the Hamersley Basin (Dogramaci and Skrzypek 2015). Many are located close to the GMWL (i.e. WR 31, WR 26, WR 25, WR 32 and WR 18) although the others appear enriched in $\delta^{18}\text{O}$ compared to the GMWL (Figure A.15). The range of values is, however, narrow. A narrow range of negative stable isotope values has previously been interpreted to suggest relatively low evaporative losses prior to recharge (Skrzypek et al. 2013).

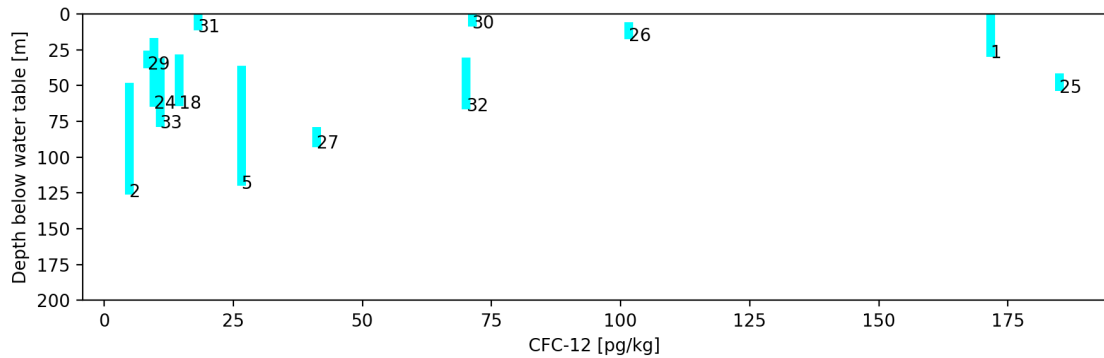


Figure A.14: Measured value of CFC-12 compared to the depth of the well screen below the water table are shown by the *blue lines*. Where more than one CFC-12 measurement were available, an average was used.

Site ID	WR	Sampling date	$\delta^{18}O$ [VS-MOW]	δ^2H [VS-MOW]
HDD0004	1	1/08/2019	-6.47	-42.6
LHRP1	2	20/07/2019	-8.07	-58.7
LHRP4	5	20/07/2019	-7.80	-57.1
LHRP7	6	21/07/2019	-7.69	-53.6
MB15HD1S002	17	4/08/2019	-8.45	-58.6
MB16H1SW0001	18	3/08/2019	-8.40	-59.4
MB17H1SW0001	20	3/08/2019	-8.70	-60.7
MB17H1SW0002	21	3/08/2019	-8.16	-59.8
MB17H1SW0018	24	3/08/2019	-7.98	-60.7
MB17H1SW0019	25	3/08/2019	-8.57	-59.5
MB17H1SW0020	26	3/08/2019	-8.53	-58.7
MB17H1SW0024	27	20/07/2019	-7.78	-57.0
MB17H1SW0026	28	22/07/2019	-7.92	-55.0
MB17H1SW0027	29	20/07/2019	-8.03	-59.6
MB17H1SW0029	30	3/08/2019	-8.09	-57.7
MB17H1SW0030	31	3/08/2019	-8.40	-57.7
MB17HD1S0001	32	20/07/2019	-8.50	-59.6
MB17HD1S0002	33	20/07/2019	-7.60	-57.1

Table A.3: Stable isotopes data for Baby Hope.

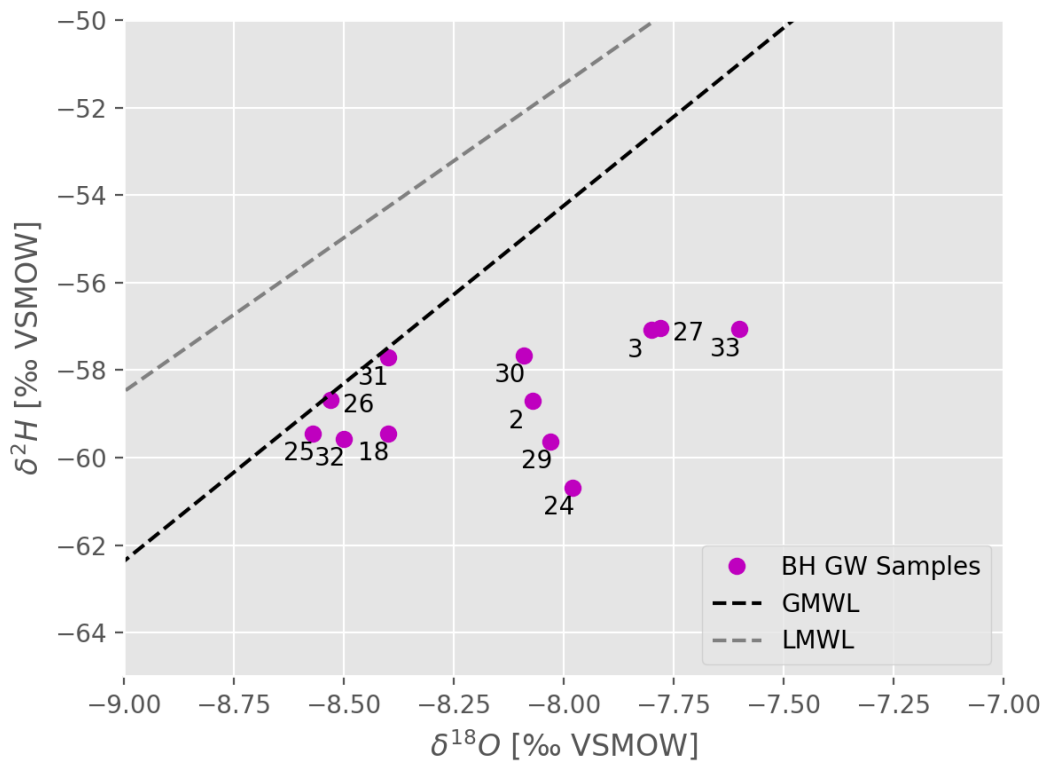


Figure A.15: Stable isotopes plot, where *purple dots* represent the value of $\delta^{18}\text{O}$ and $\delta^2\text{H}$ and are labelled with the WR number. Global Meteoric Water Line (GMWL) taken from Coplen et al. (2000), Local Meteoric Water Line (LMWL) taken from Dogramaci et al. (2012)

A.7 Summary

This appendix provides a summary of the available data and conceptual hydrogeological understanding of the Baby Hope site in the Pilbara region of Western Australia. This is a site that is intended for open-pit iron ore mining. The site includes four potential hydrogeological barriers, two in the east of the site and two in the west of the site. In the west of the site, the geology of the barriers is not known. It is not clear if these two barriers could in fact be a single low-permeability feature. In the east of the site, on the other hand, the barriers have been mapped and ground-truthed and are known to be dolerite dykes. In both the east and the west, steady-state hydraulic head data demonstrate that sharp decreases in head occur across the barriers. They appear to be buried by Tertiary sediment. However, the extent to which the western barriers, in particular, are buried is not clear.

Environmental tracer data was collected at this site to improve its hydrogeological understanding. There appear to be some unexplained, sharp changes in radiocarbon values and CFC values at a similar depth either side of the barriers. Interpreting this data is challenging, however, without full context of the recharge characteristics of the site and knowledge of how barriers impact groundwater flow. These open questions link well to Chapter 3 of the thesis in particular.

This appendix is not a full interpretation of the data at Baby Hope and does not provide a conclusion as to the nature and hydrogeological properties of the barriers. To achieve this, I suggest that numerical modelling of the Baby Site would be a natural extension to the project.

Recommended future work includes developing a numerical model of the site and reconstructing hydraulic head and groundwater age data. Groundwater age itself could be modelled, such as by using a direct age simulation (as per Chapters 3 and 4 in the thesis), or the concentration of environmental tracers could be explicitly simulated. Different hydrogeological properties of the inferred barriers could be compared to the field data collected. This may include model inversion, such as using PEST, where the geometric properties (i.e. the physical location) of the barriers are held constant while their hydrogeological properties (i.e. K values) are estimated. Further still, it could include model inversion where both the geometric properties and the hydrogeological properties are estimated, such as using the phantom structures technique demonstrated in Chapter 4 of this thesis.

Site ID	Well Reference (WR)		Easting [mE]	Northing [mN]	Elevation [mRL]	Casing		Well		Water Level [mRL]
						Diameter [mm]	Screen [mBGL]	Depth [mBGL]	Level	
HDD0004	1		723,555	7,451,700	608	50	9-57	57	578	
LHRP1	2		708,673	7,452,097	653	195	110-182	182	594	
LHRP13	3		699,491	7,452,122	689	200	60-120	120	627.1	
LHRP3	4		699,271	7,451,565	691	195	112-176	176	627.1	
LHRP4	5		715,630	7,452,508	621	195	67-145	145	593.8	
LHRP7	6		719,794	7,453,665	611	150	57-87	87	574.8	
MB13H1SW001	7		709,861	7,452,739	644	82	70-82	82	594.5	
MB13H1SW002	8		708,812	7,452,937	657	50	71-83	100	599.7	
MB13H1SW003	9		713,959	7,453,191	644	50	73-85	88	593.4	
MB14H1SW001	10		712,910	7,453,038	648	50	138-150	160	594.1	
MB14H1SW002	11		712,008	7,452,941	638	50	96-120	160	594.4	
MB14H1SW003	12		707,762	7,453,137	667	50	72-96	96	619.3	
MB15H1SW0001	13		708,813	7,452,541	646	100	18-100	100	595.7	
MB15H1SW0002	14		711,862	7,452,741	637	50	18-142	142	594.1	
MB15H1SW0003	15		712,461	7,452,842	636	50	18-124	124	594	
MB15H1SW0004	16		712,961	7,452,688	634	50	18-178	178	594	
MB15HD1S002	17		716,382	7,453,849	637	50	87-117	124	559.7*	
MB16H1SW0001	18		706,837	7,452,815	659	50	70-100	100	620.9	
MB16H1SW0002	19		711,411	7,453,630	717	154	124-154	154	614.4	
MB17H1SW0001	20		708,795	7,452,801	660	50	76-120	149	602.3*	
MB17H1SW0002	21		709,203	7,452,776	649	50	60-78	78	597.8*	
MB17H1SW0010	22		711,778	7,453,021	645	50	60-90	90	594.1*	
MB17H1SW0011	23		713,732	7,453,048	647	100	46-70	75	594.0*	
MB17H1SW0018	24		708,488	7,452,900	655	100	60-102	104	615	
MB17H1SW0019	25		710,727	7,452,176	640	100	90-96	96	595	
MB17H1SW0020	26		710,709	7,452,176	640	100	54-60	60	595	
MB17H1SW0024	27		716,964	7,453,063	617	100	108-116	122	591	
MB17H1SW0026	28		706,877	7,451,907	657	100	72-78	80	619.1*	
MB17H1SW0027	29		708,046	7,452,381	650	100	66-72	72	613	
MB17H1SW0029	30		708,058	7,452,397	650	100	37-43	43	613	

Table A.4: Well details for Baby Hope site, table 1 of 2.

Site ID	Well Reference (WR)		Easting [mE]	Northing [mN]	Elevation [mRL]	Casing		Well		Water Level [mRL]
						Diameter [mm]		Screen [mBGL]	Depth [mBGL]	
MB17H1SW0030	31		712,948	7,452,315	632	100		41-47	46.5	594
MB17HD1S0001	32		715,770	7,453,645	637	100		80-110	110	591
MB17HD1S0002	33		715,490	7,453,193	627	100		67-109	109	594
PZ07HD1S001	34		716,481	7,455,509	619	-		38-101	104	573
PZ07HD1S002	35		715,864	7,455,101	635	-		-	-	573
PZ07HD1S003	36		717,076	7,455,217	610	-		-	-	573
PZ07HD1S004	37		717,093	7,455,075	610	-		-	-	573
PZ07HD1S007	38		715,886	7,455,445	627	-		-	-	573
PZ07HD1S008	39		713,723	7,456,378	663	50		106-148	148	574
PZ07HD1S009	40		714,016	7,456,524	652	50		104-122	122	574
PZ07HD1S010	41		716,790	7,454,020	618	102		54-102	105	574
PZ07HD1S011	42		716,440	7,454,172	627	-		72-102	102	574
WB07HD1S001	43		717,089	7,455,201	610	254		65-67	140	573
WB07HD1S003	44		716,787	7,454,022	619	102		89-102	112	581
WB07HD1S004	45		716,476	7,455,170	620	203		47-107	124	573
WB10HD1S001	46		716,896	7,455,332	613	285		63-147	149	-
WB10HD1S002	47		716,744	7,455,391	615	-		-	165	-
WB16BHT0001	48		714,905	7,451,345	638	254		102-150	157	591
WB18H1SW0002	49		710,675	7,452,962	653	300		82-170	170	594.9*

Table A.5: Well details for Baby Hope site, table 2 of 2.

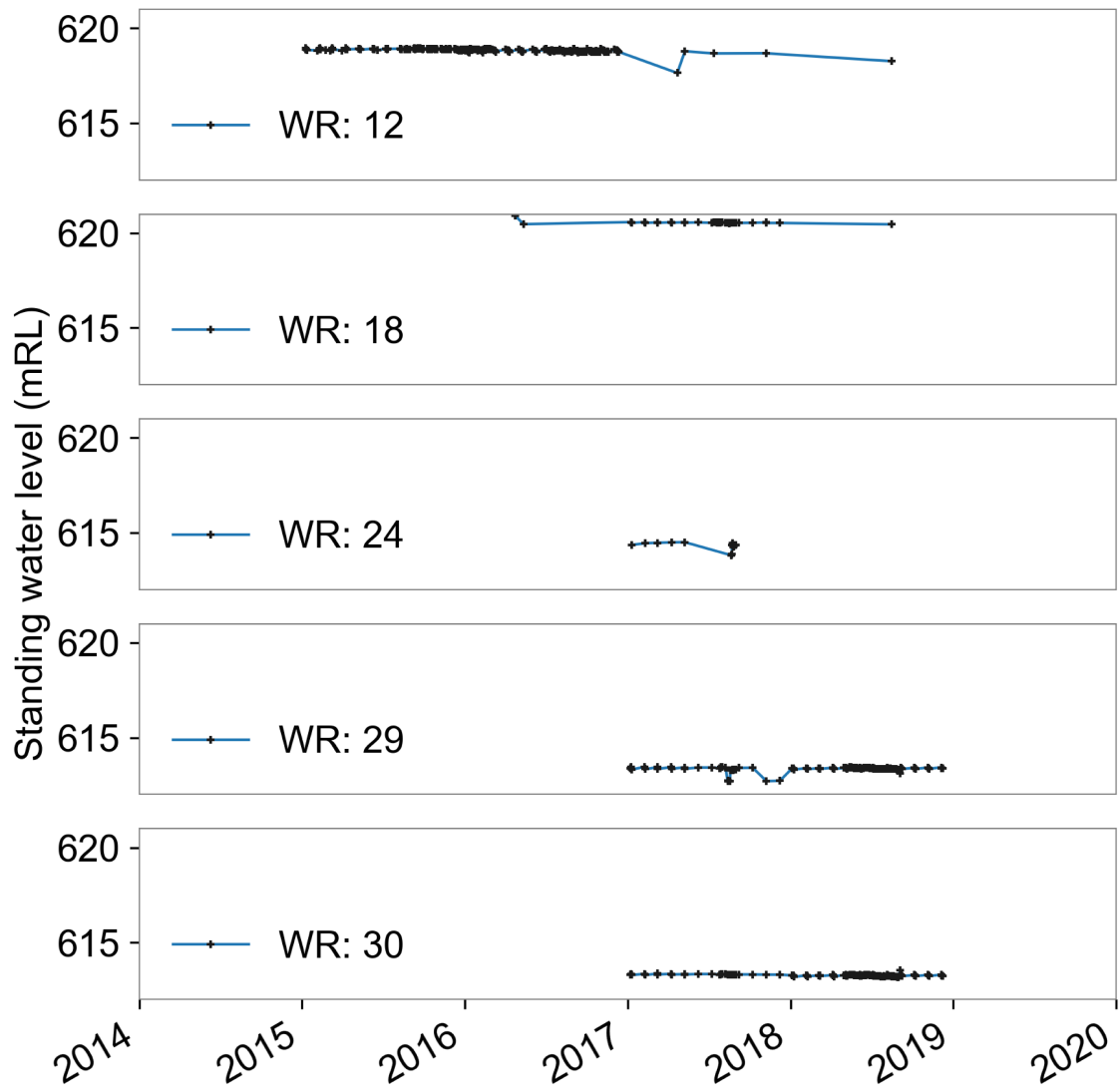


Figure A.16: Available transient water level data from the western side of the Western Barriers. WR = 'Well Reference'. *Black crosses* show data points, *blue lines* show interpolated trends.

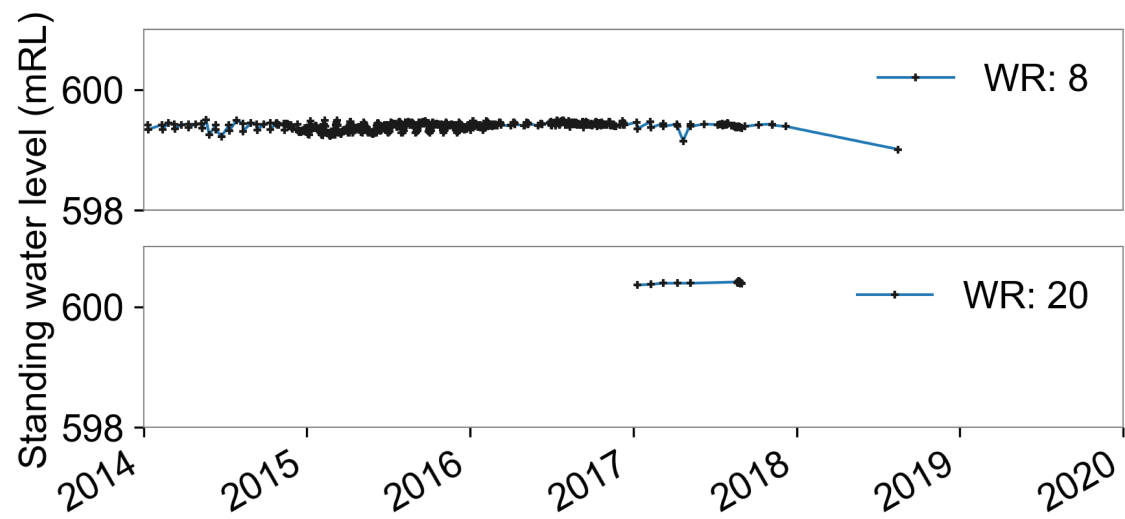


Figure A.17: Available transient water level data from the area between the two inferred Western Barriers. WR = 'Well Reference'. *Black crosses* show data points, *blue lines* show interpolated trends.

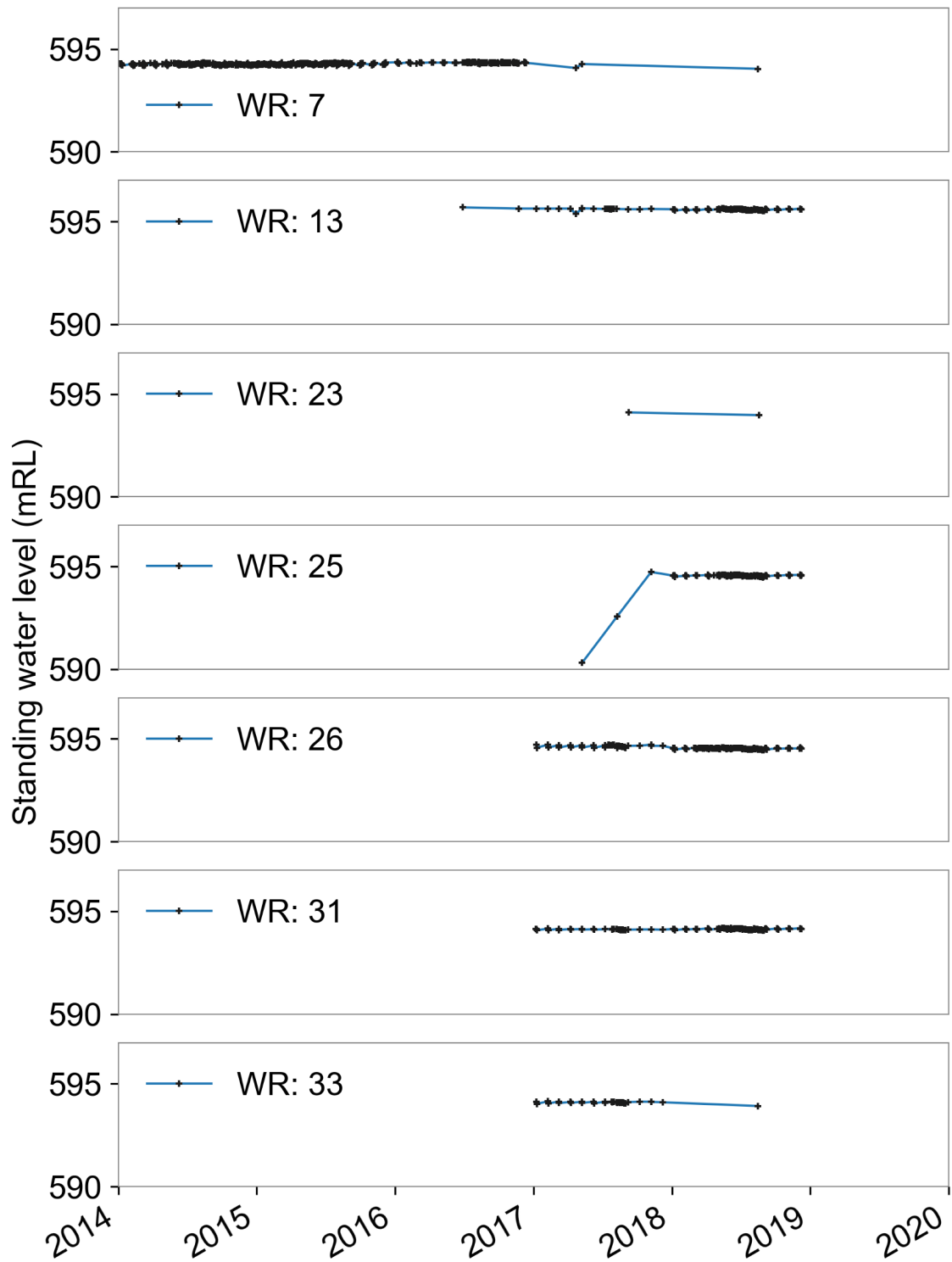


Figure A.18: Available transient water level data from the area between the Western Barriers and Eastern Barriers, A. WR = 'Well Reference'. *Black crosses* show data points, *blue lines* show interpolated trends.

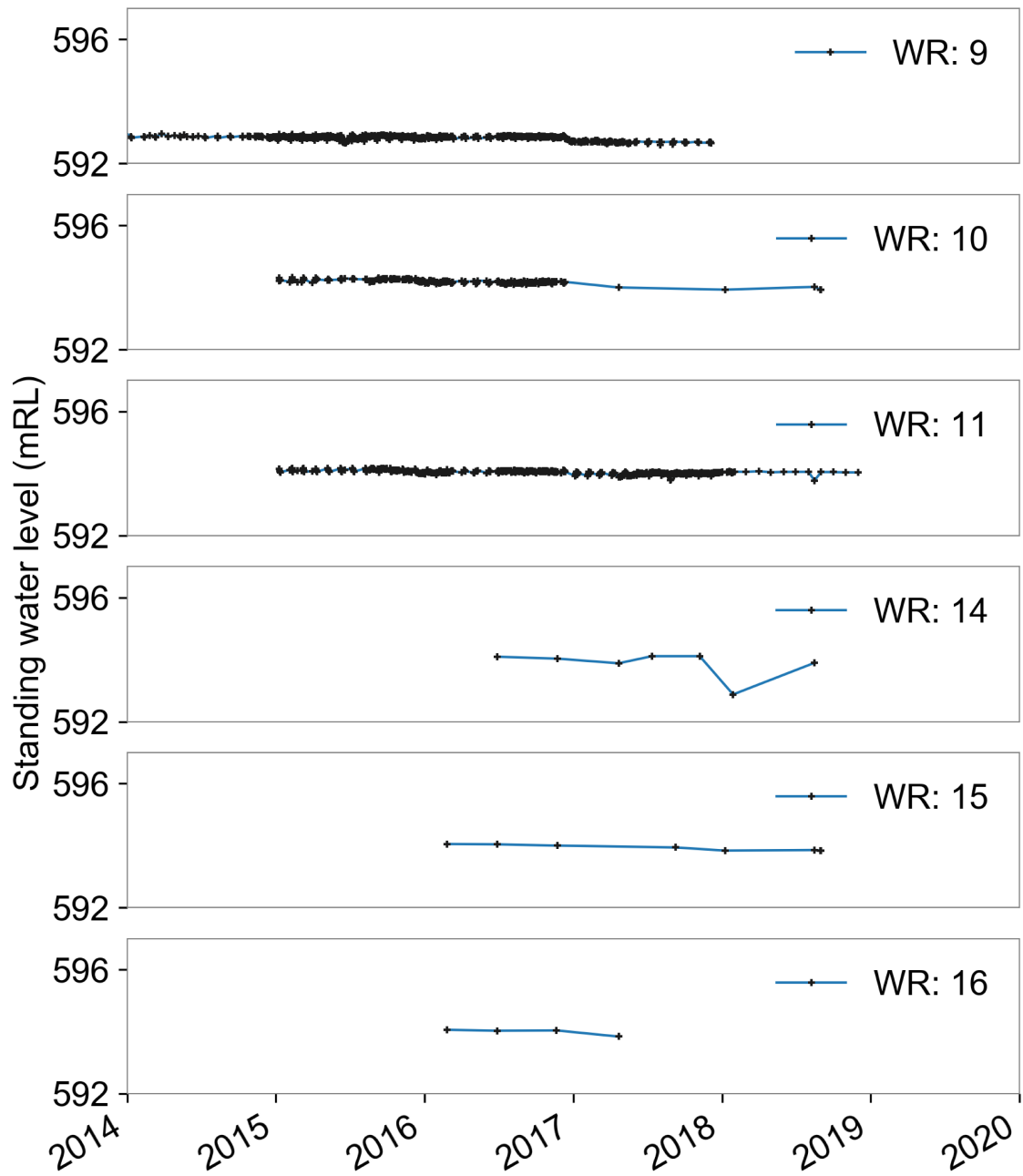


Figure A.19: Available transient water level data from the area between the Western Barriers and Eastern Barriers, B. WR = 'Well Reference'. *Black crosses* show data points, *blue lines* show interpolated trends.

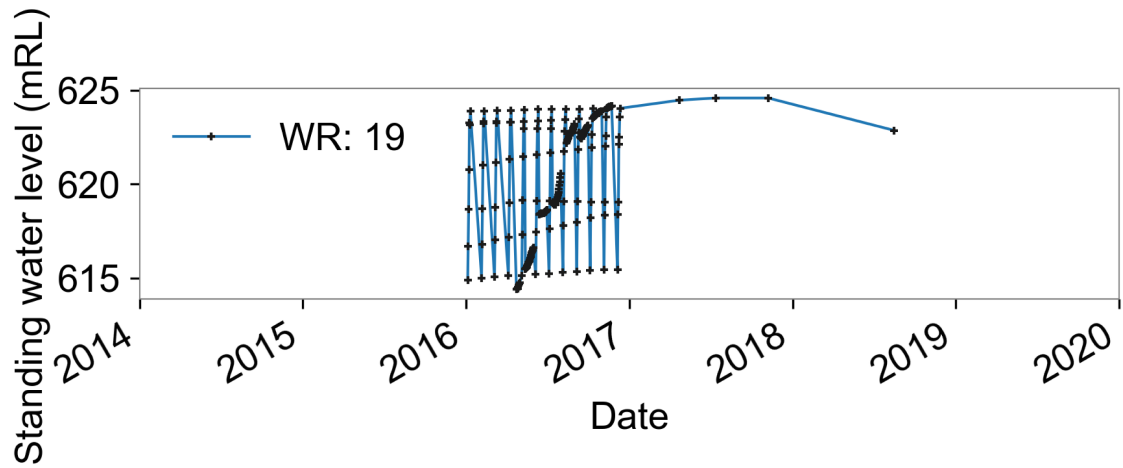


Figure A.20: Available transient water level data from well MB16H1SW0002, located in the area between the Western Barriers and Eastern Barriers. WR = ‘Well Reference’. *Black crosses* show data points, *blue lines* show interpolated trends.

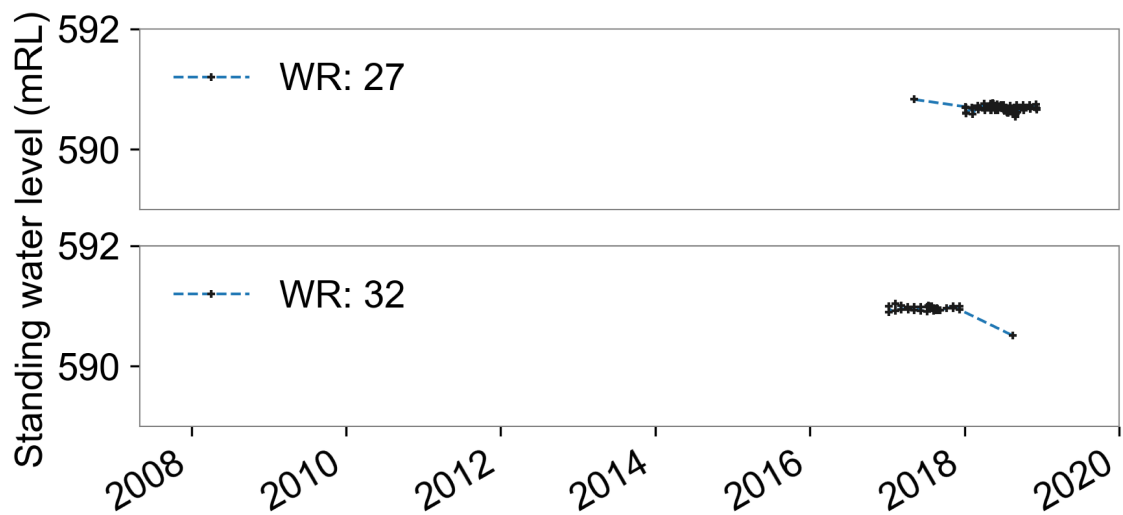


Figure A.21: Available transient water level data from the area between the two inferred Eastern Barriers. WR = ‘Well Reference’. *Black crosses* show data points, *blue lines* show interpolated trends.

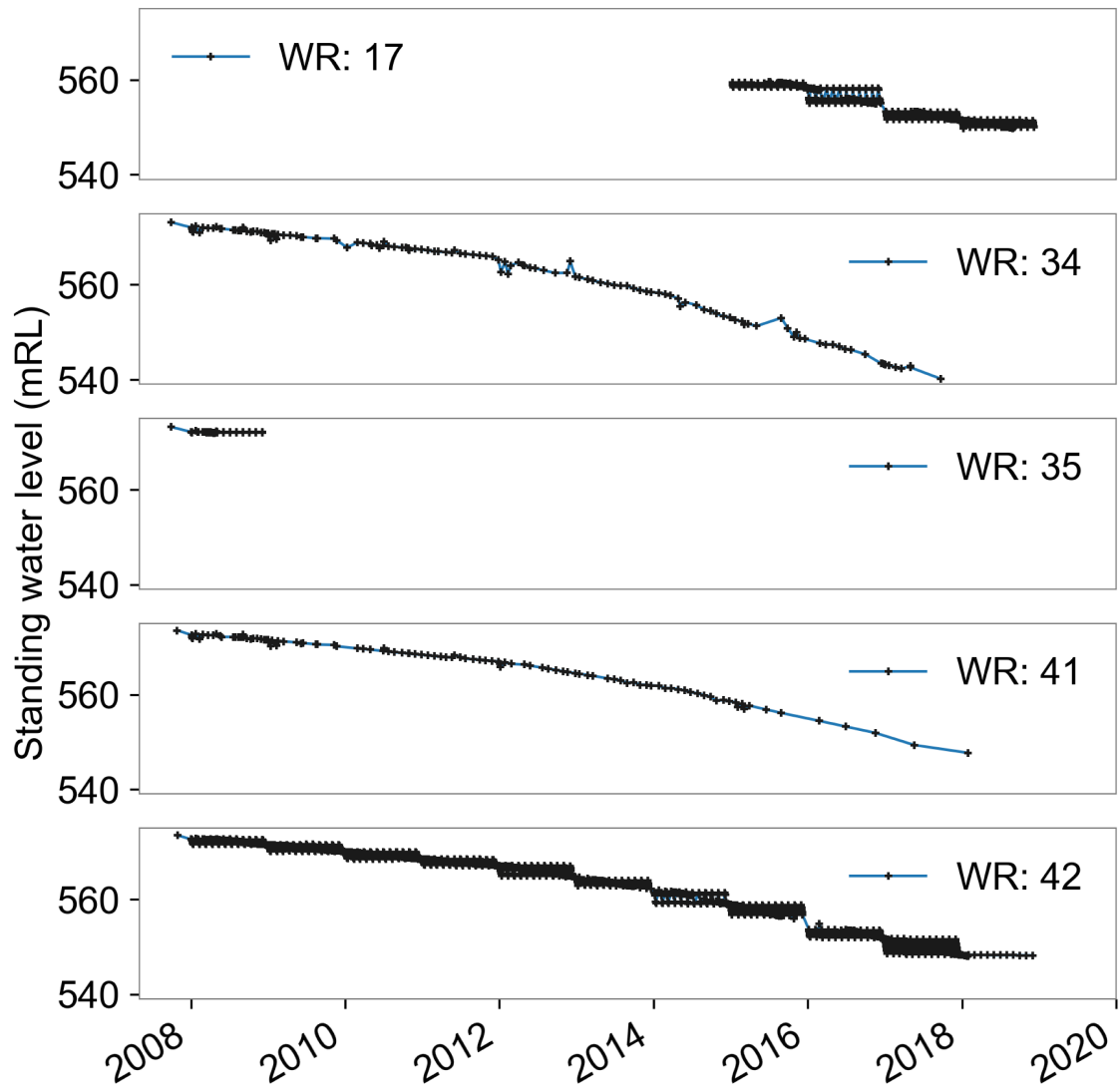


Figure A.22: Available transient water level data from the area to the east of the Eastern Barriers, A. WR = 'Well Reference'. *Black crosses* show data points, *blue lines* show interpolated trends.

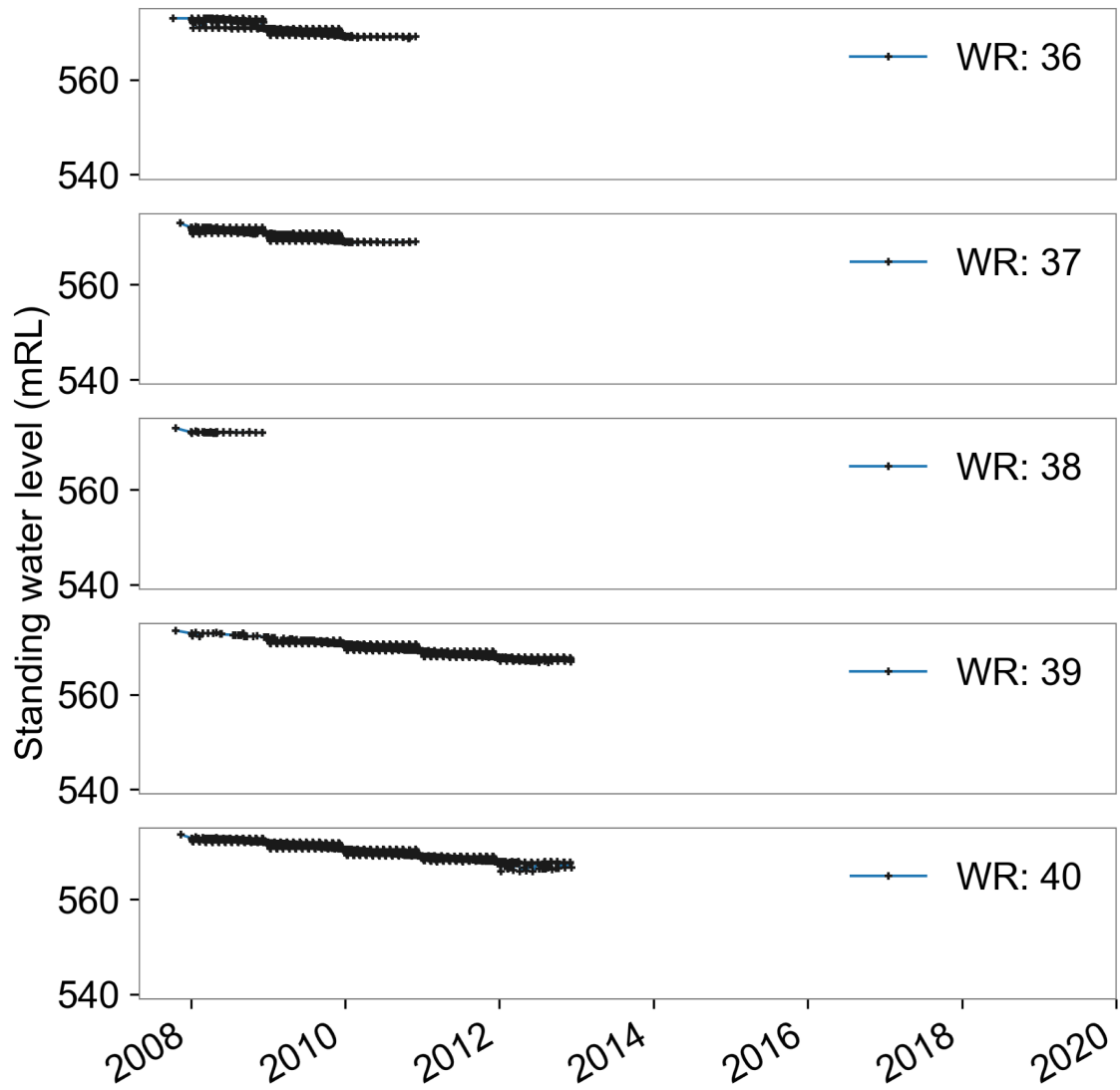


Figure A.23: Available transient water level data from the area to the east of the Eastern Barriers, B. WR = 'Well Reference'. *Black crosses* show data points, *blue lines* show interpolated trends.

Appendix B

Conference abstracts

B.1 Modelling the effect of undetected barriers on groundwater drawdown and recovery

Sarah K. Marshall; Peter G. Cook; Anthony D. Miller; Craig T. Simmons; Shawan Dogramaci

Abstract for presentation at the Geological Society of America Annual Meeting, 4–7 November, Indianapolis 2018

In the Pilbara region of Australia, large, open-pit iron-ore mines require high rates of dewatering. Predictions of drawdown are required both during mining and after it has ceased (groundwater recovery). The hydrogeology of the region is complex, with aquifers dissected by extensive dolerite dykes. Sharp hydraulic head gradients and pumping tests across these dykes demonstrate that many are impermeable barriers and inhibit groundwater flow. However, dykes may exist in areas that have not yet been affected by mine dewatering. These are therefore unlikely to have been detected and act as a source of structural uncertainty in models predicting groundwater drawdown and recovery.

This paper develops non-dimensional solutions to analytical models of groundwater flow to a well, utilising the methods of images. It explores conditions under which impermeable barriers may be undetected during groundwater pumping, yet still control the recovery of groundwater levels. The results show that even if a barrier is undetected during pumping, drawdown during recovery could be significantly greater than if that barrier were not present (on the pumping side of the barrier). The results are exemplified for a hypothetical aquifer with an unknown barrier 3 km from a pumping well. During ten years of pumping, the presence of the barrier increases drawdown by < 1 m adjacent to the barrier. However, 40

years after pumping has ceased, the presence of the barrier causes approximately 50 m of additional drawdown. The results have implications for the development of regional-scale models in areas affected by impermeable barriers.

B.2 Conjoint use of hydraulic head and groundwater age data to detect hydrogeologic barriers

Sarah K. Marshall; Peter G. Cook; Leonard F. Konikow; Craig T. Simmons; Shawan Dogramaci

Abstract for presentation at the Australasian Groundwater Conference, 24–27 November, Brisbane 2019

Hydraulic head and groundwater age data are effective in building groundwater system understanding. Yet their role in detecting and characterising near-vertical low-permeability geological structures—hydrogeologic barriers, such as faults and dykes—has not been widely studied. Here, numerical flow and transport models, using MODFLOW-NWT and MT3D-USGS, were developed with different hydrogeologic barrier configurations. Computed hydraulic head and groundwater age distributions were compared to those without a barrier. The joint use of these datasets helps in detecting vertically-oriented hydrogeologic barriers for a range of hydrogeologic conditions. Two forms of recharge were compared: (1) applied across the whole aquifer (uniform); or (2) applied only to its upstream part (upgradient).

The hydraulic head distribution is significantly impacted by a barrier (with gaps) that penetrates the aquifer’s full vertical thickness. This barrier type also perturbs the groundwater age distribution when upgradient recharge prevails. However, with uniform recharge, groundwater age is not successful in indicating the barrier’s presence. When a barrier is buried, such as by younger sediment, hydraulic head data does not clearly identify the presence of a barrier. Groundwater age data could, on the other hand, prove to be useful if sampled at depth-specific intervals. These results are significant for the detection and characterisation of hydrogeologic barriers where they may play a significant role in the compartmentalisation of groundwater flow, spring dynamics, and drawdown and recovery associated with groundwater extraction.

Reference List

- Allen, D. M. and F. A. Michel (1999). Characterizing a Faulted Aquifer by Field Testing and Numerical Simulation. *Groundwater* 37.(5), pp. 718–728. DOI: 10.1111/j.1745-6584.1999.tb01164.x.
- Anderson, E. I. and M. Bakker (2008). Groundwater flow through anisotropic fault zones in multiaquifer systems. *Water Resources Research* 44.(11), pp. 1–11. DOI: 10.1029/2008WR006925.
- Anderson, E. I. (2006). Analytical solutions for flow to a well through a fault. *Advances in Water Resources* 29.(12), pp. 1790–1803. DOI: 10.1016/j.jhydrol.2004.04.018.
- Apaydin, A. (2010). Relation of tectonic structure to groundwater flow in the Bepazari region, NW Anatolia, Turkey. *Hydrogeology Journal* 18.(6), pp. 1343–1356. DOI: 10.1007/s10040-010-0605-1.
- Australian Bureau of Statistics (2020). *Water Account, Australia*. URL: <https://www.abs.gov.au/statistics/environment/environmental-management/water-account-australia/latest-release>.
- Babiker, M. and A. Gudmundsson (2004). The effects of dykes and faults on groundwater flow in an arid land: the Red Sea Hills, Sudan. *Journal of Hydrology* 297.(1-4), pp. 256–273. DOI: 10.1016/j.jhydrol.2004.04.018.
- Bakker, M., V. Post, C. D. Langevin, J. D. Hughes, J. T. White, J. J. Starn, and M. N. Fienen (2016). Scripting MODFLOW Model Development Using Python and FloPy. *Groundwater* 54.(5), pp. 733–739. DOI: 10.1111/gwat.12413.
- Ball, L. B., S. Ge, J. S. Caine, A. Revil, and A. Jardani (2010). Constraining fault-zone hydrogeology through integrated hydrological and geoelectrical analysis. *Hydrogeology Journal* 18.(5), pp. 1057–1067. DOI: 10.1007/s10040-010-0587-z.
- Battle-Aguilar, J., E. W. Banks, O. Batelaan, R. Kipfer, M. S. Brennwald, and P. G. Cook (2017). Groundwater residence time and aquifer recharge in multilayered, semi-confined and faulted aquifer systems using environmental tracers. *Journal of Hydrology* 546, pp. 150–165. DOI: 10.1016/j.jhydrol.2016.12.036.
- Bedekar, V., E. D. Morway, C. D. Langevin, and M. Tonkin (2016). *MT3D-USGS version 1: A U.S. Geological Survey release of MT3DMS updated with new and*

- expanded transport capabilities for use with MODFLOW*. Techniques and Methods 6–A53. Reston, VA: United States Geological Survey, p. 69. DOI: 0.3133/tm6A53.
- Bense, V. F., T. Gleeson, S. E. Loveless, O. Bour, and J. Scibek (2013). Fault zone hydrogeology. *Earth-Science Reviews* 127, pp. 171–192. DOI: 10.1016/j.earscirev.2013.09.008.
- Bense, V. F. and H. Kooi (2004). Temporal and spatial variations of shallow subsurface temperature as a record of lateral variations in groundwater flow. *Journal of Geophysical Research: Solid Earth* 109.(B4), pp. 1–13. DOI: 10.1029/2003JB002782.
- Bense, V. F. and M. A. Person (2006). Faults as conduit-barrier systems to fluid flow in siliciclastic sedimentary aquifers. *Water Resources Research* 42.(5), pp. 1–18. DOI: 10.1029/2005WR004480.
- Bense, V. F. and R. T. Van Balen (2004). The effect of fault relay and clay smearing on groundwater flow patterns in the Lower Rhine Embayment. *Basin Research* 16.(3), pp. 397–411. DOI: 10.1111/j.1365-2117.2004.00238.x.
- Bense, V. F., R. T. Van Balen, and J. J. De Vries (2003). The impact of faults on the hydrogeological conditions in the Roer Valley Rift System: an overview. *Netherlands Journal of Geosciences* 82.(1), pp. 41–54. DOI: 10.1017/S0016774600022782.
- Beven, K. (2005). On the concept of model structural error. *Water Science and Technology* 52.(6), pp. 167–175. DOI: 10.2166/wst.2005.0165.
- Bredehoeft, J. D. (2005). The conceptualization model problem—surprise. *Hydrogeology Journal* 13.(1), pp. 37–46. DOI: 10.1007/s10040-004-0430-5.
- Bredehoeft, J. D. (2011). Monitoring Regional Groundwater Extraction: The Problem. *Groundwater* 49.(6), pp. 808–814. DOI: 10.1111/j.1745-6584.2011.00799.x.
- Bredehoeft, J. D., K. Belitz, and S. Sharp-Hansen (1992). The Hydrodynamics of the Big Horn Basin: A Study of the Role of Faults. *AAPG Bulletin* 76.(4), pp. 530–546. DOI: 10.1306/BDF8862-1718-11D7-8645000102C1865D.
- Bureau of Meteorology (2020). *Climate Data Online*. URL: <http://www.bom.gov.au/climate/data/> (visited on 10/10/2020).
- Caine, J. S., J. P. Evans, and C. B. Forster (1996). Fault zone architecture and permeability structure. *Geology* 24.(11), pp. 1025–1028. DOI: 10.1130/0091-7613.
- Carrera, J. and S. P. Neuman (1986). Estimation of Aquifer Parameters Under Transient and Steady State Conditions: 1. Maximum Likelihood Method Incorporating Prior Information. *Water Resources Research* 22.(2), pp. 199–210. DOI: 10.1029/WR022i002p00199.
- Castro, M. C. and P. Goblet (2005). Calculation of ground water ages—A comparative analysis. *Groundwater* 43.(3), pp. 368–380. DOI: 10.1111/j.1745-6584.2005.0046.x.

- Chen, J. and Y. Rubin (2003). An effective Bayesian model for lithofacies estimation using geophysical data. *Water Resources Research* 39.(5), pp. 4.1–4.11. DOI: 10.1029/2002WR001666.
- Cilona, A., A. Aydin, and N. M. Johnson (2015). Permeability of a fault zone cross-cutting a sequence of sandstones and shales and its influence on hydraulic head distribution in the Chatsworth Formation, California, USA. *Hydrogeology Journal* 23.(2), pp. 405–419. DOI: 10.1007/s10040-014-1206-1.
- Commander, P., R. Rojas, G. Hodgson, and D. McFarlane (2015). Groundwater. *Pilbara Water Resource Assessment. A report to the Government of Western Australia and industry partners from the CSIRO Pilbara Water Resource Assessment*. Ed. by D. J. MacFarlane. Australia: CSIRO Land and Water. ISBN: 978-1-4863-0545-2.
- Comte, J.-C., C. Wilson, U. Ofterdinger, and A. González-Quirós (2017). Effect of volcanic dykes on coastal groundwater flow and saltwater intrusion: A field-scale multiphysics approach and parameter evaluation. *Water Resources Research* 53.(3), pp. 2171–2198. DOI: 10.1002/2016WR019480.
- Cook, P. G. and D. K. Solomon (1997). Recent advances in dating young groundwater: chlorofluorocarbons, $^3\text{H}/^3\text{He}$ and ^{85}Kr . *Journal of Hydrology* 191.(1-4), pp. 245–265. DOI: 10.1016/S0022-1694(96)03051-X.
- Cook, P., S. Dogramaci, J. McCallum, and J. Hedley (2016). Groundwater age, mixing and flow rates in the vicinity of large open pit mines, Pilbara region, northwestern Australia. *Hydrogeology Journal* 25.(1), pp. 39–53. DOI: 10.1007/s10040-016-1467-y.
- Cook, P. G. and J.-K. Böhlke (2000). Determining Timescales for Groundwater Flow and Solute Transport. *Environmental Tracers in Subsurface Hydrology*. Ed. by P. G. Cook and A. L. Herczeg. Boston, MA: Springer. DOI: 10.1007/978-1-4615-4557-6_1.
- Cook, P. G., S. L. Noorduijn, G. Kirkpatrick, and S. Dogramaci (2020). *Changes in the groundwater balance of an arid region following mining development, Unpublished Report*. Report.
- Coplen, T. B., A. L. Herczeg, and C. Barnes (2000). Isotope Engineering — Using Stable Isotopes of the Water Molecule to Solve Practical Problems. *Environmental Tracers in Subsurface Hydrology*. Ed. by P. G. Cook and A. L. Herczeg. Boston, MA: Springer. DOI: 10.1007/978-1-4615-4557-6_1.
- Currell, M. J., A. D. Werner, C. McGrath, J. A. Webb, and M. Berkman (2017). Problems with the application of hydrogeological science to regulation of Australian mining projects: Carmichael Mine and Doongmabulla Springs. *Journal of Hydrology* 548, pp. 674–682. DOI: 10.1016/j.jhydrol.2017.03.031.

- Dai, Z., E. Keating, C. Gable, D. Levitt, J. Heikoop, and A. Simmons (2010). Step-wise inversion of a groundwater flow model with multi-scale observation data. *Hydrogeology Journal* 18.(3), pp. 607–624. DOI: 10.1007/s10040-009-0543-y.
- Dogramaci, S. and W. Dodson (2009). The Use of Stable Isotopes of Oxygen, Hydrogen and Carbon to Understand Groundwater Dynamics in the Hammersley Basin, Western Pilbara Region, Northwest Australia. *Water in Mining Conference*.
- Dogramaci, S., G. Firmani, P. Hedley, G. Skrzypek, and P. F. Grierson (2015). Evaluating recharge to an ephemeral dryland stream using a hydraulic model and water, chloride and isotope mass balance. *Journal of Hydrology* 521, pp. 520–532. DOI: 10.1016/j.jhydrol.2014.12.017.
- Dogramaci, S. and G. Skrzypek (2015). Unravelling sources of solutes in groundwater of an ancient landscape in NW Australia using stable Sr, H and O isotopes. *Chemical Geology* 393-394, pp. 67–78. DOI: 10.1016/j.chemgeo.2014.11.021.
- Dogramaci, S., G. Skrzypek, W. Dodson, and P. F. Grierson (2012). Stable isotope and hydrochemical evolution of groundwater in the semi-arid Hamersley Basin of subtropical northwest Australia. *Journal of Hydrology* 475, pp. 281–293. DOI: 10.1016/j.jhydrol.2012.10.004.
- Doherty, J. (2003). Ground Water Model Calibration Using Pilot Points and Regularization. *Groundwater* 41.(2), pp. 170–177. DOI: 10.1111/j.1745-6584.2003.tb02580.x.
- Doherty, J. and R. J. Hunt (2009). Two statistics for evaluating parameter identifiability and error reduction. *Journal of Hydrology* 366.(1-4), pp. 119–127. DOI: 10.1016/j.jhydrol.2008.12.018.
- Doherty, J. and C. T. Simmons (2013). Groundwater modelling in decision support: reflections on a unified conceptual framework. *Hydrogeology Journal* 21.(7), pp. 1531–1537. DOI: 10.1007/s10040-013-1027-7.
- Doherty, J. and D. Welter (2010). A short exploration of structural noise. *Water Resources Research* 46.(5), pp. 1–14. DOI: 10.1029/2009WR008377.
- Doherty, J. E. (2015). *Calibration and Uncertainty Analysis for Complex Environmental Models. PEST: complete theory and what it means for modelling the real world*. Brisbane, Australia: Watermark Numerical Computing. ISBN: 978-0-9943786-0-6.
- Doherty, J. E. (2018a). *Nonlinear Regularization in support of Geologically Realistic Parameter Fields*. Unpublished report. Brisbane, Australia: Watermark Numerical Computing.
- Doherty, J. E. (2018b). *PEST Model-Independent Parameter Estimation User Manual*. 7th Edition. Brisbane, Australia: Watermark Numerical Computing.

- Enemark, T., L. J. Peeters, D. Mallants, and O. Batelaan (2019). Hydrogeological conceptual model building and testing: A review. *Journal of Hydrology* 569, pp. 310–329. DOI: 10.1016/j.jhydrol.2018.12.007.
- Fairley, J. P. (2009). Modeling fluid flow in a heterogeneous, fault-controlled hydrothermal system. *Geofluids* 9.(2), pp. 153–166. DOI: 10.1111/j.1468-8123.2008.00236.x.
- Ferrill, D. A., D. W. Sims, D. J. Waiting, A. P. Morris, N. M. Franklin, and A. L. Schultz (2004). Structural framework of the Edwards Aquifer recharge zone in south-central Texas. *GSA Bulletin* 116.(3-4), pp. 407–418. DOI: 10.1130/B25174.1.
- Ferris, J. G., D. B. Knowles, R. H. Brown, and R. W. Stallman (1962). *Theory of aquifer tests*. Water-Supply Paper 1536-E. Denver, CO: United States Geological Survey, p. 105. DOI: 10.3133/wsp1536E.
- Fienen, M. N., C. T. Muffels, and R. J. Hunt (2009). On Constraining Pilot Point Calibration with Regularization in PEST. *Groundwater* 47.(6), pp. 835–844. DOI: 10.1111/j.1745-6584.2009.00579.x.
- Fitts, C. R. (1997). Analytic Modeling of Impermeable and Resistant Barriers. *Groundwater* 35.(2), pp. 312, 317. DOI: 10.1111/j.1745-6584.1997.tb00088.x.
- Gelhar, L. W., C. Welty, and K. R. Rehfeldt (1992). A critical review of data on field-scale dispersion in aquifers. *Water Resources Research* 28.(7), pp. 1955–1974. DOI: 10.1029/92wr00607.
- Gleeson, T. and K. Novakowski (2009). Identifying watershed-scale barriers to groundwater flow: Lineaments in the Canadian Shield. *GSA Bulletin* 121.(3-4), pp. 333–347. DOI: 10.1130/B26241.1.
- Goode, D. J. (1996). Direct Simulation of Groundwater Age. *Water Resources Research* 32.(2), pp. 289–296. DOI: 10.1029/95WR03401.
- Guillaume, J. H. A., R. J. Hunt, A. Comunian, R. S. Blakers, and B. Fu (2016). Methods for Exploring Uncertainty in Groundwater Management Predictions. *Integrated Groundwater Management*. Ed. by A. J. Jakeman, O. Barreteau, R. J. Hunt, J.-D. Rinaudo, and A. Ross. Springer, Cham, pp. 711–737. ISBN: 978-3-319-23575-2. DOI: 10.1007/978-3-319-23576-9.
- Gumm, L. P., V. F. Bense, P. F. Dennis, K. M. Hiscock, N. Cremer, and S. Simon (2016). Dissolved noble gases and stable isotopes as tracers of preferential fluid flow along faults in the Lower Rhine Embayment, Germany. *Hydrogeology Journal* 24.(1), pp. 99–108. DOI: 10.1007/s10040-015-1321-7.
- Gupta, H. V., M. P. Clark, J. A. Vrugt, G. Abramowitz, and M. Ye (2012). Towards a comprehensive assessment of model structural adequacy. *Water Resources Research* 48.(8), pp. 1–16. DOI: 10.1029/2011WR011044.

- Hadley, D. R., D. B. Abrams, and G. S. Roadcap (2020). Modeling a Large-Scale Historic Aquifer Test: Insight into the Hydrogeology of a Regional Fault Zone. *Groundwater* 58 (3), pp. 453–463. DOI: 10.1111/gwat.12922.
- Hamersley HMS Pty Ltd (2015). *Baby Hope Proposal, Environmental Review Document*. Report S38 Referral. Perth, Western Australia: Rio Tinto.
- Harp, D. R., Z. Dai, A. V. Wolfsberg, J. A. Vrugt, B. A. Robinson, and V. V. Vesselinov (2008). Aquifer structure identification using stochastic inversion. *Geophysical Research Letters* 35.(8), pp. 1–5. DOI: 10.1029/2008GL033585.
- Hill, M. C. and C. R. Tiedeman (2007). *Effective groundwater model calibration: With analysis of data, sensitivities, predictions, and uncertainty*. Hoboken, NJ: Wiley-Interscience, p. 480. ISBN: 9780471776369. DOI: 10.1002/9780470041086.index.
- Hope Downs Management Services Pty Ltd (2000). *Hope Downs Iron Ore Project Public Environmental Report/Public Environmental Review*. Report.
- Hsieh, P. A. and J. R. Freckleton (1993). *Documentation of a computer program to simulate horizontal-flow barriers using the U.S. Geological Survey’s modular three-dimensional finite-difference ground-water flow model*. Open-File Report 92-477. Reston, VA: United States Geological Survey, p. 32. DOI: 10.3133/ofr92477.
- Hunt, R. J. and D. E. Welter (2010). Taking Account of “Unknown Unknowns”. *Ground Water* 48.(4), pp. 477–477. ISSN: 1745-6584. DOI: 10.1111/j.1745-6584.2010.00681.x.
- Janos, D., J. Molson, and R. Lefebvre (2018). Regional groundwater flow dynamics and residence times in Chaudière-Appalaches, Québec, Canada: Insights from numerical simulations. *Canadian Water Resources Journal / Revue canadienne des ressources hydriques* 43.(2), pp. 214–239. DOI: 10.1080/07011784.2018.1437370.
- Johnson, S. L. (2004). Geology and hydrogeology. *An inventory and condition survey of the Pilbara region, Western Australia*. Ed. by A. M. van Vreeswyk, K. A. Leighton, A. L. Payne, and P. Hennig. Vol. Technical Bulletin 92. Perth, Western Australia: Department of Agriculture and Food. ISBN: 0-646-44349-6.
- Kellogg Brown Root (2008). *Hope Downs 1 Stage 1 (2008), Review of Dewatering Progress Hope Downs North*. Kellogg, Brown and Root Pty Ltd.
- Knowling, M. J., J. T. White, C. R. Moore, P. Rakowski, and K. Hayley (2020). On the assimilation of environmental tracer observations for model-based decision support. *Hydrology and Earth System Sciences* 24.(4), pp. 1677–1689. DOI: 10.5194/hess-24-1677-2020.
- Konikow, L. F., G. Z. Hornberger, L. D. Putnam, A. M. Shapiro, and B. A. Zinn (2008). The use of groundwater age as a calibration target. *International Conference on Calibration and Reliability in Groundwater Modeling: Credibility of*

- Modeling* (Copenhagen). Ed. by J. C. Refsgaard, K. Kovar, E. Haarder, and E. Nygaard. Vol. 320. IAHS Publication, pp. 250–256.
- Koohbor, B., M. Fahs, B. Ataie-Ashtiani, B. Belfort, C. T. Simmons, and A. Younes (2019). Uncertainty analysis for seawater intrusion in fractured coastal aquifers: Effects of fracture location, aperture, density and hydrodynamic parameters. *Journal of Hydrology* 571, pp. 159–177. DOI: 10.1016/j.jhydrol.2019.01.0.
- Kruseman, G. P. and N. A. de Ridder (2000). *Analysis and Evaluation of Pumping Test Data*. Second Edition (Completely Revised). Publication 47. Wageningen, The Netherlands: International Institute for Land Reclamation and Improvement. ISBN: 9070754207.
- Larocque, M., P. G. Cook, K. Haaken, and C. T. Simmons (2009). Estimating Flow Using Tracers and Hydraulics in Synthetic Heterogeneous Aquifers. *Groundwater* 47.(6), pp. 786–796. DOI: 10.1111/j.1745-6584.2009.00595.x.
- Latscha, A.-A. (2010). *Ophthalmia, West Angelas, Juna Downs Districts Hydrogeological Conceptual Model*. Rio Tinto.
- Manning, A. H. and D. K. Solomon (2003). Using noble gases to investigate mountain-front recharge. *Journal of Hydrology* 275.(3-4), pp. 194–207. DOI: 10.1016/S0022-1694(03)00043-X.
- Marler, J. and S. Ge (2003). The permeability of the Elkhorn Fault Zone, South Park, Colorado. *Groundwater* 41.(3), pp. 321–332. DOI: 10.1111/j.1745-6584.2003.tb02601.x.
- Marshall, S., P. G. Cook, L. F. Konikow, C. T. Simmons, and S. Dogramaci (2020). Conjoint use of hydraulic head and groundwater age data to detect hydrogeologic barriers. *Hydrogeology Journal* 28.(3), pp. 1003–1019. DOI: 10.1007/s10040-019-02095-9.
- Marshall, S. K., P. G. Cook, A. D. Miller, C. T. Simmons, and S. Dogramaci (2019). The Effect of Undetected Barriers on Groundwater Drawdown and Recovery. *Groundwater* 57.(5), pp. 718–726. DOI: 10.1111/gwat.12856.
- Mayer, A., W. May, C. Lukkarila, and J. Diehl (2007). Estimation of fault-zone conductance by calibration of a regional groundwater flow model: Desert Hot Springs, California. *Hydrogeology Journal* 15.(6), pp. 1093–1106. DOI: 10.1007/s10040-007-0158-0.
- McCallum, J. L., P. G. Cook, S. Dogramaci, R. Purtschert, C. T. Simmons, and L. Burk (2017). Identifying modern and historic recharge events from tracer-derived groundwater age distributions. *Water Resources Research* 53.(2), pp. 1039–1056. DOI: 10.1002/2016WR019839.
- McCallum, J. L., P. G. Cook, C. T. Simmons, and A. D. Werner (2014a). Bias of Apparent Tracer Ages in Heterogeneous Environments. *Groundwater* 52.(2), pp. 239–250. DOI: 10.1111/gwat.12052.

- McCallum, J. L., D. Herckenrath, and C. T. Simmons (2014b). Impact of Data Density and Geostatistical Simulation Technique on the Estimation of Residence Times in a Synthetic Two-dimensional Aquifer. *Mathematical Geosciences* 46.(5), pp. 539–560. DOI: 10.1007/s11004-013-9518-6.
- McFarlane, D. J. (2015). *Pilbara Water Resource Assessment. A report to the Government of Western Australia and industry partners from the CSIRO Pilbara Water Resource Assessment*. Australia: CSIRO Land and Water.
- McKenzie, N. L., S. v. Leeuwen, and A. M. Pinder (2009). Introduction to the Pilbara Biodiversity Survey, 2002–2007. *Records of the Western Australian Museum, Supplement 78*, pp. 3–89. DOI: 10.18195/issn.0313-122x.78(1).2009.003-089.
- Moore, C. and J. Doherty (2005). Role of the calibration process in reducing model predictive error. *Water Resources Research* 41.(5), pp. 1–14. DOI: 10.1029/2004wr003501.
- Morris, R. C. and R. C. Horwitz (1983). The origin of the iron-formation-rich Hamersley Group of Western Australia — deposition on a platform. *Precambrian Research* 21.(3), pp. 273–297. ISSN: 0301-9268. DOI: [https://doi.org/10.1016/0301-9268\(83\)90044-X](https://doi.org/10.1016/0301-9268(83)90044-X).
- Niswonger, R. G., S. Panday, and M. Ibaraki (2011). *MODFLOW-NWT, A Newton Formulation for MODFLOW-2005*. Techniques and Methods 6–A37. United States Geological Survey, p. 44. DOI: 10.3133/tm6A37.
- Ochoa-González, G. H., D. Carreón-Freyre, M. Cerca, and M. López-Martínez (2015). Assessment of groundwater flow in volcanic faulted areas. A study case in Queretaro, Mexico. *Geofísica Internacional* 54.(3), pp. 199–220. DOI: 10.1016/j.gi.2015.04.016.
- Oreskes, N. and K. Belitz (2001). Philosophical Issues in Model Assessment. *Model Validation: Perspectives in Hydrological Science*. Ed. by M. G. Anderson and P. D. Bates. Chichester, England: John Wiley and Sons, p. 512. ISBN: 978-0-471-98572-3.
- Parrod, A.-S. (2019). *Effect of faults and barriers on groundwater flow; Preliminary study at Baby Hope, HD1, Hamersley Basin*. Report. Rio Tinto.
- Per, S., T. B. Minor, and M. M. Chesley (1997). Ground-Water Exploration Based on Lineament Analysis and Reproducibility Tests. *Groundwater* 35.(5), pp. 888–894. DOI: 10.1111/j.1745-6584.1997.tb00157.x.
- Pereira, A. J. S. C., M. M. Godinho, and L. J. P. F. Neves (2010). On the influence of faulting on small-scale soil-gas radon variability: a case study in the Iberian Uranium Province. *Journal of Environmental Radioactivity* 101.(10), pp. 875–882. DOI: 10.1016/j.jenvrad.2010.05.014.
- Pham, L. (2016). *West Angelas Deposits C and D Regional Groundwater Model*. RTIO-PDE-0147252.

- Poulsen, D. L., P. G. Cook, C. T. Simmons, D. K. Solomon, and S. Dogramaci (2019). Depth-Resolved Groundwater Chemistry by Longitudinal Sampling of Ambient and Pumped Flows Within Long-Screened and Open Borehole Wells. *Water Resources Research* 55.(11), pp. 9417–9435. DOI: 10.1029/2019wr025713.
- Pujades, E., A. López, J. Carrera, E. Vázquez-Suñé, and A. Jurado (2012). Barrier effect of underground structures on aquifers. *Engineering Geology* 145-146, pp. 41–49. DOI: 10.1016/j.enggeo.2012.07.004.
- Raiber, M., J. A. Webb, D. I. Cendón, P. A. White, and G. E. Jacobsen (2015). Environmental isotopes meet 3D geological modelling: Conceptualising recharge and structurally-controlled aquifer connectivity in the basalt plains of south-western Victoria, Australia. *Journal of Hydrology* 527, pp. 262–280. DOI: 10.1016/j.jhydrol.2015.04.053.
- Rajabpour, H. and A. Vaezihir (2016). Hydrogeological Studies to Identify the Trend of Concealed Section of the North Tabriz Fault (Iran). *Groundwater* 55.(3), pp. 327–333. DOI: 10.1111/gwat.12477.
- Rapantova, N., A. Grmela, D. Vojtek, J. Halir, and B. Michalek (2007). Ground Water Flow Modelling Applications in Mining Hydrogeology. *Mine Water and the Environment* 26.(4), pp. 264–270. DOI: 10.1007/s10230-007-0017-1.
- Rawling, G. C., L. B. Goodwin, and J. L. Wilson (2001). Internal architecture, permeability structure, and hydrologic significance of contrasting fault-zone types. *Geology* 29.(1), pp. 43–46. DOI: 10.1130/0091-7613(2001)029(0043:IAPSAH)2.0.CO;2.
- Refsgaard, J. C., S. Christensen, T. O. Sonnenborg, D. Seifert, A. L. Højberg, and L. Trolborg (2012). Review of strategies for handling geological uncertainty in groundwater flow and transport modeling. *Advances in Water Resources* 36, pp. 36–50. DOI: 10.1016/j.advwatres.2011.04.006.
- Reilly, T. E., L. N. Plummer, P. J. Phillips, and E. Busenberg (1994). The use of simulation and multiple environmental tracers to quantify groundwater flow in a shallow aquifer. *Water Resources Research* 30.(2), pp. 421–433. DOI: 10.1029/93WR02655.
- Rojas, R., P. Commander, D. McFarlane, R. Ali, W. Dawes, O. Barron, G. Hodgson, and S. Charles (2018). Groundwater Resource Assessment and Conceptualization in the Pilbara Region, Western Australia. *Earth Systems and Environment* 2, pp. 345–365. DOI: 10.1007/s41748-018-0051-0.
- Rouillard, A., G. Skrzypek, C. Turney, S. Dogramaci, Q. Hua, A. Zawadzki, J. Reeves, P. Greenwood, A. J. O'Donnell, and P. F. Grierson (2016). Evidence for extreme floods in arid subtropical northwest Australia during the Little Ice Age chronozone (CE 1400-1850). *Quaternary Science Reviews* 144, pp. 107–122.

- RPS Group (2015). *Ecohydrogeological Conceptualisation of the Central Pilbara Region*. Subiaco, Western Australia.
- Sanford, W. (2011). Calibration of models using groundwater age. *Hydrogeology Journal* 19.(1), pp. 13–16. DOI: 10.1007/s10040-010-0637-6.
- Schilling, O. S., P. G. Cook, and P. Brunner (2019). Beyond Classical Observations in Hydrogeology: The Advantages of Including Exchange Flux, Temperature, Tracer Concentration, Residence Time, and Soil Moisture Observations in Groundwater Model Calibration. *Reviews of Geophysics* 57.(1), pp. 146–182. DOI: 10.1029/2018rg000619.
- Seaton, W. J. and T. J. Burbey (2005). Influence of ancient thrust faults on the hydrogeology of the blue ridge province. *Groundwater* 43.(3), pp. 301–313. DOI: 10.1111/j.1745-6584.2005.0026.x.
- Sebben, M. L. and A. D. Werner (2016). On the effects of preferential or barrier flow features on solute plumes in permeable porous media. *Advances in Water Resources* 98, pp. 32–46. DOI: 10.1016/j.advwatres.2016.10.011.
- Senior, A., A. Britt, D. Summerfield, A. Hughes, A. Hitchman, A. Cross, D. Champion, D. Huston, E. Bastrakov, M. Sexton, J. Moloney, J. Pheeney, and A. Schofield (2020). *Australia's Identified Mineral Resources 2019*. Geoscience Australia, p. 78. DOI: 10.11636/1327-1466.2019.
- Singh, S. K. (2001). Identifying Impervious Boundary and Aquifer Parameters from Pump-Test Data. *Journal of Hydraulic Engineering* 127.(4), pp. 280–285. DOI: 10.1061/(ASCE)0733-9429(2001)127:4(280).
- Skrzypek, G., S. Dogramaci, and P. F. Grierson (2013). Geochemical and hydrological processes controlling groundwater salinity of a large inland wetland of northwest Australia. *Chemical Geology* 357, pp. 164–177. ISSN: 0009-2541. DOI: <https://doi.org/10.1016/j.chemgeo.2013.08.035>.
- Smerdon, B. D. and C. Turnadge (2015). Considering the potential effect of faulting on regional-scale groundwater flow: an illustrative example from Australia's Great Artesian Basin. *Hydrogeology Journal* 23.(5), pp. 949–960. DOI: 10.1007/s10040-015-1248-z.
- Stamatis, G. and K. Voudouris (2003). Marine and human activity influences on the groundwater quality of southern Korinthos area (Greece). *Hydrological Processes* 17.(12), pp. 2327–2345. DOI: 10.1002/hyp.1245.
- Stuiver, M. and H. A. Polach (1977). Discussion Reporting of ^{14}C Data. *Radiocarbon* 19.(3), pp. 355–363. DOI: 10.1017/S0033822200003672.
- Sun, X., P. Yang, Y. Xiang, X. Si, and D. Liu (2018). Across-fault distributions of radon concentrations in soil gas for different tectonic environments. *Geosciences Journal* 22.(2), pp. 227–239. DOI: 10.1007/s12303-017-0028-2.

- Tam, V. T., F. De Smedt, O. Batelaan, and A. Dassargues (2004). Study on the relationship between lineaments and borehole specific capacity in a fractured and karstified limestone area in Vietnam. *Hydrogeology Journal* 12.(6), pp. 662–673. DOI: 10.1007/s10040-004-0329-1.
- Theis, C. V. (1935). The relation between the lowering of the piezometric surface and the rate and duration of discharge of a well using ground-water storage. *Eos, Transactions American Geophysical Union* 16.(2), pp. 519–524. DOI: 10.1029/TR016i002p00519.
- Toran, L. and K. R. Bradbury (1988). Ground-Water Flow Model of Drawdown and Recovery Near an Underground Mine. *Groundwater* 26.(6), pp. 724–733. DOI: 10.1111/j.1745-6584.1988.tb00423.x.
- Toutain, J.-P. and J.-C. Baubron (1999). Gas geochemistry and seismotectonics: a review. *Tectonophysics* 304.(1-2), pp. 1–27. DOI: 10.1016/S0040-1951(98)00295-9.
- Umeda, K. and A. Ninomiya (2009). Helium isotopes as a tool for detecting concealed active faults. *Geochemistry, Geophysics, Geosystems* 10.(8), pp. 1–10. DOI: 10.1029/2009GC002501.
- Underwood, S. C., J. L. McCallum, P. G. Cook, C. T. Simmons, S. Dogramaci, R. Purtschert, A. J. Siade, and H. Prommer (2018). Physical and Chemical Controls on the Simultaneous Occurrence of Young and Old Groundwater Inferred From Multiple Age Tracers. *Water Resources Research* 54.(11), pp. 9514–9532. DOI: 10.1029/2018WR022800.
- Valdes, D., J. Dupont, B. Laignel, S. Ogier, T. Leboulanger, and B. J. Malhler (2007). A spatial analysis of structural controls on Karst groundwater geochemistry at a regional scale. *Journal of Hydrology* 340.(3-4), pp. 244–255. DOI: 10.1016/j.jhydrol.2007.04.014.
- Viezzoli, A., F. Jørgensen, and C. Sørensen (2013). Flawed Processing of Airborne EM Data Affecting Hydrogeological Interpretation. *Groundwater* 51.(2), pp. 191–202. DOI: 10.1111/j.1745-6584.2012.00958.x.
- Vittecoq, B., P. A. Reninger, S. Violette, G. Martelet, B. Dewandel, and J. C. Audru (2015). Heterogeneity of hydrodynamic properties and groundwater circulation of a coastal andesitic volcanic aquifer controlled by tectonic induced faults and rock fracturing – Martinique island (Lesser Antilles – FWI). *Journal of Hydrology* 529.(3), pp. 1041–1059. DOI: 10.1016/j.jhydrol.2015.09.022.
- Vreeswyk, A. M. E. v., K. A. Leighton, A. L. Payne, and P. Henning (2004). *An inventory and condition survey of the Pilbara region, Western Australia*. Report 92. South Perth: Department of Agriculture, Government of Western Australia.
- Walker, G. R. and P. G. Cook (1991). The importance of considering diffusion when using carbon-14 to estimate groundwater recharge to an unconfined aquifer. *Journal of Hydrology* 128.(1-4), pp. 41–48. DOI: 10.1016/0022-1694(91)90130-A.

- Weissmann, G. S., Y. Zhang, E. M. LaBolle, and G. E. Fogg (2002). Dispersion of groundwater age in an alluvial aquifer system. *Water Resources Research* 38.(10), pp. 16.1–16.13. DOI: 10.1029/2001WR000907.
- White, J. T., M. N. Fienen, and J. E. Doherty (2016). A python framework for environmental model uncertainty analysis. *Environmental Modelling and Software* 85, pp. 217–228. DOI: 10.1016/j.envsoft.2016.08.017.
- Wilkes, S. M., T. P. Clement, and C. J. Otto (2004). Characterisation of the hydrogeology of the Augustus River catchment, Western Australia. *Hydrogeology Journal* 12 (2), pp. 209–223. DOI: 10.1007/s10040-003-0298-9.
- Wu, Y.-X., J. S. Shen, W.-C. Cheng, and T. Hino (2017). Semi-analytical solution to pumping test data with barrier, wellbore storage, and partial penetration effects. *Engineering Geology* 226, pp. 44–51. DOI: 10.1016/j.enggeo.2017.05.011.
- Ye, M., S. P. Neuman, and P. D. Meyer (2004). Maximum likelihood Bayesian averaging of spatial variability models in unsaturated fractured tuff. *Water Resources Research* 40.(5), pp. 1–17. DOI: 10.1029/2003wr002557.
- Ye, M., K. F. Pohlmann, J. B. Chapman, G. M. Pohll, and D. M. Reeves (2010). A Model-Averaging Method for Assessing Groundwater Conceptual Model Uncertainty. *Groundwater* 48.(5), pp. 716–728. DOI: 10.1111/j.1745-6584.2009.00633.x.
- Younger, P. L., S. A. Banwart, and R. S. Hedin (2002). *Mine Water Hydrology, Pollution, Remediation*. Ed. by B. V. Springer-Science+Business Media. Vol. 5. Environmental Pollution. Dordrecht, The Netherlands, p. 453. ISBN: 978-1-4020-0138-3. DOI: 10.1007/978-94-010-0610-1.
- Zell, W. O., T. B. Culver, and W. E. Sanford (2018). Prediction uncertainty and data worth assessment for groundwater transport times in an agricultural catchment. *Journal of Hydrology* 561, pp. 1019–1036. DOI: 10.1016/j.jhydrol.2018.02.006.
- Zinn, B. A. and L. F. Konikow (2007a). Effects of intraborehole flow on groundwater age distribution. *Hydrogeology Journal* 15.(4), pp. 633–643. DOI: 10.1007/s10040-006-0139-8.
- Zinn, B. A. and L. F. Konikow (2007b). Potential effects of regional pumpage on groundwater age distribution. *Water Resources Research* 43.(6), pp. 1–17. DOI: 10.1029/2006WR004865.